



**HAL**  
open science

# Image processing methods for 3D intraoperative ultrasound

Pierre Hellier

► **To cite this version:**

Pierre Hellier. Image processing methods for 3D intraoperative ultrasound. Modeling and Simulation. Université Rennes 1, 2010. tel-00536133

**HAL Id: tel-00536133**

**<https://theses.hal.science/tel-00536133>**

Submitted on 15 Nov 2010

**HAL** is a multi-disciplinary open access archive for the deposit and dissemination of scientific research documents, whether they are published or not. The documents may come from teaching and research institutions in France or abroad, or from public or private research centers.

L'archive ouverte pluridisciplinaire **HAL**, est destinée au dépôt et à la diffusion de documents scientifiques de niveau recherche, publiés ou non, émanant des établissements d'enseignement et de recherche français ou étrangers, des laboratoires publics ou privés.

# HABILITATION À DIRIGER DES RECHERCHES

présentée devant

**L'Université de Rennes 1**  
**Spécialité : informatique**

par

Pierre Hellier

Image processing methods for 3D intraoperative ultrasound

**soutenu le 30 Juin 2010 devant le jury composé de :**

Nicholas Ayache	Directeur de Recherches INRIA	rapporteur
David Hawkes	Prof. University College London	rapporteur
Etienne Mémin	Directeur de Recherches INRIA	
Xavier Morandi	Prof. des Universités - Praticien Hospitalier	
Wiro Niessen	Prof. Univ. Medical Center Rotterdam	
Jean-Philippe Thiran	Prof. Ecole Polytech. Féd. de Lausanne	rapporteur
Jocelyne Troccaz	Directeur de Recherches CNRS (absente)	

Je remercie Nicholas Ayache, Dave Hawkes, Jean-Philippe Thiran, Jocelyne Troccaz, Wiro Niessen, Etienne Mémin, Xavier Morandi de m'avoir fait l'honneur d'évaluer ce travail malgré un emploi du temps toujours chargé en cette période. Leurs travaux ont eu une influence majeure sur le contenu présenté dans cette habilitation.

Le travail présenté ici a été réalisé entre 2004 et 2009, au sein de l'équipe projet Visages (INRIA-INSERM), et en partenariat avec le service de neurochirurgie du CHU Pontchaillou à Rennes. De nombreuses personnes, avec qui j'ai eu un grand plaisir à travailler, y ont contribué, parmi lesquelles Alexandre Abadie, Guillermo Andrade-Barroso, Gilles Brassier, Romain Carpentier, Sean Chen, Louis Collins, Pierrick Coupé, Nicolas Courty, Anne Cuzol, Jean-Yves Gauvrit, Vincent Gratsac, Claire Haegelen, Pierre-Louis Henaux, Charles Kervrann, Etienne Mémin, Xavier Morandi, Pierre Meyer, Arnaud Ogier, Fernanda Palhano, Sylvain Prima et François Rousseau.

Je tiens à remercier plus particulièrement Xavier Morandi, neurochirurgien, pour son apport scientifique, technique et humain à ce projet. Les résultats présentés ici sont indissociables de son enthousiasme quotidien. J'espère avoir la chance que nous continuions à travailler ensemble à l'avenir.. Dans ce contexte si particulier de la neurochirurgie, je tiens aussi à remercier tous les personnels de salle d'opération (Ide, Ibod) qui nous ont accueillis avec une constante bienveillance en salle d'opération.

Une personne tient une place particulière dans ce travail : Pierrick Coupé, qui a effectué sa thèse entre 2004 et 2007, et qui a grandement contribué à ce projet de recherche par ses qualités scientifiques et son enthousiasme. Ce fut un énorme plaisir de travailler avec Pierrick.

J'ai une pensée particulière pour Louis Collins et tous les collègues et amis du MNI chez qui j'ai passé une année en 2006. Une année extraordinaire.

Pour Matéo et Mila

1	Résumé français	1
1.1	Neurochirurgie guidée par l'image	1
1.2	Contributions	2
1.2.1	Plate-forme logicielle pour le planning préopératoire et la navigation intraopératoire	2
1.2.2	Méthodes d'analyse d'images	2
2	Introduction	5
2.1	Image guided neurosurgery	5
2.2	Summary of contributions	6
2.2.1	Software platform for preoperative planning and intra-operative navigation	6
2.2.2	Image analysis methods	8
3	Calibration	11
3.1	Introduction	11
3.1.1	3D ultrasound data	11
3.1.2	Spatial and temporal calibration	11
3.1.3	Related work	13
3.2	Proposed method	13
3.2.1	Phantom	13
3.2.2	Feature extraction	14
3.2.3	Spatial and temporal calibration	15
3.3	Quantitative evaluation	18
3.3.1	Introduction	18
3.3.2	Evaluation criteria	18
3.3.3	Results	20
3.4	Discussion	20
4	Reconstruction	23
4.1	Introduction	23
4.1.1	Motivation	23
4.1.2	Related work	23
4.2	Reconstruction method	24
4.2.1	Distance Weighted Interpolation	24
4.2.2	Probe Trajectory Interpolation	24
4.3	Results	26
4.3.1	Simulated intra-operative sequences	26
4.3.2	Ultrasound intra-operative sequences	28

4.4	Discussion . . . . .	28
5	Artifacts detection and reduction	31
5.1	Introduction . . . . .	31
5.2	Denoising . . . . .	32
5.2.1	Introduction . . . . .	32
5.2.2	NL-means . . . . .	33
5.2.3	Adaptation to ultrasound noise model . . . . .	35
5.2.4	Results . . . . .	35
5.2.5	Quantitative analysis on registration accuracy . . . . .	36
5.3	Detection of ultrasound acoustic shadows . . . . .	39
5.3.1	Introduction . . . . .	39
5.3.2	A geometric and photometric method . . . . .	40
5.3.3	Results . . . . .	44
5.4	Discussion . . . . .	46
6	Registration	47
6.1	Introduction . . . . .	47
6.2	Method . . . . .	48
6.2.1	Matching hyperechogenic structures . . . . .	48
6.2.2	Construction of the probability maps . . . . .	48
6.2.3	Non-rigid parametrization . . . . .	49
6.2.4	Optimization . . . . .	51
6.3	First results . . . . .	51
6.4	Discussion . . . . .	52
7	Further work	57
7.1	Capturing intraoperative deformations . . . . .	57
7.2	Intraoperative tissue characterization . . . . .	58
7.3	Clinical context: learning and validation . . . . .	59
	Bibliography	61
8	Publications	75

Ce document constitue une synthèse de travaux de recherche en vue de l'obtention du diplôme d'habilitation à diriger les recherches. A la suite de cette introduction rédigée en français, le reste de ce document sera en anglais. Je suis actuellement chargé de recherches INRIA au centre de Rennes Bretagne Atlantique. J'ai rejoint en Septembre 2001 l'équipe Vista dirigée par Patrick Bouthemy, puis l'équipe Visages dirigée par Christian Barillot en Janvier 2004. Depuis Janvier 2010, je travaille dans l'équipe-projet Serpico dirigée par Charles Kervrann dont l'objet est l'imagerie et la modélisation de la dynamique intracellulaire.

Parmi mes activités passées, ce document va se concentrer uniquement sur les activités portant sur la neurochirurgie guidée par l'image. En particulier, les travaux effectués sur le recalage non-rigide ne seront pas présentés ici. Concernant le recalage, ces travaux ont commencé pendant ma thèse avec le développement d'une méthode de recalage 3D basé sur le flot optique [72], l'incorporation de contraintes locales dans ce processus de recalage [74] et la validation de méthodes de recalage inter-sujets [71]. J'ai poursuivi ces travaux après mon recrutement avec Anne Cuzol et Etienne Mémin sur la modélisation fluide du recalage [44], avec Nicolas Courty sur l'accélération temps-réel de méthode de recalage [42], et sur l'évaluation des méthodes de recalage dans deux contextes : celui de l'implantation d'électrodes profondes [29] et le recalage inter-sujets [92].

## 1.1 NEUROCHIRURGIE GUIDÉE PAR L'IMAGE

L'utilisation de systèmes dits de neuronavigation est maintenant courante dans les services de neurochirurgie. Les bénéfices, attendus ou reportés dans la littérature, sont une réduction de la mortalité et de la morbidité, une amélioration de la précision, une réduction de la durée d'intervention, des coûts d'hospitalisation. Tous ces bénéfices ne sont pas à l'heure actuelle démontrés à ma connaissance, mais cette question dépasse largement le cadre de ce document. Ces systèmes de neuronavigation permettent l'utilisation du planning chirurgical pendant l'intervention, dans la mesure où le patient est mis en correspondance géométrique avec les images préopératoires à partir desquelles est préparée l'intervention.

Ces informations multimodales sont maintenant couramment utilisées, comprenant des informations anatomiques, vasculaires, fonctionnelles. La fusion de ces informations permet de préparer le geste chirurgical : où est la cible, quelle est la voie d'abord, quelles zones éviter. Ces informations peuvent maintenant être utilisées en salle d'opération et visualisées dans les oculaires du microscope chirurgical grâce au système de neuronavigation. Malheureusement,

cela suppose qu'il existe une transformation rigide entre le patient et les images préopératoires. Alors que cela peut être considéré comme exact avant l'intervention, cette hypothèse tombe rapidement sous l'effet de la déformation des tissus mous. Ces déformations, qui doivent être considérées comme un phénomène spatio-temporel, interviennent sous l'effet de plusieurs facteurs, dont la gravité, la perte de liquide céphalo-rachidien, l'administration de produits anesthésiants ou diurétiques, etc.

Ces déformations sont très difficiles à modéliser et prédire. De plus, il s'agit d'un phénomène spatio-temporel, dont l'amplitude peut varier considérablement en fonction de plusieurs facteurs. Pour corriger ces déformations, l'imagerie intra-opératoire apparaît comme la seule piste possible.

### 1.2 CONTRIBUTIONS

Entre 2004 et 2009, j'ai donc travaillé sur une méthode de correction de ces déformations basée sur l'acquisition et l'analyse d'images échographiques intraopératoires. Ce travail a porté sur deux aspects, logiciel d'une part pour la construction d'une plate-forme logicielle pré-opératoire et intra-opératoire; méthodologique d'autre part sur l'analyse d'images.

#### 1.2.1 Plate-forme logicielle pour le planning préopératoire et la navigation intraopératoire

La préparation des données préopératoires (planning), ainsi que l'acquisition et l'exploitation des données intraopératoires ont nécessité le développement d'une plate-forme logicielle financée sur une ODL INRIA.

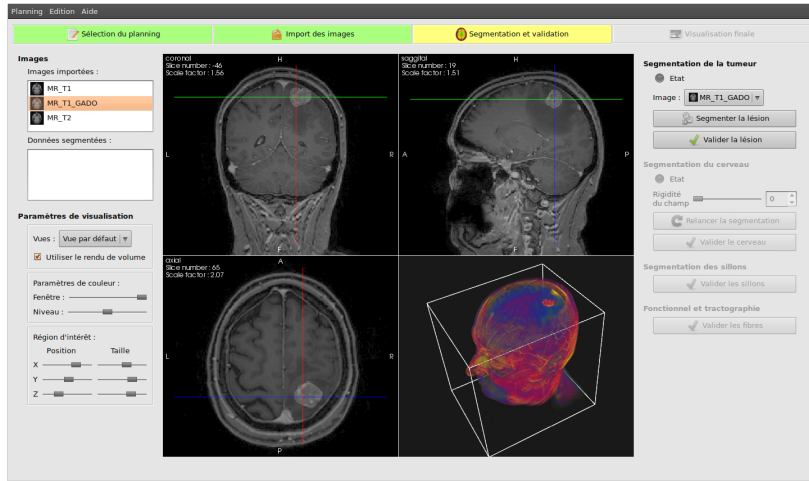
La plate-forme logicielle préopératoire a pour but l'import des données, la segmentation de la peau, du cerveau, de la lésion (la segmentation est manuelle car la segmentation automatique des lésions sur des données cliniques est très difficile [43]), des sillons au voisinage de la lésion, et de la fusion avec des informations fonctionnelles et structurelles. Une première version de cette plate-forme a été déployée fin 2009 dans le service de neurochirurgie de l'hôpital Pontchaillou à Rennes afin d'être utilisée par les médecins sans aide extérieure. La figure 1.1 présente quelques vues de cette application.

Après cette étape de planning, il était nécessaire d'acquérir et d'analyser en salle d'opération des données échographiques. Ce projet a bénéficié du soutien de Rennes Métropole (100 keuros) à travers le financement d'un appareil d'échographie et du module sononav permettant de coupler l'échographe avec la station de neuronavigation. Une plate-forme logicielle intraopératoire, dont des vues sont présentées sur la figure 1.2, permet l'acquisition et le traitement des données intra-opératoires.

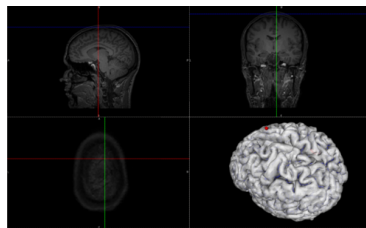
#### 1.2.2 Méthodes d'analyse d'images

L'acquisition et le traitement des données échographique a nécessité le développement d'une chaîne de traitement d'images, partant des données brutes non reconstruites, et s'achevant par une étape de recalage permettant le calcul d'une transformation géométrique compensant les déformations des tissus mous. Ces différentes étapes sont l'objet central de ce document :

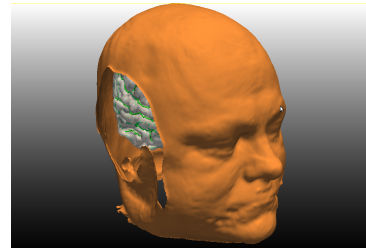
- La calibration est indispensable pour connaître la position des pixels de l'image échographique dans le repère de référence utilisé par le système



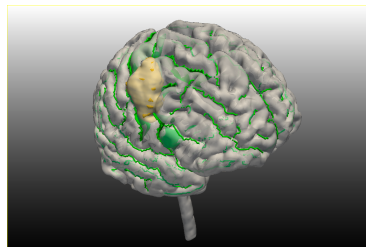
Interface de l'application



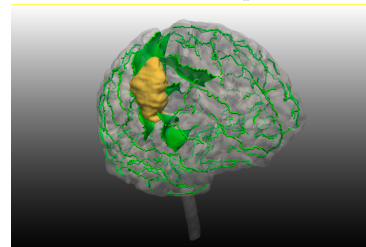
vue 3D view



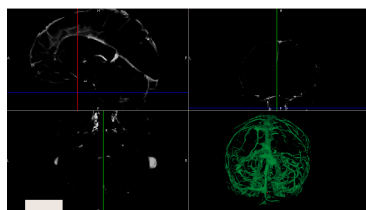
surface de la peau



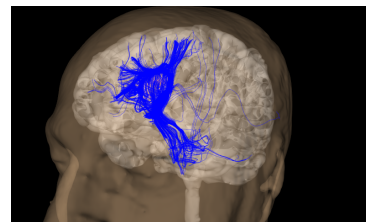
Surface corticale et segmentation de la lésion



Sillons extraits



Vaisseaux extraits



Fibres DTI

Figure 1.1: Visualisation du logiciel de planning. Les vues représentent les étapes de planning, incluant l'import des données, la visualisation 3D, la segmentation de la peau, du cerveau, des sillons et vaisseaux, et la fusion avec le DTI.

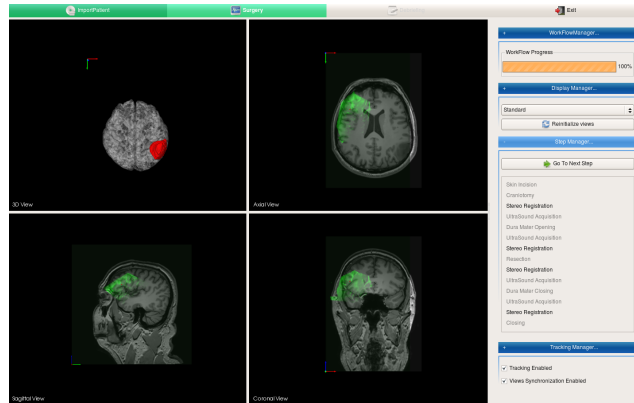


Figure 1.2: Vues de l'application intraopératoire, où la vue échographique est superposée à l'image IRM préopératoire.

de neuronavigation [150]. La calibration temporelle correspond à l'alignement temporel entre le signal de position et le signal vidéo [151]. Ces deux étapes de calibration sont nécessaires afin d'obtenir des données quantitatives fiables [149]. Sur ces aspects, nous avons proposé une méthode extrayant de manière robuste des caractéristiques sur les images échographiques.

- La reconstruction consiste à calculer un volume régulier  $3D$  à partir de la séquence d'images échographiques et de leurs positions. Nous avons proposé une méthode incorporant explicitement l'information de trajectoire de la sonde dans cette étape de reconstruction [39].
- La réduction d'artefacts vise à réduire l'influence du bruit des images échographiques dans les processus de traitement d'images. En effet, les images échographiques sont corrompues par des variations de signal importantes, qui peuvent être de différente nature : forte atténuation du signal en profondeur, ombres acoustiques, et bruit important. Pour se faire, nous nous sommes appuyés sur une modélisation simple mais efficace de ce bruit afin de débruiter les images par une approche de type NL means [36] d'une part, et détecter les ombres acoustiques d'autre part [73].
- Enfin, les étapes de recalage cherchent à aligner de manière rigide [38] ou non-rigide [40] les images échographiques intraopératoires et l'IRM préopératoire. Nous avons proposé une méthode mettant explicitement en correspondance les structures hyperéchogènes.

Ce document va donc présenter de manière synthétique les étapes de traitement d'images, des chapitres 3 à 6, le lecteur pouvant trouver les détails techniques dans les publications associées: références [149–151] pour le chapitre 3, référence [39] pour le chapitre 4, références [36, 41, 73] pour le chapitre 5, références [37, 40] pour le chapitre 6.

This document constitutes a synthesis in preparation for my habilitation degree in computer science. I am now researcher at INRIA Rennes since September 2001. From September 2001 to January 2004, I was a researcher in the *Vista* project headed by Patrick Bouthemy, and moved to the *Visages* project headed by Christian Barillot. In January 2010, I moved to the *Serpico* team headed by Charles Kervrann that focuses on "imaging and modeling intracellular dynamics of molecular architectures". This document presents part of my work among the Visages team. Actually, this habilitation thesis will focus on image processing aspects of intraoperative ultrasound in neurosurgery.

My work on non-rigid registration will not be described here. The work on non-rigid registration began during my PhD thesis, where the three main contributions were the design of a 3D non-rigid registration method based on optical flow [72], the incorporation of local constraints [74] and the retrospective evaluation of inter-subject registration [71]. I continued working on image registration, with Anne Cuzol and Etienne Mémin using fluid motion description [44], with Nicolas Courty on GPU accelerated registration [42] and on evaluation of non-rigid registration techniques: with Mallar Chakravarty and co-authors [29] for deep-brain stimulation planning; with Arno Klein and co-authors [92] concerning inter-subject brain registration.

## 2.1 IMAGE GUIDED NEUROSURGERY

In the last decade, it has become increasingly common to use image-guided navigating systems to assist surgical procedures [51]. The reported benefits are improved accuracy, reduced intervention time, improved quality of life, reduced morbidity (and perhaps mortality), reduced intensive care and reduced hospital costs. Image-guided systems can help the surgeon plan the operation and provide accurate information about the anatomy during the intervention. Image-guided systems are also useful for minimally invasive surgery, since the intraoperative images can be used interactively as a guide.

Current surgical procedures rely on complex preoperative planning, including various multimodal examinations: anatomical, vascular, functional explorations for brain surgery. Once all information has been merged, it can be used for navigation in the operating theatre (OR) using image-guided surgery systems. Image-guided surgery involves the rigid registration of the patient's body with the preoperative data. With an optical tracking system, and Light Emitting Diodes (LED), it is possible to track the patient's body, the microscope and the surgical instruments in real time. The preoperative data can then be merged with the surgical field of view displayed in the microscope. This fusion is called "augmented reality".

Unfortunately, the assumption of a rigid registration between the patient's body and the preoperative images only holds at the beginning of the procedure. This is because soft tissues tend to deform during the intervention. This is a common problem in many image-guided interventions, the particular case of neurosurgical procedures can be considered as a representative case. When dealing with neurosurgery, this phenomenon is called "brain shift".

Although the impact and the magnitude of soft tissue motion have been studied over the last few years, this phenomenon is still poorly understood. Soft tissue deformation can be explained by physiological (steroids, diuretic medication, mechanical ventilation) and mechanical factors (CSF leakage, patient positioning, tumor nature and location, craniotomy size, gravity [117], etc).

The magnitude of brain shift shows striking differences at each stage of surgery. Brain shift must be considered as a spatio-temporal phenomenon, and should be estimated continuously, or at least at key moments, to update the preoperative planning. To do so, one possibility is to deform the anatomical and functional images according to the estimated deformation.

### 2.2 SUMMARY OF CONTRIBUTIONS

Between 2004 and 2009, I have worked on designing a soft tissue deformation correction workflow based on intraoperative tracked ultrasound. To do so, two aspects of the project needed to be considered: a technical side needed to acquire and process data and perform clinical evaluation, and a methodological side to design novel image analysis methods.

#### 2.2.1 Software platform for preoperative planning and intraoperative navigation

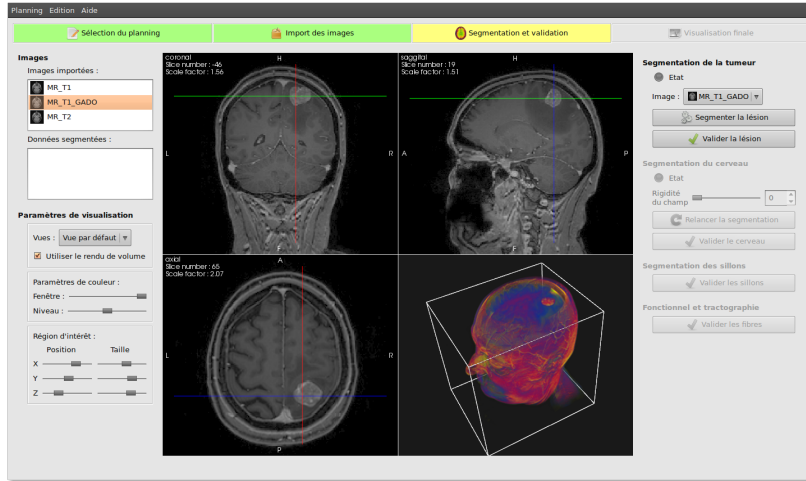
From a technical side, it was necessary to acquire ultrasound image intraoperatively. Rennes city council granted 100keuros for this project, what was used to purchase a sonosite ultrasound equipment the sononav module for the Medtronic neuronavigation system. The project has also been supported by an INRIA "ODL" grant.

The preoperative software platform is designed to build a 3D scene from raw MR data, containing only relevant information needed to plan surgery, including skin and brain surface, manual lesion segmentation since fully automatic lesion segmentation is difficult in clinical routine [43], sulci and vessel segmentation in the vicinity of the tumor, extraction and mapping of fMRI and DTI data. Figures 2.1 presents some visualization of the obtained 3D scenes.

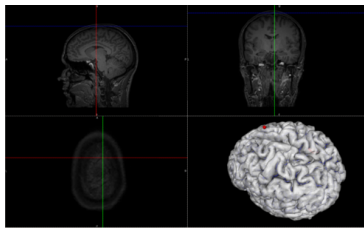
The pre-operative software platform has been deployed at the neurosurgery department in Rennes University Hospital to be used daily and autonomously by neurosurgeons.

Once pre-operative information have been acquired, it can be used in the operating room (OR) during surgery. To enable the visualization of this information (on a workstation and in the ocular of the microscope), we have developed a intraoperative software platform. Thanks to the stealthlink library provided by Medtronic - the vendor of the neuronavigation system used in neurosurgery - it is possible to acquire the position of the tools tracked by the neuronavigation system. We were thus able to visualize the pre-operative data,

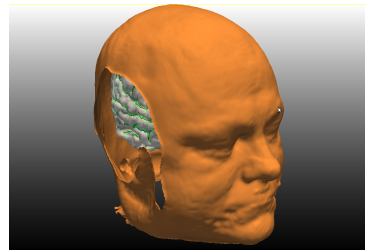
## 2.2. Summary of contributions



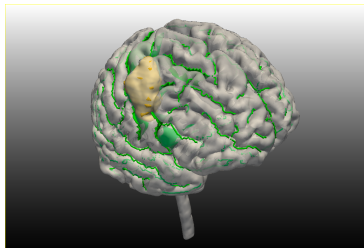
Application interface



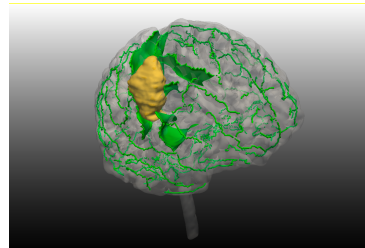
3D view



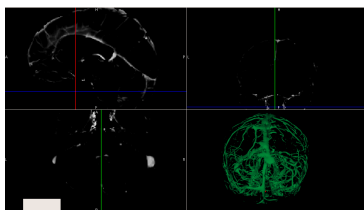
skin surface



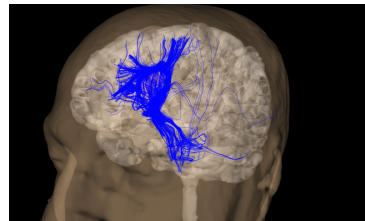
Brain surface and lesion segmentation



Extracted sulci



Extracted vessels



DTI fibers

Figure 2.1: Visualization of the pre-operative software. Figures present the successive steps of the planning, including data import and 3D visualization, segmentation of skin surface, brain, sulci and vessels extraction, DTI fusion.

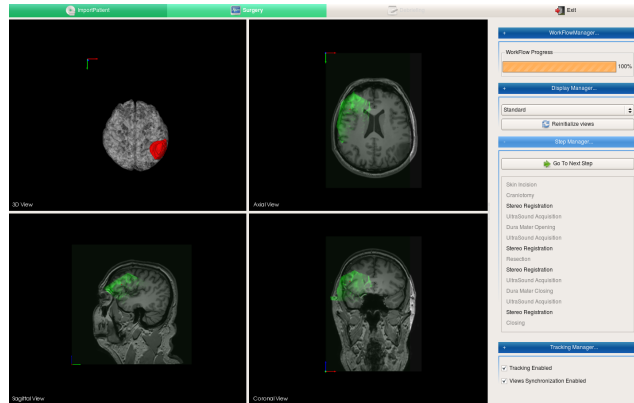


Figure 2.2: Visualization of the intraoperative application. The acquired ultrasound image is overlaid in green on top of the pre-operative MR image.

and acquire intraoperative tracked ultrasound images. Figure 2.2 presents a visualization of the intraoperative application.

### 2.2.2 Image analysis methods

From an image analysis point of view, I worked on image processing methods composing a workflow that takes raw unreconstructed ultrasound images as an input, and provides geometrical transformations intended to accommodate soft-tissue deformations. To do so, several steps are needed to process the data:

- Calibration is needed to determine accurately the coordinates of the ultrasound pixels in the coordinate system of the reference frame [150]. In addition, temporal calibration is mandatory to align temporally the image signal (acquired through a video card) to the position signal provided by the 3D localization system [151]. For these two tasks, we have proposed a method that extracts accurately and robustly relevant features that will be used to calibrate the system spatially [150] and temporally [151]. We have also assessed that accurate calibration is critical for quantitative image analysis [149].
- Reconstruction means computing a 3D regular lattice volume out of the unreconstructed set of B-scans. To do so, we have proposed a technique that incorporates the probe's motion into the reconstruction process [39].
- Artifact reduction is helpful for quantitative image analysis. Ultrasound images are corrupted by an important noise, often called speckle, and exhibit imaging artifact like signal attenuation and acoustic shadows. To remove or detect these artifact, we have used a simple yet efficient modeling of the ultrasound noise to denoise ultrasound images using a adapted NL-means method [36] and to detect acoustic shadows [73].
- Registration finally computes the geometrical transformation that aligns rigidly [37] or non-rigidly [40] the intraoperative ultrasound to the pre-operative MR. To do so, we have proposed a method based on the extraction and matching of hyperechogenic structures.

The image analysis methods that were developed within this project will be the core of this document. Methods will be presented in a synthetic manner, and the interested reader is referred to corresponding publications for technical details: publications [149–151] for chapter 3, publication [39] for chapter 4, publications [36, 41, 73] for chapter 5, publications [37, 40] for chapter 6.



### 3.1 INTRODUCTION

#### 3.1.1 3D ultrasound data

In our application, 3D ultrasound data is mandatory to capture the 3D nature of the deformation. 3D ultrasound data can now be acquired by different means: sensorless ultrasound, 2D probe associated with constrained or known motion (3D mechanical probes, tracked ultrasound) or direct 3D probes.

- Sensorless technique uses image speckle to determine out-of-plane motion between two consecutive B-scans.
- Mechanical probes correspond to an internal mechanical sweep (usually a fan motion) implemented within the ultrasound probe.
- Tracked ultrasound correspond to a standard 2D probe that is moved freely, and where the probe's motion is either observed (by a optical or magnetic sensor mounted on the probe) or known, for instance if the probe is mounted on a robotic arm.
- Recently, 3D probes have appeared with the development of 2D phase arrays. Actually, these probes are now capable of 4D image acquisition. The field of view of these probes is however limited at the moment compared to standard 2D probes.

In the context of image-guided surgery, not all these probes are relevant. In particular, mechanical probes are too cumbersome for neurosurgery where the probe footprint should be as small as possible. Sensorless techniques are inappropriate since the neuronavigation system is equipped with a 3D localization system and it would make no sense not to use it. 3D probes is an appealing technique, however, the field of view is too limited at the moment to be used, but it is foreseen that it should become the "ideal" acquisition technique when this limitation disappears. There has been some promising work to create "mosaics" with various acquisition, so as to increase the field of view [172].

#### 3.1.2 Spatial and temporal calibration

##### 3.1.2.1 Spatial calibration

When using ultrasound for image-guided procedures, the probe needs to be tracked using the position system of the neuronavigation system. This enables positioning the ultrasound image with respect to preoperative images. Calibration is then needed to correctly position the ultrasound image in the coordinate

system of the camera, and embraces spatial and temporal calibration. This is illustrated in figure 3.1.

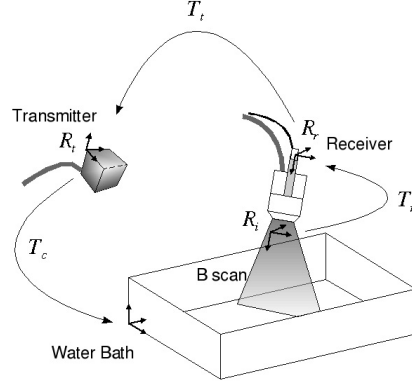


Figure 3.1: *Coordinate systems :  $R_i$  (image),  $R_r$  (receiver),  $R_t$  (transmitter in case of magnetic positioning, camera for neuronavigation systems),  $R_c$  (reconstruction volume, surgical field of view).*

The spatial calibration problem can be formulated in the following way ([140]):

$$\mathbf{x}_c = T_c T_t T_r \mathbf{x}_r, \text{ with } \mathbf{x}_r = \begin{pmatrix} s_x u \\ s_y v \\ 0 \\ 1 \end{pmatrix} \quad (3.1)$$

where  $T_r$  denotes the rigid transformation from B-scan to probe's tool coordinates,  $T_t$  is the rigid transformation from probe's tool to camera coordinates,  $T_c$  stands for the rigid transformation from camera to reference arc coordinates,  $u$  and  $v$  are the image pixel coordinates,  $s_x$  and  $s_y$  denote scaling factors or pixel spatial resolution (see Figure 3.1).

Performing the spatial calibration amounts to estimating the matrix  $T_r$  (3 translations and 3 rotations) and the scaling coefficients  $s_x$  and  $s_y$ . The calibration is generally carried out in the following way: after scanning a phantom whose 3D geometrical properties are known, the calibration is based on this geometry being recovered in the sequence of ultrasound images.

$T_r$  is a rigid-body transformation :

$$T_r(t_x, t_y, t_z, \alpha, \beta, \gamma) = \begin{bmatrix} R(\alpha, \beta, \gamma) & \mathbf{t}(t_x, t_y, t_z) \\ 0 & 1 \end{bmatrix} \quad (3.2)$$

where  $\mathbf{t}(t_x, t_y, t_z)$  is a translation vector,  $(\alpha, \beta, \gamma)$  the rotation angles around axis  $(z, y, x)$  and  $R(\alpha, \beta, \gamma)$  is a rotation matrix.

### 3.1.2.2 Temporal calibration

Temporal calibration consists of estimating the latency between the position sensor timestamps and ultrasound image timestamps. Temporal calibration depends on the experimental setup, including video grabber and PC used,

echographic machine and video transfer format, position sensor and transfer rate, image quality of the phantom used for calibration. Therefore, temporal calibration is specific to each experimental setup.

### 3.1.3 Related work

Spatial calibration has been investigated by different groups and exhaustive survey paper exists on the subject [80, 116]. Methods can be grossly sorted according to the type of phantom used, ranging from single point phantom [13, 46, 97, 169], single point tracked by a stylus [6, 68, 136, 171], multiple points from a stylus [89], three-wire phantom [28], plane phantom [5, 140, 150, 170], two-plane phantom [20], 2D shaped board phantom [16, 107, 156, 175], Z-phantom [21, 31, 35] or "image registration" approach [19].

The different phantoms have drawbacks and advantages, regarding the context of use. In particular, some phantoms (especially point phantoms) require a manual segmentation of the point that is tedious and time-consuming. These phantoms are not suited when calibration needs to be repeated often.

Temporal calibration has previously been achieved by estimating the latency using visual criteria for augmented reality [82]. This system was composed of an ultrasound probe held with a mechanical arm and a virtual reality helmet tracked by a magnetic sensor. For images acquired at  $10Hz$ , the measured latency was  $220ms$ . Some authors have used a water bath phantom to match changes in the position and line signals [81, 141, 168]. Other groups [89, 122, 123] proposed a temporal calibration method using a point based phantom. Latency estimation is performed with a least-square minimization of the distance between the phantom point and the estimated position of this point. Gooding *et al.* [62] have proposed an image alignment method that relaxes the hypothesis of a constant latency between two scans.

## 3.2 PROPOSED METHOD

### 3.2.1 Phantom

In our work, we have decided to rely on a plane-phantom since the latter is easy to design. Two aspects cannot be neglected for a correct calibration: first, a 9% alcohol solution needs to be used in the water bath to obtain a speed of sound comparable with the one expected by the ultrasound machine. Second, a complete sequence of probe motion needs to be achieved to solve the calibration, including a wide range of angles and positions as described in [140]. The major difficulty of such phantom is the robust and accurate detection of the plane. As a matter of fact, when the angle between the beam and the water bath decreases below 70 degrees, the combined effect of beam thickness and wave reflection leads to a weak signal in the ultrasound image as can be seen in figure 3.2. We have therefore focused on proposing a reliable feature extraction method.

The plane phantom is also suitable for temporal calibration, since some probe motion lead to a change of the line signal that can be easily identified. However, not all probe motion correspond to image changes, as translations over the water bath at a given angle and altitude will not change the appearance of the line. Therefore, using adequate probe motion, the line feature can be matched with the position signal in order to achieve temporal calibration.

### 3.2.2 Feature extraction

In this section, the feature extraction process from ultrasound images is described. These features will be used for the spatial and temporal calibration processes. For the spatial calibration, a point set corresponding to the water bath is extracted. For the temporal calibration, a line regression method is used. The feature extraction is performed in the following steps:

- The point extraction is performed retaining the highest gradient and highest luminance points. The threshold is fixed (in percentage) compared to the maximum in intensity and gradient in the first image. These two features are needed because, as it can be seen in figure 3.2, either intensity or gradient information alone would not be sufficient for a reliable extraction. Since the points of interest extraction is done by thresholding, this step is sensitive to outliers. To obtain a robust algorithm, the consistency of the extraction is checked successively using 2D information (Hough transform) and 3D information (spatio-temporal continuity of the point set).
- To reject outliers in each image, the Hough transform [79] is used to isolate features of a particular shape within an image. A convenient equation for describing a set of lines uses parametric or normal notion :  $x \cos \theta + y \sin \theta = r$ , where  $r$  is the length of a normal from the origin to this line and  $\theta$  is the orientation of  $r$  with respect to the X-axis in the B-scan. For any point  $(x, y)$  on this line,  $r$  and  $\theta$  are constant. When viewed in Hough parameter space  $(r, \theta)$ , points which are collinear in the cartesian image space become readily apparent as they yield curves which intersect at a common  $(r, \theta)$  point. The transform is implemented by quantizing the Hough parameter space into finite intervals or accumulator cells. Each  $(x_i, y_i)$  is transformed into a discretized  $(r, \theta)$  curve and the accumulator cells which lie along this curve are incremented. Peaks in the accumulator array represent strong evidence that a corresponding straight line exists in the image. The Hough transform is used to extract in each B-scan a line whose equation is:  $ax + by + c = 0$ . Given the equation of the line and the point set, we have to reject possible outliers. Using the Euclidian distance as selection criterion, only the closest points to the line are retained using a fixed threshold.
- 3D consistency: spatio-temporal continuity of the point set. To ensure coherence in all the ultrasound sequence, we reject image where the line extraction is not correct. Continuity of probe motion should lead to a smooth variation of parameters  $a, b$  and  $c$ . Figure 3.3 plots the evolution of  $a, b$  and  $c$  for the US sequence. We think that a discriminant parameter is the intersection of the line with the axis  $y = 0$ , that is to say parameter  $-\frac{c}{a}$ . Let us note  $\Delta$  the successive differences of the parameter  $-\frac{c}{a}$  :  $\Delta_k \triangleq -\frac{c_k}{a_k} + \frac{c_{k-1}}{a_{k-1}}$ . Figure 3.3 (bottom right) shows the evolution of  $\Delta$  for the same sequence. Peaks of this plot correspond to incorrect line detection (see Figure 3.4).

There are only two probe motions that produce two important plane motions in the ultrasound images : translation in  $y$  axis and rotation

around the  $z$  axis, in the image coordinate system. Considering an important translation motion of  $5\text{cm/s}$  in  $y$  axis, with an acquisition rate of 5 images per second and typical scale factors equal to  $0.01\text{ mm/pixel}$ ,  $\Delta$  which corresponds to the plane motion in the B-scan is equal to 100 *pixels*. For the rotation motion around the  $z$  axis, for an angle equal to 10 degrees between two successive B-scans and an B-scan width equal to 500 *pixels*, the value of  $\Delta$  is under 100. This justifies our choice to set the rejection threshold to 100.

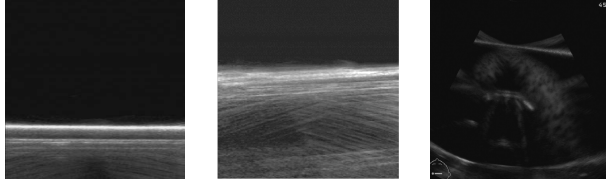


Figure 3.2: *Representative images of ultrasound sequences of the water bath.*

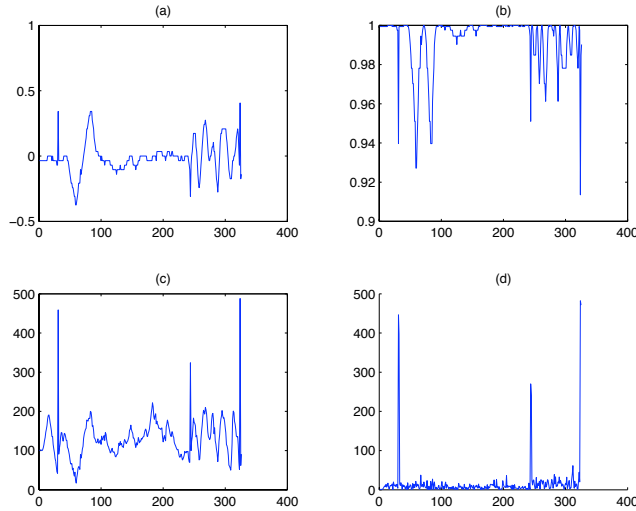


Figure 3.3: *Evolution of the line parameters (a, b and c) and  $\Delta$  for a classical calibration sequence.*

### 3.2.3 Spatial and temporal calibration

#### 3.2.3.1 Spatial calibration

Calibration parameters and plane parameters are estimated by minimizing the Euclidian distance between the plane and the points of interest.

$$\hat{T}_r = \arg \min_T \left\{ \frac{1}{2} \sum_{i=1}^N d_{3D}(\pi, M_i)^2 \right\} \quad (3.3)$$

where  $N$  is the cardinal of the point set,  $d_{3D}(\pi, M)$  is the 3D Euclidian distance between the plane  $\pi$  and the point of interest  $M_i$  in 3D space. The cost function

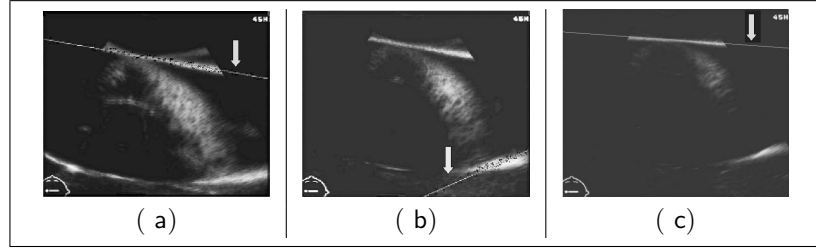


Figure 3.4: *Line detection with the Hough transform for three successive images. In (a) and (c), good detection; in (b), bad detection, the line is rejected.*

can be readily derivated with respect to all parameters and is optimized using Levenberg-Marquardt algorithm [119].

To shorten the computation time, we propose a hierarchical multiresolution algorithm [26]. The complexity of the algorithm only depends on the number of points of interest used to minimize  $f$ . Thus, we can divide the optimization procedure into different stages. For instance, with a fixed number  $N$  of interest points, the first optimization part is performed with a third of  $N$  points. This result is used as an initialization for an optimization using two thirds of  $N$  points. Then the second part with two thirds of  $N$  points, and finally, with all extracted points. This hierarchical decomposition permits us to split the algorithm complexity and in this way, to shorten computation time.

Optimization might be sensitive to outliers due to speckle noise in the US image, even if the 2D and 3D consistency of the extracted point set is ensured. Nevertheless, the set of interest points has been retained by thresholding what is sensitive to outliers. Therefore, we use a Least Trimmed Squares estimator (LTS) ([152]) during the optimization stage. The LTS estimator  $\mathcal{T}$  minimizes a criterion  $\mathcal{C}$  with  $r_1^2 \leq r_2^2 \leq \dots \leq r_N^2$  the ordonated remainders, and  $h$  the number of points used for the estimation :  $\hat{T} = \arg \min_T \sum_{i=1}^h r_i^2$ , with  $\frac{N}{2} \leq h \leq N$ . The breaking point of LTS estimator is equal to 0.5 and  $\mathcal{E}$  is close to 1. For each point, the computed remainder is equal to the distance between the plane and the point.

### 3.2.3.2 Temporal calibration

For the temporal calibration, the estimated lines are manipulated with their equation  $x \cos \theta + y \sin \theta - \rho = 0$ , where  $\rho$  is the length of a normal from the origin to this line and  $\theta$  is the orientation of  $\rho$  with respect to the X-axis in the B-scan. Then, the couple of parameters  $(\frac{\cos \theta}{\sin \theta}, \frac{-\rho}{\sin \theta})$  is used to detect ruptures in the line signal. First, B-spline approximation of the evolution of line parameters is performed. Let  $\mathcal{T} = \{\tau_i, i = \dots, n\}$  denotes the knot set. A  $m$  order B-spline is defined as [30]:

$$B_i(t) = (\tau_{i+m+2} - \tau_i) \sum_{j=0}^{m+2} \left( \frac{(\tau_{i+j}-t)_+^{m+1}}{\prod_{l=0: l \neq j}^{m+2} (\tau_{i+j} - \tau_{i+l})} \right), \text{ with}$$

$$(\tau_{i+j} - t)_+^{m+1} = \begin{cases} (\tau_{i+j} - t)^{m+1} & \text{if } t \leq \tau \\ 0 & \text{if } t > \tau. \end{cases}$$

The approximation model is the following:  $Y_i = g(t_i) + W_i$ , with  $g(t_i) = \sum_{j=0}^{q+1} \beta_j B_j(t_i)$  where  $Y_i$  is the raw signal,  $g$  is the regression spline,  $W_i$  are

independent random variables and  $B_j$  are the B-splines. In our case, we used cubic B-splines ( $m = 3$ ) with equidistant knots. Then, in order to reject line outliers, a statistical test is performed on the differences between these approximations and line parameter evolutions.

The latency is estimated by matching the position sensor signals with the line parameters. Using a plane phantom, only certain motion lead to changes in the US image. However, a change of one extracted line parameter always corresponds to a variation of probe motions. Thus, changes in both signals are detected and matched. Line parameter curve  $\frac{-\rho}{\sin\theta}$  is less noisy and variations are larger than for the signal  $\frac{\cos\theta}{\sin\theta}$  related to the line slope. Thus the latency estimation is carried out by matching position sensor signals with the evolution curve of  $sr = \frac{-\rho}{\sin\theta}$  which we will call "reference signal".

Let  $sr$  denotes the reference signal and  $sp_i$  the position sensor signals,  $i \in \{1, \dots, 6\}$  (3 translations and 3 rotations). Let  $\mathcal{G}$  be the point set for which gradient of  $sr$  is zero:  $\mathcal{G} = \{x, \frac{dsr}{dt}(x) = 0\}$ . Latency  $\mathcal{L}$  is estimated so as to minimize the sum of gradient for the points in  $\mathcal{G}$ . We thus minimize:

$$\mathcal{L} = \arg \min_u \sum_{x \in \mathcal{G}} \sum_{i=1}^6 \left( \frac{dsp_i}{dt}(x+u) \right)^2$$

Position sensor signals and reference signal are noisy. A Gaussian filtering is applied to remove high frequency variations ( $\sigma = 1$ ). Then each signal is approximated using B-splines. Accurate gradient estimation is performed using the analytical formulation of every signal obtained from B-spline parametrization. The continuous parametrization of the signals allows the estimated latency to be lower than the image acquisition rate.

As outliers may perturb the latency estimation, robust estimators are introduced in order to reject points with high gradient value for all position signals. The robust formulation takes into account only the position signals which take part into the visible changes in the image and thus in the reference signal variations. We chose to use M-estimators for their proven effectiveness. Contrary to the spatial calibration where the number of outliers might be high (an where the LTS estimator was needed so as to reject as much as 50% of outliers), we expect that outliers will be limited in our case because the position signal has been filtered and parametrized. In that case, the M-estimator, whose rejection rate is lower than the LTS, is more adequate. Let  $y = \{y_i, 1 \leq i \leq m\}$  be the data set with  $y_i = f(\theta, x_i) + r_i$ . Parameters  $\theta$  are estimated taking into account the data  $x_i$  and the noise  $r_i$ . The principle of these estimators consists in minimizing the sum of the residuals:  $\hat{\theta} = \arg \min_{\theta} E(\theta)$  with  $E(\theta) = \sum_i \rho(y_i - f(\theta, x_i))$ . The function  $\rho$  is called M-estimator. Additional details about properties of M-estimators can be found in [18].  $\sigma$  is fixed arbitrarily at 5. We experienced that the method leads to comparable results for a large range of variation of parameter  $\sigma$ .

In addition, we introduce a confidence measure for the points of interest. Basically, we aim at retaining only peaks, i.e. points that are significantly informative. This is motivated by the complexity of the image sequences (noise and low frame rate). A quality measure of the points of interest is proposed to improve the robustness and is defined as:  $q(x) = \frac{1}{n} \sum_{i=1}^n \left( \frac{dsr}{dt}(x) - \frac{dsr}{dt}(x_i) \right)^2$ , where  $x_i$  is a neighbor of  $x$ ,  $n$  is the number of neighbors considered. The larger  $q(x)$ , the more interesting  $x$ . A small  $q(x)$  corresponds to a flat area which is

not relevant for matching. The zero gradient point selection is carried out by retaining only points for which the  $q$  value is large, corresponding to "peaks". The threshold is a percentage of the set of the extracted points of interest.

### 3.3 QUANTITATIVE EVALUATION

#### 3.3.1 Introduction

Accurate calibration is critical for quantitative image analysis. Validation is however difficult, since the true calibration parameters are unknown, and evaluation criterion that were proposed reflect calibration errors, but also other types of errors due to the system components like position sensor errors, alignment errors and segmentation errors. Validation encompasses several aspects:

- Calibration reproducibility was proposed by [140] using the following criterion:  $\Delta \mathbf{x}^t = \|T_{r1}\mathbf{x}_r - T_{r2}\mathbf{x}_r\|$ , where  $\mathbf{x}_r$  is a corner point of B-scan or a variant (image center, or the worst image corner depending on the paper),  $T_{r1}$  and  $T_{r2}$  two calibration transformations for the same ultrasound sequence.  $\Delta \mathbf{x}^t$  is the reproducibility measure. When  $\Delta \mathbf{x}^t$  is close to zero, the reproducibility of the calibration method is good.
- Calibration precision was used by some groups [19, 22, 46, 120, 138] and amounts to scanning a point from different positions. The point location in each image being transformed in the 3D space, a set of  $N$  points is obtained, and the precision is measured via the compacity of the point set:  $\mu = \frac{1}{N} \sum_i |T_{2D \rightarrow 3D} p_i - \bar{p}|$ , where  $\bar{p}$  is the center of mass of the  $N$  points  $p_i$ .
- Calibration accuracy usually refers to the previous method, except that the 3D position of the point is known, for instance by using a pointer.

With Wiro Niessen and colleagues at Utrecht University, we have proposed different criteria (point, distance, volume and shape) to assess three calibration methods, namely the one presented here, the stradx method [140] and the calibration method implemented in the medtronic neuronavigation system [21].

#### 3.3.2 Evaluation criteria

We have proposed point, distance, volume and shape criteria to evaluate the calibration methods:

- The first criterion evaluates the performance of point localization in 3D space. This criterion is crucial for navigation accuracy using 3D reconstructed ultrasound data. A single point phantom was used to perform this evaluation [46, 102]. It consists of a spherical bead with a diameter of 1.5mm attached to the bottom of a water bath. The bead was imaged through water from different positions. The spatial precision was evaluated from different view points. Since the bead position is unknown, only the variation in position and not the localization accuracy could be assessed. For image acquisition, the US probe was aligned for optimal imaging of the bead. Using different positions and orientations, this was repeated six times for each depth. Six depths were used: 6, 7, 8, 9, 10 and 12 cm, leading to in total 36 3D position measurements. The spherical

bead position were detected manually in the 2D images. The manual detection has been checked by two experts. The 3D location of these points were computed using each of the three calibration matrices (the calibration matrix maps the 2D position to the 3D position). For each calibration, the mean error between the mean location and the whole measurement set was computed.

- The second and third criteria evaluate the capability of measuring distances and volumes. While calibration evaluation is generally performed on point sets, the accuracy of distance and volume measurements is very important to evaluate in the context of 3D ultrasound. A CIRS, Inc. <sup>1</sup> 3D ultrasound calibration phantom was used which contains two calibrated volumetric egg-shaped test objects. The characteristics of this egg are the length of the axes and the volume. The respective axes lengths of the egg are 3.9cm and 1.8cm, and the total volume of the egg is 6.6162 cm<sup>3</sup>. For image acquisition of the CIRS, Inc. phantom, four depths were used: 6, 8, 10 and 12 cm. For each depth, two different probe motions were used: translational motion and fan-like motion. The distance measurements were performed using the StradX software. Once the calibration parameters were loaded, the two axes of the egg were measured using the StradX reslicing facility. The axis lengths were then measured in the resliced planes using the StradX measurements facility.
- The volume estimation has been performed using two methods: based on the axis lengths and based on the manual segmentation. Owing to the simple egg shape, its estimated volume  $\hat{V}$  can be computed from the axes using the following equation:  $\hat{V} = \frac{4}{6}\pi.a_2^2.(a_1^+ + a_1^-)$  (the volume of the egg is the sum of two volumes of half ellipsoids, where  $a_1^+ = 2.7cm$ ,  $a_1^- = 1.2cm$  and  $a_2 = 0.9cm$ ). Manual segmentation was performed using the StradX software. Egg contours were segmented every three images and smoothly interpolated by StradX. Since the segmentation is intrinsically 2D, this step does not depend on calibration parameters. Therefore, the manual delineation is exactly the same for each evaluated calibration method. Finally, the egg volume was estimated from the segmentation using StradX volume estimation facility.
- We investigated the use of a shape based criterion to assess the accuracy of the tested calibration methods. The surface of the egg  $\mathcal{S}$  is defined by the point set satisfying the following implicit equation:  $f(x, y, z) = \left(\frac{x}{a_1}\right)^2 + \left(\frac{y}{a_2}\right)^2 + \left(\frac{z}{a_2}\right)^2 = 1$ , where  $a_1 = 2.7cm$  if  $x > 0$ ,  $a_1 = 1.2cm$  if  $x < 0$ , and  $a_2 = 0.9cm$ . A least-square fitting method was used and enables to compute an analytic distance between a point and the implicit surface. The radial Euclidean distance [12, 32] is the distance between the point P and the intersection of the OP line and the surface, where O is the egg center. The radial Euclidean distance  $d$  of a point  $P(x, y, z)$  to the surface  $\mathcal{S}$  is given by the following equation:  $d(P, \mathcal{S}) = ||OP|| * |1 - f^{\frac{1}{2}}(x, y, z)|$ . The estimation of the center of the egg is performed by minimizing the radial Euclidean distance between the point set and the

<sup>1</sup><http://www.cirsinc.com>

estimated shape. Then, the shape criterion was obtained by computing the the mean radial Euclidian distance between the point set provided by the manual segmentation and the model of the egg-shaped object, constrained with a fixed and known axis length.

### 3.3.3 Results

This section will provide only a summary of the obtained results that are considered as the most significant. The interested reader is referred to [149] for detailed results.

- *Point localization.* The results for 3D point localization can be seen in Table 3.1. Results are averages over six depths (6, 7, 8, 9, 10 and 12 cm). Mean error, standard deviation, maximum error and median error are given in *mm*. The mean error varies between 1.6 *mm* (Medtronic and Rennes) and 2.7 *mm* (Stradx). As can be seen, Medtronic and Rennes methods provide similar results.
- *Volume measurement.* For each of the 16 image sequences (4 depths, two acquisitions per probe movement (translation and fan)), the egg-shaped object volume has been estimated using both the estimated axes lengths and a manual segmentation method. Results are indicated in Table 3.2. Using manual segmentation, volume estimation varies between 91.82% (Stradx) and 105.20% (Medtronic) of the theoretical volume. Using axes length-based method, results varies between 81.87% (Stradx) and 89.60% (Medtronic).
- *Shape criterion.* The radial Euclidean distance between the egg shape and the point set provided by the manual segmentation has been computed for each of the 16 image sequences. Results are indicated in Table 3.3. The best results were achieved by StradX and Rennes methods with a mean distance of 0.069*cm* and 0.067*cm* respectively.

Calibration method	Mean	Std. Dev.	Max	Median
Medtronic	1.62	0.67	3.13	1.56
Stradx	2.70	0.92	4.87	2.58
Rennes	1.67	0.66	3.29	1.52

Table 3.1: Evaluation of the 3D point localization criterion. The results are given in *mm*.

## 3.4 DISCUSSION

In this chapter, a robust feature extraction method was presented. The extracted features (the water bath, represented by either points or lines) have been used to perform spatial and temporal calibration of tracked 3D freehand ultrasound. In addition, it was shown that mis-calibration directly impacts quantitative processes like distance, volume and shape measures.

Calibration is crucial for quantitative measures. At first glance, one could expect that calibration errors could be compensated by rigid registration. That

Calibration method	Mean	Std. Dev.
Manual segmentation-based method		
Medtronic	6.96 (105.20 %)	0.19 (2.93 %)
Stradx	6.08 (91.82 %)	0.28 (4.24 %)
Rennes	6.54 (98.83 %)	0.20 (3.06 %)
CT-scan data	6.66 (100.6%)	0.20 (3.06%)
Axis length-based method		
Medtronic	5.93 (89.60 %)	0.30 (4.54 %)
Stradx	5.42 (81.87 %)	0.40 (6.03 %)
Rennes	5.86 (88.51 %)	0.21 (3.15 %)
CT-scan data	6.18 (93.40%)	0.55 (8,31%)

Table 3.2: *Volume measurements of the test object as a function of the calibration methods and the volume estimation method. Results are given in  $\text{cm}^3$  with between brackets the percentage that each measure represents compared to the manufacturer specifications (the total volume of the test object is  $6.62 \text{ cm}^3$ ).*

Calibration method	Mean Error	Std. Dev.
Medtronic	0.074	0.026
Stradx	0.067	0.021
Rennes	0.069	0.019

Table 3.3: *Shape criterion computed using different calibration methods and from the CT scans. The radial Euclidean distance has been computed between the point set provided by manual segmentation and the model of the egg-shaped object. Results are given in  $\text{cm}$ . Volume computation (in  $\text{cm}^3$ ) based on axis estimation (in  $\text{cm}$ ) is also given with between brackets the percentage that each measure represents compared to the manufacturer specifications.*

could be the case for a pure translational probe motion which is unlikely to occur in clinical practice. Due to the coupling between translations and rotations, mis-calibration will cause B-scan planes to be mutually mis-aligned, and after reconstruction, this mis-alignment cannot be corrected for easily.

For the image-guided neurosurgery application, we have acquired ultrasound images thanks to the sononav module provided by Medtronic. At the time the work on calibration was carried out, this module was not available. However, for pragmatic and legal reasons, it was more convenient to acquire the ultrasound images through the neuronavigation system already used in neurosurgery. As a consequence, we could not use our calibration technique and were bound to the calibration of the commercial system.



## 4.1 INTRODUCTION

### 4.1.1 Motivation

To analyze the sequences of B-scans, two types of approaches can be used: the reslicing (without reconstruction) or the true 3D reconstruction including interpolation step. The first is used by the StradX system [141] and enables the analysis of the data without reconstruction. The sequence of B-scans can be arbitrarily resliced and distance/volume measurements are performed without reconstruction. This strategy is very powerful for manual analysis of 3D datasets. However, 3D isotropic reconstruction is still necessary in clinical context when automatic segmentation or registration procedures are required. The second approach is based on the interpolation of the information within the B-scans to fill a regular 3D lattice thus creating a volumetric reconstruction. Due to the non uniform distribution of the B-scans, this step is acutely expensive with respect to computation time and reconstruction quality: an efficient reconstruction method should not introduce geometrical artifacts, degrade nor distort the images.

### 4.1.2 Related work

A review of freehand reconstruction method was published recently [160], while reviews of medical image interpolation were also published earlier [101]. Methods can be grossly sorted into voxel-based methods, pixel-based methods and function-based methods:

- Voxel based method consist in parsing the reconstructed volume and interpolating the intensity from the set of input  $2D$  images, either with no interpolation (Voxel Nearest Neighbor) [158], or higher order interpolation [16, 166, 169]. Among this class, the registration-based interpolation [133, 134] may also be included, where the registration between two slices is taken into account to interpolate linearly.
- Pixel-based methods proceed in two steps: first, input  $2D$  pixels are distributed in the  $3D$  volume, and second, a hole-filling step is performed. The bin-filling step can be done using pixel nearest neighbor [61, 124], maximum value [124], first value [129] or last value [169]. The hole filling step may use a local neighbourhood [78, 84, 124], a  $3D$  kernel around filled voxels [84, 93] or a  $3D$  kernel around input pixels [14, 60, 114, 129].
- Function-based methods are used to interpolate intensity values through the input pixels and fill the  $3D$  volume. The interpolation function may

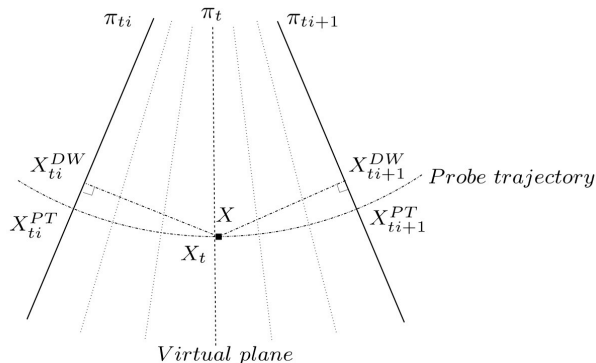


Figure 4.1: Illustration of DW and PT principles. The two orthogonal projections for DW interpolation method and the construction of a “virtual” plane  $\pi_t$  containing  $X$  for PT method.

be either explicit, like radial basis function [148] or implicit using Bayesian techniques [155].

## 4.2 RECONSTRUCTION METHOD

This work builds on the distance weighted interpolation and proposes to incorporate probe trajectory information. The distance weighted interpolation is first presented in section (4.2.1). Then, the probe trajectory information is incorporated in section (4.2.2).

### 4.2.1 Distance Weighted Interpolation

At each point  $X$  of the reconstructed volume, the linear interpolation amounts to computing:  $f_n(X) = \frac{1}{G} \sum_{ti \in K_n(X)} g_{ti} \tilde{f}(X_{ti})$ , where  $K_n$  is the interpolation kernel. In other words,  $K_n$  is the set of the different indexes of the B-scans that are involved in the interpolation,  $n$  is the interpolation order. For a given interpolation degree, the  $n$  closest B-scans before  $X$  and the  $n$  closest B-scans after  $X$  are considered. For the DW interpolation,  $X_{ti}$  is the orthogonal projection of  $X$  on the  $ti^{th}$  B-scan.  $\tilde{f}(X_{ti})$  is the intensity at position  $X_{ti}$  and is obtained by bilinear interpolation. Finally,  $G$  is the normalization constant with  $G = \sum g_{ti}$ , where  $g_{ti}$  is the distance between  $X$  and  $X_{ti}$  (see Fig. 4.1).

### 4.2.2 Probe Trajectory Interpolation

The orthogonal projection of points to the nearest B-scans is a straightforward solution. However, it does not take into account the relationship between a given point and its projections. As seen in section 4.1, registration based interpolation uses homologous points to interpolate, thus increasing the computational burden. We propose to incorporate the probe trajectory into the interpolation process. In other words, homologous points are defined as being successive points along the probe trajectory.

We believe there is correlation between the underlying signal structure and the probe trajectory. When imaging cross-sections of a tubular structure for instance, the intuitive displacement of the probe that follows the Structure

Of Interest (SOI) will lead to some correlation between the probe trajectory and the anatomical structure. In intra-operative exams, we observed that the surgeon was concentrated in keeping the focus of the US scans on the SOI (i.e. the lesion). This is confirmed by observing the location of the SOI, which is kept at the same position in the x-y plane during the sequence (see Fig. 4.2). Therefore, we think that the introduction of probe trajectory into the

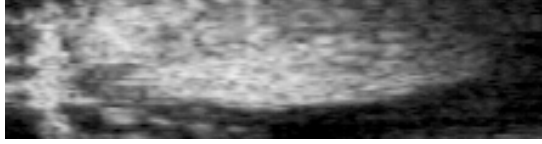


Figure 4.2: A longitudinal reslice of the non reconstructed intra-operative data (i.e. the stack of B-scans). The x position in B-scans (horizontal axis of the reslice) of the structure of interest is correlated along the sequence, the vertical axis of the reslice corresponding to the B-scans latencies. The cerebral falx is visible at left and the lesion at center.

interpolation process is relevant.

Instead of using orthogonal projections as in classical DW, we propose to project along the probe trajectory. Firstly, the time stamp  $t \in \mathbb{R}$ ,  $t \in [t_i, t_{i+1}]$  of the “virtual plane”  $\pi_t$  is estimated. The “virtual plane” is the plane which passes through  $X$  in the sense of the probe trajectory (see Fig 4.1). Then,  $t$  is used to compute the “virtual plane” parameters (translation and rotation) by interpolation of  $\pi_{t_i}$  and  $\pi_{t_{i+1}}$  positions. Finally, the 2D coordinates of  $X_t$  (the projection of  $X$  on  $\pi_t$ ) are used to obtain the projections of  $X$  on  $\pi_{t_i}$  and  $\pi_{t_{i+1}}$  in the sense of the probe trajectory.

#### 4.2.2.1 Determination of the “virtual” plane time stamp

Under the assumption that the probe motion is constant between two consecutive B-scans, the latency ratio is equal to the distance ratio:

$$t = \frac{d_{t_{i+1}}}{d_{t_i} + d_{t_{i+1}}}(t_i) + \frac{d_{t_i}}{d_{t_i} + d_{t_{i+1}}}(t_i + 1) \quad (4.1)$$

where  $d_{t_i}$  is the distance (in the sense of orthogonal projection) between the current voxel and the B-scan of time stamp  $t_i$  ( $d_{t_i} = \|X - X_{t_i}^{DW}\|$ ). The assumption of constant probe speed between two slices is justified by the frame rate. The lowest frame rate is usually 10Hz, which means that 100ms separate two frames. It is therefore reasonable to assume a constant motion magnitude between two frames (i.e. no significant acceleration). Once the time stamp of the “virtual” plane is computed, the probe position can be interpolated.

#### 4.2.2.2 Determination of the “virtual” plane parameters

The position of each B-scan is defined by 3 translations and 3 rotations. Thus the interpolation of origin position and rotation parameters is needed. We use the Key interpolation for the translations and the Spherical Linear Interpolation (SLERP) for the rotations.

*Interpolation of origin position.* For the origin of the B-scan, a cubic interpolation is used to estimate the origin of the “virtual” plane at time stamp  $t$ . The Key function is used to carry out a direct cubic interpolation and is defined as:

$$\varphi(t) = \begin{cases} (a+2)|t|^3 - (a+3)t^2 + 1 & \text{if } 0 \leq |t| < 1, \\ a|t|^3 - 5at^2 + 8a|t| - 4a & \text{if } 1 \leq |t| < 2, \\ 0 & \text{if } 2 \leq |t| \end{cases} \quad (4.2)$$

With  $a = -\frac{1}{2}$ ,  $\varphi$  is a  $C^1$  function and a third order interpolation is obtained [165]. In practice, four B-scans are used for cubic interpolation. This seems to be an optimal trade-off between computational time and reconstruction quality. For example, the interpolation of the origin position along  $x$  axis  $T_x$  reads as:

$$T_x(t) = \sum_{k=t_i-1}^{t_i+2} T_x(k)\varphi(t-k) \quad (4.3)$$

*Interpolation of rotation parameters.* The rotation parameters of each B-scan are converted into a quaternion which is a compact representation of rotations within a hyper-complex number of rank 4:  $q = w + ix + jy + kz$ . This representation of rotations, allows to take into account the coupling of rotations during the interpolation step. The quaternion representing the rotations of the “virtual” plane is obtained through a Spherical Linear Interpolation (SLERP) [159] at time stamp  $t$ :  $q_t = q_{t_i} \frac{\sin((1-t)\theta)}{\sin\theta} + q_{t_{i+1}} \frac{\sin(t\theta)}{\sin\theta}$ , where  $q_{t_i}$  and  $q_{t_{i+1}}$  are the unit quaternions corresponding to B-scans of time stamps  $t_i$  and  $t_i + 1$ ; and  $\theta$  represents the angle between  $q_{t_i}$  and  $q_{t_{i+1}}$  computed as:  $\theta = \cos^{-1}(q_{t_i} \cdot q_{t_{i+1}})$ . The orientation of the “virtual” plane is contained in  $q_t$ . Then,  $X_{t_i}^{PT}$  and  $X_{t_{i+1}}^{PT}$  are obtained directly, since they have the same 2D coordinates (defined in each B-scans) as  $X_t$ .

### 4.3 RESULTS

#### 4.3.1 Simulated intra-operative sequences

In freehand ultrasound imaging, like in other contexts, validation is not easy because the “ground truth” does not exist. In order to overcome this problem, magnetic resonance sequences were built on geometry of the ultrasonic intra-operative sequences. Firstly, the intra operative trajectories were used to re-slice the preoperative magnetic resonance volume of the patient. Then, a stack of MR-scans was built on the images obtained by the re-slicing. Finally, the reconstructed MR volume was compared to the “ground truth” (i.e the corresponding preoperative MRI volume). As the US-sequences, the MR-sequence1 is composed of 59 MR-scans ( $223 \times 405$ ) and MR-sequence2 of 46 MR-scans ( $223 \times 405$ ).

Since the “ground truth” is known, the validation metric directly compares the reconstructed volume  $\tilde{V}$  and the corresponding volume  $V$  in preoperative MRI. Firstly, the MR sequence, obtained by reslicing the pre-operative MRI accordingly to the US trajectory, was reconstructed with the three evaluated methods (VNN, DW and PT). Secondly, the corresponding MR volume  $V$  (in terms of field of view and resolution) was computed using cubic interpolation.

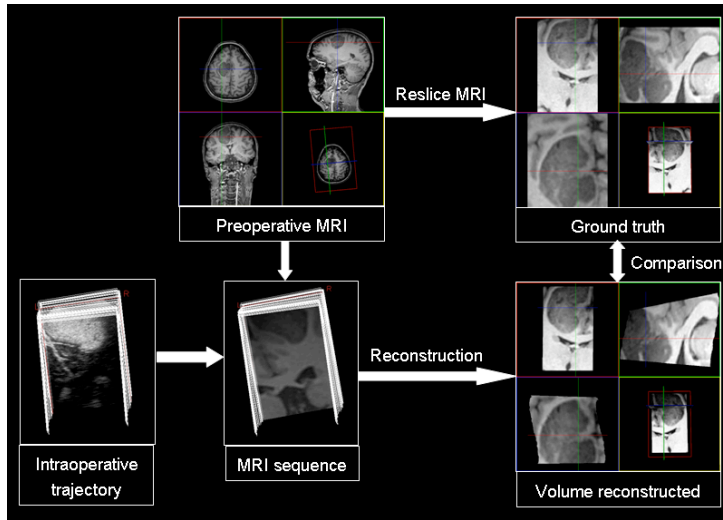


Figure 4.3: Illustration of the validation framework used for the MR-sequences.

Finally, the reconstructed volumes obtained with VNN, DW and PT were compared to the “ground truth”  $V$  (see Fig. 4.3) by the means of Mean Square Error.

Figure 4.4 shows the influence of the mean distance between two consecutive B-scans on the reconstruction error. The mean square error is computed between the “Ground Truth” and the reconstructed volume. The PT method outperforms the VNN and DW approaches especially on sparse data. Figure 4.5 presents slices extracted from initial MR volume and the reconstructed MR volume. Visually, the PT method more preserves edges and contrast. Compared to DW method, the PT method improves the reconstruction result especially on edges whose direction is correlated with probe trajectory.

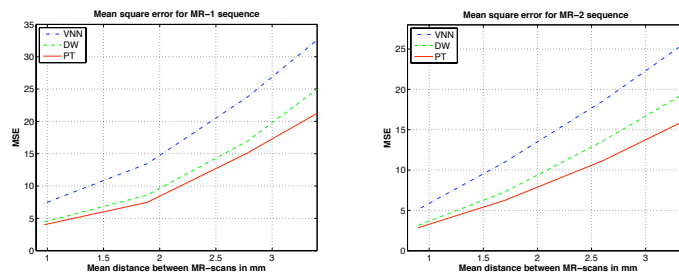


Figure 4.4: Variation of mean reconstruction error relatively to the distance between two consecutive MR-scans with interpolation degree of 1. Left MR-sequence1, right MR-sequence2. Three methods are evaluated: VNN, DW and PT. The PT method outperforms others methods especially on sparse data.

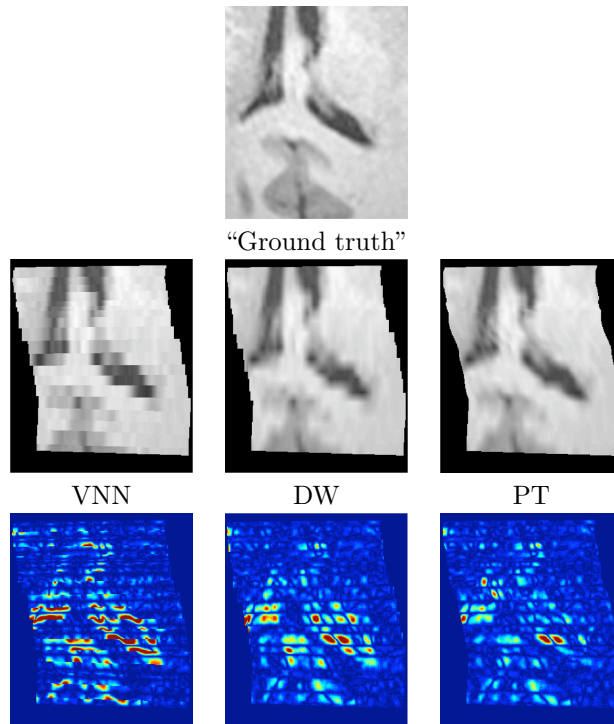


Figure 4.5: Results for MR-sequences of brain. Top: the “ground truth” and the reconstructions obtained *via* the different methods for a mean distance between MR-scans of  $1.8mm$ . On the bottom: the images of the difference between the “ground truth” and the reconstructed volume. Visually, the PT method preserves more the edge continuity and the contrast. The difference images show that the PT method creates less artifacts and appears closer to the “ground truth”, especially on ventricles edges.

### 4.3.2 Ultrasound intra-operative sequences

For intra-operative sequences, the sonosite cranial probe was coupled with the Sononav Medtronic system. The sequences were acquired during neurosurgical procedures after the craniotomy step but before opening the dura. US-sequence1 is composed of 59 B-scans ( $223 \times 405$ ) and US-sequence2 of 46 B-scans ( $223 \times 405$ ).

The reconstructions of B-scans dataset US-sequence1 are presented in Figure 4.6 and US-sequence2 are presented in Figure 4.7. Visually, the VNN method leads to many discontinuities and creates artificial boundaries (see image at the top right of Fig. 4.7). The DW method generally smooths out the edges and spoils the native texture pattern of US image more than PT (see at the bottom of Fig. 4.7).

## 4.4 DISCUSSION

In this chapter, we have proposed a new method to reconstruct 3D freehand ultrasound images. This method incorporates probe trajectory into the re-

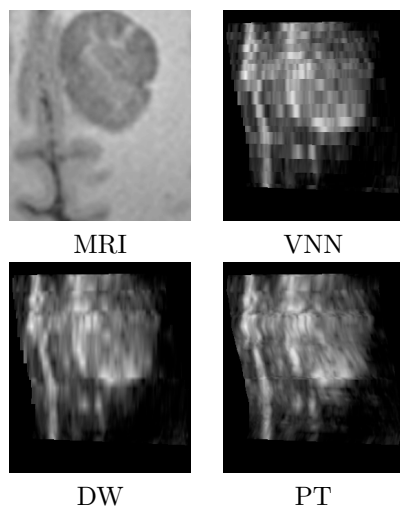


Figure 4.6: Results for US-sequence1 of brain. Top: the preoperative MRI and the US reconstruction obtained with the VNN method. On the bottom: the reconstruction obtained with DW and PT approaches. The low-grade glioma and the cerebral falx appear in gray in MR image and in white in US images. From left to right the VNN, DW and PT methods. The images highlight the inherent artifacts of VNN (i.e. discontinuities) and DW (i.e. blur) methods. These results underline that the PT method preserves the edges continuity and the native texture of US image more than VNN and DW method.

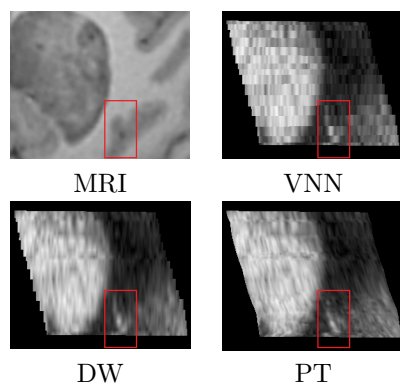


Figure 4.7: Results for US-sequence2 of brain. Top: the preoperative MRI and the US reconstruction obtained with the VNN method. On the bottom: the reconstruction obtained with DW and PT approaches. The low-grade glioma appears in gray in MR image and in white in US images. Visually, the PT method preserves more the edges continuity especially on sulci edges (see at the center bottom of images).

construction process. Validation has been performed using a simulated MR sequence, computed from a real MR image and a real intraoperative trajectory. Experiments have been conducted on real intraoperative data and have shown that this method offers a good tradeoff between reconstruction quality and computation time. It can be noted that this technique is suited for GPU computation facility since the method is intrinsically parallel. By doing so, a real-time reconstruction technique would be available.

Extensive validation and comparison between reconstruction techniques of 3D freehand ultrasound has never been proposed to the best of our knowledge, as opposed to general reconstruction and interpolation techniques [64, 115]. Offering validation data and validation metrics to the community would yet be beneficial. Data that were used for our validation could be disseminated. In particular, this would give the opportunity to compare 3D freehand ultrasound reconstruction techniques.

## 5.1 INTRODUCTION

Ultrasound is an appealing imaging modality because it is real-time, non-invasive, cheap, light in the operating room. The main issue is image quality that is sensitive to many artifact. Among them, the acoustic wave is totally reflected when it reaches a boundary separating two layers of very different acoustic impedance. As a consequence, air interfaces and bone interfaces lead to an almost total reflection of the signal.

In addition, ultrasound images are corrupted by a strong noise, often called speckle. This noise is due to complex interactions between the acoustic wave and local scatterers, the wave energy being either diffused, or reflected. Modeling ultrasound image noise is of high interest to be incorporated in image processing methods like segmentation, registration, denoising, *etc.* However, modeling the ultrasound image formation, either with a physics-based approach or a statistical approach, is difficult.

Filling the gap between ultrasound wave propagation to ultrasound image noise is very challenging. With simplification hypothesis, many models have been proposed, ranging from simple Rayleigh to complex k-homodyne distribution [7, 33, 53, 63, 83, 113, 118, 142, 143, 174, 176]. Physics-based modeling are relevant when the raw RF signal is available. More commonly, the acquired signal is an analog video signal from the ultrasound machine. Then, the signal has endured some processing: logarithm amplification of radio-frequency signals performed on the display image [1]; additive Gaussian noise of sensors [1]; additive Gaussian noise introduced by the acquisition card and probably image processing techniques (filtering, enhancement) implemented by the manufacturer.

Due to the complexity of determining a good noise model, let us first express the expected characteristics of such good model:

- The noise amplitude should be correlated with the signal, since we observe that the noise is higher in hyperechogenic areas in ultrasound images.
- The noise model can be manipulated analytically. For instance, the K-homodyne model is too complex to be used, while the Rice or Rayleigh model are adequate.
- The model should be generic enough to comply with log compression.

For these reasons, we have used a simple yet efficient noise model in this section. This model reads as:

$$u(x) = v(x) + v^\gamma(x)\eta(x) \quad (5.1)$$

where  $v(x)$  is the original image,  $u(x)$  is the observed image,  $\eta(x) \sim \mathcal{N}(0, \sigma^2)$  is a zero-mean Gaussian noise. This model is more flexible and less restrictive than the usual RF model and is able to capture reliably image statistics since the factor  $\gamma$  depends on ultrasound devices and additional processing related to image formation.

Contrary to additive white Gaussian noise model, the noise component in (5.1) is image-dependent. In [109], based on the experimental estimation of the mean versus the standard deviation in Log-compressed images, Loupas *et al.* have shown that  $\gamma = 0.5$  model fits better to data than the multiplicative model or the Rayleigh model. Since, this model has been used successfully in many studies [9, 66, 95, 173]. Clearly, this model is relevant since it is confirmed that the speckle is higher in regions of high intensities versus regions of low intensities [95, 162].

In this chapter, this noise model will be used in a Bayesian formulation of the *NL-means* filter, and will then be used to detect acoustic shadows in ultrasound images.

## 5.2 DENOISING

### 5.2.1 Introduction

The speckle in US images is often considered as undesirable and several noise removal filters have been proposed. Unlike the additive white Gaussian noise model adopted in most denoising methods, US imaging requires specific filters due to the signal-dependent nature of the speckle intensity. In this section, we present a classification of standard adaptive filters and methods for speckle reduction.

#### 5.2.1.1 Adaptive Filters

The adaptive filters are widely used in US image restoration because they are easy to implement and control. The commonly-used adaptive filters - the Lee's filter [100], Frost's filter [57], and Kuan's filter [98] - assume that speckle noise is essentially a multiplicative noise. Many improvements of these classical filters have been proposed since. At the beginning of the 90's, Lopes *et al.* [108] suggested to improve the Lee's and Frost's filters by classifying the pixels in order to apply specific processing to the different classes. Based on this idea, the so-called Adaptive Speckle Reduction filter (ASR) exploits local image statistics to determine specific areas to be processed further. In [85], the kernel of the adaptive filter is fitted to homogeneous regions according to local image statistics. Analyzing local homogeneous regions was also investigated in [94, 130] to spatially adapt the filter parameters. Note that the Median filter has been also examined for speckle reduction in [109]. Very recently, a stochastic approach to ultrasound despeckling (SBF) has been developed in [163, 164]. This local averaging method removes the local extrema assumed to be outliers in a robust statistical estimation framework. Finally, the Rayleigh-Maximum-Likelihood (R-ML) filter has been derived with similar methodological tools in [11].

#### 5.2.1.2 Partial Differential Equations (PDE) -based approaches

Adapted formulations of the Anisotropic Diffusion filter (AD) [135] and the Total Variation minimization scheme (TV) [154] have been developed for US

imaging. In [178, 179], the Speckle Reducing Anisotropic Diffusion (SRAD) was introduced and involves a noise-dependent instantaneous coefficient of variation. In [1] the Nonlinear Coherent Diffusion (NCD) filter is based on the assumption that the multiplicative speckle in US signals is transformed into an additive Gaussian noise in Log-compressed images. Recently, the Oriented SRAD (OSRAD) filter has been proposed in [96]; this filter takes into account the local directional variance of the image intensity, i.e., the local image geometry. Finally, the TV minimization scheme has been adapted to ultrasound imaging in [47, 157]. Unlike the previous adaptive speckle filters, all the considered PDE-based approaches are iterative and produce smooth images while preserving edges. Nevertheless, meaningful structural details are unfortunately removed during iterations.

#### 5.2.1.3 Multiscale methods

Several conventional wavelet thresholding methods [34, 48, 49] have also been investigated for speckle reduction [58, 126, 182] with the assumption that the logarithm compression of US images transforms the speckle into an additive Gaussian noise. In order to relax this restrictive assumption, Pizurica *et al.* [137] proposed a wavelet-based Generalized Likelihood ratio formulation and imposed no prior on noise and signal statistics. In [2, 17, 56, 65], the Bayesian framework was also explored to perform wavelet thresholding adapted to the non-Gaussian statistics of the signal. Note that other multiscale strategies have been also studied in [3, 177, 181] to improve the performance of the AD filter; in [4], the Kuan's filter is applied to interscale layers of a Laplacian pyramid.

#### 5.2.1.4 Hybrid approaches

The aforementioned approaches can be also combined in order to take advantage of the different paradigms. In [66], the image is preprocessed by an adaptive filter in order to decompose the image into two components. A Donoho's soft thresholding method is then performed on each component. Finally, the two processed components are combined to reduce speckle. PDE-based approaches and a wavelet transform have been also combined as proposed in [127].

### 5.2.2 NL-means

In this section, the formulation of the *NL-means* method is briefly recalled. Then, the method is adapted to incorporate the dedicated ultrasound noise model.

The previously mentioned approaches for speckle reduction are based on the so-called *locally adaptive recovery paradigm* [55]. Nevertheless, more recently, a new *patch-based non local recovery paradigm* has been proposed by Buades *et al* [24]. This new paradigm proposes to replace the local comparison of pixels by the non local comparison of patches. Unlike the aforementioned methods, the so-called *NL-means* filter does not make any assumptions about the location of the most relevant pixels used to denoise the current pixel. The weight assigned to a pixel in the restoration of the current pixel does not depend on the distance between them (neither in terms of spatial distance nor in terms of intensity distance). The local model of the signal is revised and the authors consider only information redundancy in the image. Instead of comparing the intensity of the pixels, which may be highly corrupted by noise, the *NL-means* filter analyzes the patterns around the pixels. Basically, image patches are

compared for selecting the relevant features useful for noise reduction. This strategy leads to competitive results when compared to most of the state-of-the-art methods [23, 41, 86–88, 90, 111].

In the original *NL-means* filter [24], the restored intensity  $NL(u)(x_i)$  of pixel  $x_i$ , is the weighted average of all the pixel intensities  $u(x_j)$  in the image  $\Omega^{dim}$ :

$$NL(u)(x_i) = \sum_{x_j \in \Omega^{dim}} w(x_i, x_j) u(x_j) \quad (5.2)$$

where  $dim$  denotes the image grid dimension ( $dim = 2$  or  $dim = 3$  respectively for 2D and 3D images),  $\Omega^{dim} \subset \mathbb{R}^{dim}$  is the bounded image domain,  $w(x_i, x_j)$  is the weight assigned to value  $u(x_j)$  for restoring the pixel  $x_i$ . More precisely, the weight evaluates the similarity between the intensities of the local neighborhoods (patches)  $\mathcal{N}_i$  and  $\mathcal{N}_j$  centered on pixels  $x_i$  and  $x_j$ , such that  $w(x_i, x_j) \in [0, 1]$  and  $\sum_{x_j \in \Omega^{dim}} w(x_i, x_j) = 1$  (see Fig. 5.1). The size of the local neighborhood  $\mathcal{N}_i$  and  $\mathcal{N}_j$  is  $(2d+1)^{dim}$ . The traditional definition of the *NL-means* filter considers that the intensity of each pixel can be linked to pixel intensities of the whole image. For practical and computational reasons, the number of pixels taken into account in the weighted average is restricted to a neighborhood, that is a “search volume”  $\Delta_i$  of size  $(2M+1)^{dim}$ , centered at the current pixel  $x_i$ .

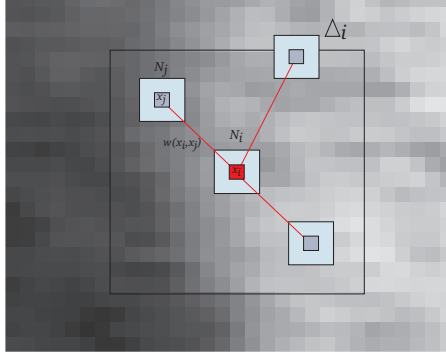


Figure 5.1: **Pixelwise *NL-means* filter** ( $d = 1$  and  $M = 8$ ). The restored value at pixel  $x_i$  (in red) is the weighted average of all intensity values of pixels  $x_j$  in the search volume  $\Delta_i$ . The weights are based on the similarity of the intensity neighborhoods (patches)  $\mathbf{u}(\mathcal{N}_i)$  and  $\mathbf{u}(\mathcal{N}_j)$ .

For each pixel  $x_j$  in  $\Delta_i$ , the Gaussian-weighted Euclidean distance  $\|\cdot\|_{2,a}^2$  is computed between the two image patches  $\mathbf{u}(\mathcal{N}_j)$  and  $\mathbf{u}(\mathcal{N}_i)$  as explained in [24]. This distance is the traditional  $L_2$ -norm convolved with a Gaussian kernel of standard deviation  $a$ . The standard deviation of the Gaussian kernel is used to assign spatial weights to the patch elements. The central pixels in the patch contribute more to the distance than the pixels located at the periphery. The weights  $w(x_i, x_j)$  are then computed as follows:

$$w(x_i, x_j) = \frac{1}{Z_i} \exp - \frac{\|\mathbf{u}(\mathcal{N}_i) - \mathbf{u}(\mathcal{N}_j)\|_{2,a}^2}{h^2} \quad (5.3)$$

where  $Z_i$  is a normalization constant ensuring that  $\sum_{x_j \in \Omega^{dim}} w(x_i, x_j) = 1$ , and  $h$  acts as a filtering parameter controlling the decay of the exponential function.

The main drawback of this filter is its computational burden. In order to overcome this problem, we have recently proposed a fast and optimized implementation of the *NL-means* filter for 3D Magnetic Resonance (MR) images [41] using block-wise approach and adaptive dictionaries.

### 5.2.3 Adaptation to ultrasound noise model

In [88], a Bayesian formulation of the *NL-means* filter was proposed. Equivalent to the conditional mean estimator, it has been shown that an empirical estimator  $\hat{\mathbf{v}}(B_{i_k})$  of a block  $B_{i_k}$  can be defined as (see publications [36, 88] for more details):

$$\hat{\mathbf{v}}(B_{i_k}) = \frac{\sum_{j=1}^{|\Delta_{i_k}|} \mathbf{u}(B_j) p(\mathbf{u}(B_{i_k}) | \mathbf{u}(B_j))}{\sum_{j=1}^{|\Delta_{i_k}|} p(\mathbf{u}(B_{i_k}) | \mathbf{u}(B_j))} \quad (5.4)$$

where  $p(\mathbf{u}(B_{i_k}) | \mathbf{u}(B_j))$  denotes the pdf of  $\mathbf{u}(B_{i_k})$  conditionally to  $\mathbf{u}(B_j)$ . In the case of an additive white Gaussian noise, the likelihood  $p(\mathbf{u}(B_{i_k}) | \mathbf{u}(B_j))$  will be proportional to  $e^{-\frac{\|\mathbf{u}(B_{i_k}) - \mathbf{u}(B_j)\|_2^2}{h^2}}$ , and the corresponding Bayesian estimator  $\hat{\mathbf{v}}(B_{i_k})$  is then similar to the initial *NL-means* method.

The dedicated noise model 5.1 leads to:

$$u(x) | v(x) \sim \mathcal{N}(v(x), v(x)^{2\gamma} \sigma^2) \quad (5.5)$$

which yields

$$p(u(x) | v(x)) \propto \exp - \frac{(u(x) - v(x))^2}{2v(x)^{2\gamma} \sigma^2}. \quad (5.6)$$

Given a block  $B_i$ , the likelihood can be expressed as:

$$p(\mathbf{u}(B_i) | \mathbf{u}(B_j)) \propto \exp - \sum_{p=1}^P \frac{(u^{(p)}(x_i) - u^{(p)}(x_j))^2}{2(u^{(p)})^{2\gamma}(x_j) \sigma^2} \quad (5.7)$$

which amounts to replacing the  $L_2$ -norm by the Pearson distance defined as:

$$d_P(\mathbf{u}(B_i), \mathbf{u}(B_j)) = \sum_{p=1}^P \frac{(u^{(p)}(B_i) - u^{(p)}(B_j))^2}{(u^{(p)})^{2\gamma}(B_j)} \quad (5.8)$$

### 5.2.4 Results

The adapted filter has been tested on a variety of synthetic images with different noise models, and compared to existing methods. Results published in [36] have shown that the adapted *NL-means* outperforms other techniques.

The proposed denoising method was compared visually to the SBF and SRAD filters on real intraoperative brain images. The parameters for the SBF and SRAD filters are the parameters given respectively in [178] and [163]. The

parameters of the OBNLM filter were set as follows :  $h = 8$ ,  $n = 2$ ,  $\alpha = 3$ ,  $M = 6$  and  $\mu_1 = 0.6$ .

Figure 5.2 shows the denoising results. Visually, the OBNLM filter efficiently removes the speckle component while enhancing the edges and preserving the image structures. The visual results produced on real image by our method are competitive compared to SRAD and SBF filters.

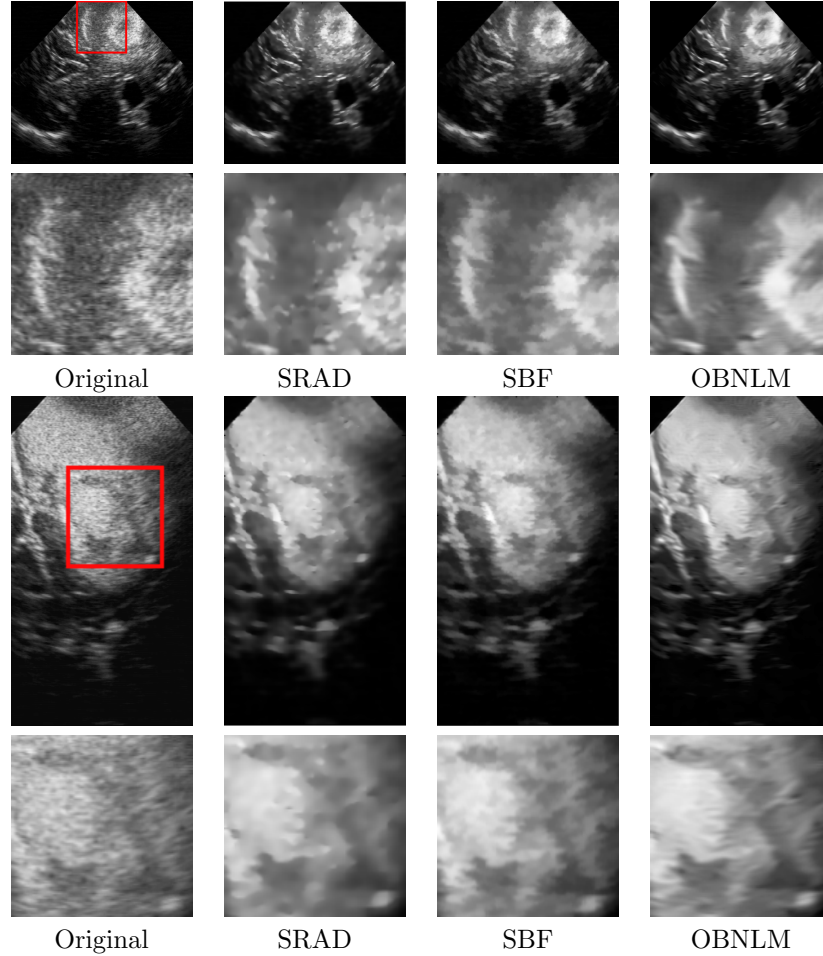


Figure 5.2: Results obtained with the SRAD and SBF filters and the proposed filters on real intraoperative brain images. The OBNLM filter efficiently removes the speckle while enhancing the edges and preserving the image structures.

### 5.2.5 Quantitative analysis on registration accuracy

As stated before, denoising might not be always of interest for clinicians since speckle contains spatial patterns useful for diagnosis. However, speckle is an issue for image processing tasks like image segmentation and registration. Therefore, we have tried to assess the impact of denoising on registration.

### 5.2.5.1 Validation framework

The evaluation framework is based on the warping index criterion proposed in [165] as explained below. Let  $I$  be an image and  $T$  be a geometric transformation. Two transformed images  $I_T$  and  $I_{T^{-1}}$  are computed as follows:  $I_T(x) = I(T(x))$  and  $I_{T^{-1}}(x) = I(T^{-1}(x))$ . These two transformations, coupled with bi-cubic interpolation, introduce similar interpolation artifacts in both images. The warping index  $\omega$  is the distance between the estimated transformation by the registration process  $\hat{R}$  and the true transformation  $R = T \circ T$ :

$$\omega = \frac{1}{|\Omega^{dim}|} \sum_{x \in \Omega^{dim}} \left\| R^{-1}(x) - \hat{R}^{-1}(x) \right\|_2 \quad (5.9)$$

where  $\|\cdot\|_2$  is the  $L_2$ -norm. With several initial transformations, the quality of a registration procedure can be estimated by computing the mean warping index and its variance.

The registration procedure is based on the sum of square differences with a simplex optimization within a multiresolution scheme. The registration procedure is stopped at a 0.4 mm isotropic image resolution level.

### 5.2.5.2 3D intraoperative brain image

The real volume used for this experiment (see Fig. 5.3) is an intraoperative ultrasound image of  $510 \times 432 \times 174$  voxels in size and isotropic resolution of  $0.2mm^3$ .

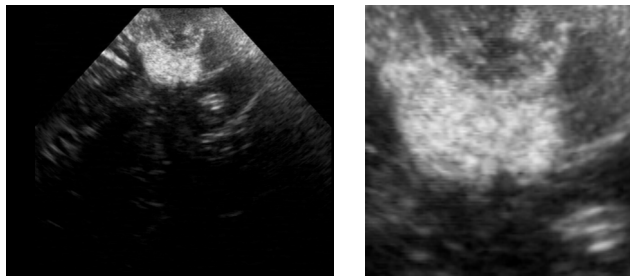


Figure 5.3: 3D intraoperative ultrasound brain image used for the evaluation. Left: original noisy image. Right: zoom on the upper part processing on the lesion.

### 5.2.5.3 Comparison with other denoising methods

During this experiment the TV, AD, SRAD, FROST, NL-means and adapted NL-means filters were successively considered. In this experiment, the mean  $\bar{\omega}$  and the variance  $Var(\omega)$  of the warping index were based on 50 random image registrations with larger transformations. The 50 matrices  $T$  correspond to a translation uniformly distributed in  $[-5, 5]$  mm and a rotation uniformly distributed in  $[-\pi/18, \pi/18]$ . The same initial transformations were used for all denoising methods.

For all methods, the optimal parameters were sought in a large range to ensure that the best result -in terms of registration accuracy- are provided for each denoising method.

Filter	$\bar{\omega}$ (mm)	$Var(\omega)$ (mm)	Success rate
Original image	0.3631	0.0196	94%
AD	0.3048	0.0185	96%
SRAD	0.3003	0.0095	96%
TV	0.2999	0.0092	94%
Frost's filter	0.3330	0.0123	92%
NL-means	0.2961	0.0091	96%
OBNLM	<u>0.2815</u>	<u>0.0075</u>	<u>98%</u>

Table 5.1: Registration accuracy results obtained with the tested filters. The OBNLM filter obtains the best mean and variance of warping index as well as the best success rate.

In order to preserve the homogeneity of samples, the transformations for which at least one filter failed (i.e., the registration between the denoised images with this filter failed) were rejected from the analysis. Among the 50 transformations initially used, only 44 transformations were considered during statistical analysis.

Table 5.1 presents the success rate, the mean  $\bar{\omega}$  and the variance  $Var(\omega)$  of the warping index obtained with the compared filters. These results show that the error rate after registration is smaller with the adapted *NL-means* filter with the best success rate.

A one-way Analysis of Variance (Anova) was used to assess the statistical significance of the observed differences. Figure 5.4 shows the distribution of the warping indexes for all the compared filters. The  $p$ -value obtained with the “*anova1*” function of Matlab was 0.05. This means that at least one sample mean was significantly different than the other sample means.

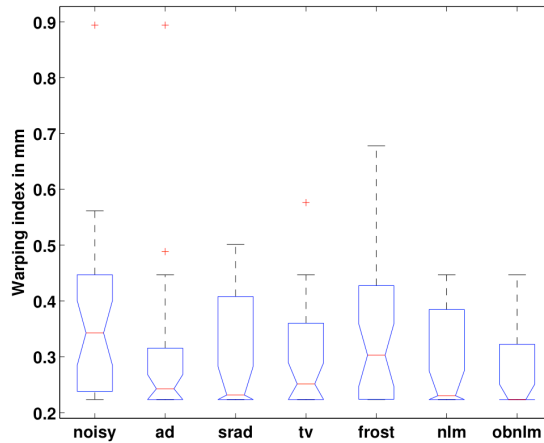


Figure 5.4: ANOVA: distributions of the warping indexes obtained for the AD, the TV, Frost's, the SRAD, the *NL-means* and the OBNLM filters.

Then, a multiple comparison test [77] (Matlab implementation) was per-

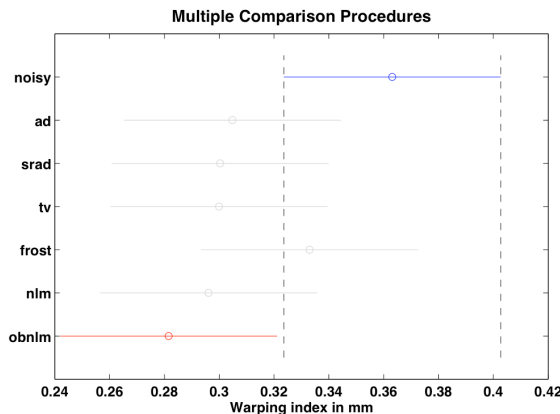


Figure 5.5: Multiple comparison procedures: study of the statistical differences between the warping indexes obtained with the compared methods. By selecting the “noisy” group as reference, only the OBNLM method is statistically different than the other denoising methods in terms of registration accuracy.

formed to determine which method was significantly different from the others. Contrary to paired t-tests between each couple of groups, the multiple comparison procedure provides an upper bound on the probability that any comparison can be incorrectly found significant. By selecting the “noisy” group as reference (i.e. without denoising), the multiple comparison procedures showed that only the OBNLM was significantly different in terms of registration accuracy (see Fig. 5.5).

### 5.3 DETECTION OF ULTRASOUND ACOUSTIC SHADOWS

#### 5.3.1 Introduction

The image formation process of ultrasound images is bound to the propagation and interaction of waves in tissues of various acoustic impedances [161]. More precisely, at the boundary of two materials, the wave energy is transmitted and/or reflected. If the wave energy is almost totally reflected, this will result in an acoustic shadow in the region of the image beyond the boundary. The motivation for detecting acoustic shadows is twofold. First, the presence of an acoustic shadow reflects the presence of an interface where the acoustic energy was almost completely lost. This is typically an interface tissue/air or tissue/bone. Therefore, acoustic shadows are useful to detect calcifications, gallstones or bone structures, detect lesions [52], discriminate benign tumors [167], predict stability of Peyronie’s disease [15] or diagnosis leiomyoma [27]. Secondly, acoustic shadows might limit the efficiency of image processing techniques like segmentation, registration [103, 104, 132] or 3D reconstruction. The automatic processing of ultrasound in a quantitative analysis workflow requires to detect and account for acoustic shadows. This paper will focus on the impact of shadow estimation on image processing tasks and more precisely on 3D reconstruction and 3D registration of ultrasound intraoperative data.

Only a few papers have presented automatic methods to detect acoustic shadows. Methods can be broadly sorted in two groups: intensity-based meth-

ods [52,112] and geometric methods [103,132]. Intensity-based methods rely on a direct analysis of the intensities to detect dark regions. Madabhushi *et al.* [112] describe a method that combines a feature space extraction, manual training and classification to discriminate lesions from posterior acoustic shadowing. Drukker *et al.* [52] use a threshold on a local skewness map to detect shadows. Geometric methods take into account the probe's geometry and analyze intensity profiles along the lines that compose the B-scan. Leroy *et al.* [103] fit an heuristic exponential function to determine whether a shadow occurred, while Penney *et al.* [132] manually estimate the image mask to determine dark areas.

The method proposed in this paper is a hybrid method combining a geometrical approach with a modeling of ultrasound image statistics. Contrary to previous papers, the image mask, the probe geometry and the statistical detection threshold are estimated automatically. Rather than fitting heuristic function to detect shadows, a statistical analysis is performed along each transducer line to detect potential shadows regions. These ruptures (or breaks) along the intensity profiles are tested as potential shadow boundary with a statistical test based on the previously presented noise model 5.1.

### 5.3.2 A geometric and photometric method

The shadow detection procedure consists of two phases. Since the presence of acoustic shadows is bound to the geometry of the probe and to the propagation of the signal along the lines that compose the B-scan, it is necessary to estimate the probe's shape in the first phase. The probe's shape is related to the probe geometry (linear, curvilinear) and corresponds to the image mask in the B-scans (see figure 5.6-a). Then, in a second phase, a signal analysis is performed along the lines that compose the B-scan. An acoustic shadow is detected along a line when two criteria are met:

1. A rupture along a line exists and
2. The signal distribution after the rupture is statistically compliant with an estimated noise model.

The detection method is thus decomposed into the following steps:

#### 5.3.2.1 B-scan geometry extraction

Given a sequence of  $2D$  ultrasound images (see a typical image in figure 5.6-(a)), it is necessary to separate the image and the background. In many cases, the geometry (e.g., fan vs linear) will be known *a priori*, it will be possible to use a precomputed mask and this step of the procedure can be skipped. However, when this is not the case, estimating the mask amount to computing a  $2D$  mask given the  $2D + t$  sequence. To do so, maps of longitudinal mean and variance are computed, and multiplied pixelwise to compute a feature map. For a given point, the longitudinal mean (respectively variance) is defined as the mean (respectively variance) of a  $2D$  pixel location over time. Background pixels are dark and have low (or zero) variance. Points in the image foreground have the highest values of the feature map (compared to the background). Then, points with the highest values of the feature map are retained (see figure 5.6-(b)). To remove false detections exist, a morphological closing and opening are performed to clean the input mask (see figure 5.6-(c)). To estimate the probe geometry, a trapezoid model is fitted to the input mask. The trapezoid

model is the simplest model capable of capturing the geometry of a linear or curvilinear probe. The 5 parameters of the model are estimated by optimizing the total performance measure.

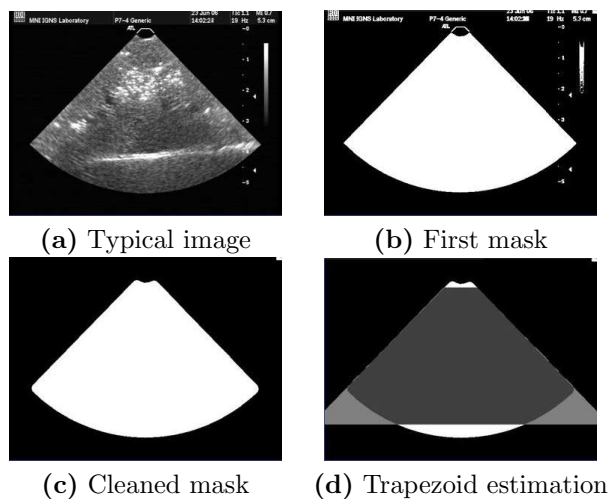


Figure 5.6: Illustration of the automatic mask extraction. (a) shows a typical image of the acquired sequence. (b) shows the first mask obtained after selecting the highest values of the longitudinal statistics. (c) shows the mask after morphological operators were applied to remove patient information. (d) shows the final trapezoid model estimation.

### 5.3.2.2 Line rupture detection

Once the probe's geometry is estimated, it is possible to know whether the direction of scanning is top-down or bottom-up when a curvilinear probe is used. For a linear probe, the user must specify the direction of scanning (it is generally top-down except if the video grabber flipped the image). Afterwards, it is necessary to sample line profiles corresponding to the transducer lines. For each B-scan, an arbitrary number of lines can be drawn and for each line,  $k$  samples are computed by trilinear interpolation in the corresponding B-scan. As mentioned previously, the shadow is defined as a signal rupture along the line, followed by a low signal afterwards. Therefore, signal ruptures are detected first. To do so, the line signal is smoothed with a low-pass filter. Then, a local symmetric entropy criterion is computed. For each point  $p$  of the line signal  $\mathcal{S}$ , a sliding window of size  $n$  is used to compute the rupture criterion  $\mathcal{R}$ :

$$\mathcal{R} = \sum_{i=1}^{i=n} \left( \mathcal{S}(p-i) \log \frac{\mathcal{S}(p-i)}{\mathcal{S}(p+i)} + \mathcal{S}(p+i) \log \frac{\mathcal{S}(p+i)}{\mathcal{S}(p-i)} \right)$$

The first term is the relative entropy of the "past" (the signal before the rupture) knowing the "future" (the signal after the rupture) which can also be viewed as the Kullback-Leibler divergence of the past distribution given a reference signal (the future). In order to symmetrize the criterion, the second term is added and expresses the relative entropy of the future knowing the

past. The loci where  $\mathcal{R}$  is maximal indicate a signal rupture. The rupture criterion  $R$  is quite general since it relies on the statistical dependency between the future and the past samples in a sliding window. Rupture positions are determined as zero-crossings of the gradient of  $\mathcal{R}$ .

### 5.3.2.3 Shadow detection

It is generally assumed that acoustic shadows are areas where the signal is relatively low. In this paper, we assume that acoustic shadows are areas where the noise is low. Since noise is modulated by signal intensity in ultrasound images, this is not a strong assumption. When a rupture is detected and tested as a candidate for a shadow, let us denote  $\mathbb{E}(u_f)$  (respectively  $\mathbb{V}(u_f)$ ) the mean (respectively the variance) of the signal after the rupture. The shadow detection test states that the intensity noise after the rupture is low and not compliant with the noise modeling of equation 5.1. Therefore, the test reads as:

$$\mathbb{V}(u_f) < \mathbb{E}(u_f) \cdot \sigma^2. \quad (5.10)$$

Thus it is necessary to estimate the parameter  $\sigma$ . To do so, we follow the approach described in [76]. On local square patches that intersect the B-scan mask, the local mean  $\mu$  and variance  $\vartheta$  are computed. The parameter  $\sigma^2$  can be interpreted as the linear regression parameter of the variance versus the mean:  $\vartheta = \sigma^2 \cdot \mu$ .

This computation relies on the hypothesis that the patch contains only one tissue type. This cannot be ensured in practice as illustrated in figure 5.7-(a) where two regions  $R_1$  and  $R_2$  intersect the patch. Therefore, a robust Leclerc M-estimators (with parameter  $\sigma = 20$ ) is used to compute a robust mean and variance. Let us note  $x_i$  the samples that compose the patch, then the robust mean is computed as  $\mu = \frac{\sum_i \lambda_i x_i}{\sum_i \lambda_i}$ . The robust estimator iterates between the computation of the weights  $\lambda$  and the weighted mean  $\mu$  until convergence. After convergence, the weights  $\lambda$  are used to compute the robust variance as  $V_r(x) = \frac{\sum_i \lambda_i^2 (x_i - \bar{x})^2}{\sum_i \lambda_i}$ . Figure 5.7-(b) shows a plot of variance versus mean of all image patches using a classical computation, while figure 5.7-(c) show the same plot with a robust computation of mean and variance. These figures show that the robust computation leads to a better constrained linear regression.

The remaining issue is the size of the square patch used to compute the regression parameter  $\sigma$ . One may expect that using small patches will bias the computation of mean variance, while using large patches will lead to inconsistent results, since a patch will contain several tissue classes, as illustrated in figure 5.7-(a). Figure 5.8 shows the results of the regression parameter when the patch size varies, with a classic computation of statistics 5.8-(a) and a robust computation of statistics 5.8-(b). This shows that the classical computation leads to a biased estimation of  $\sigma$ . When the patch size increases, the patch is composed of different tissue classes and the observed variance is the sum of the noise variance and the inter-tissue variance. On the opposite, the use of robust statistics leads to a consistent and reliable estimation of  $\sigma$  over a wide range of patch sizes.

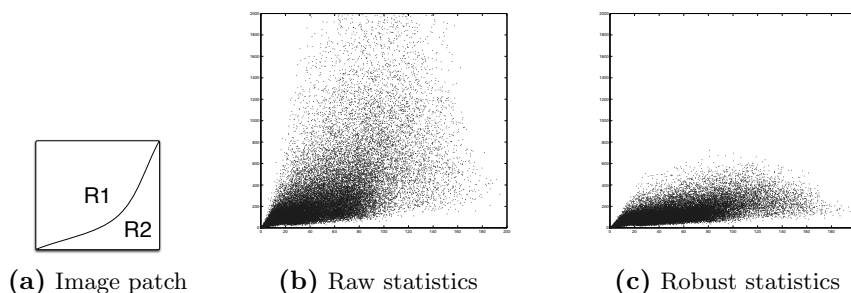


Figure 5.7: Estimation of parameter  $\sigma$  of the noise model 5.1. On square patches, local statistics are computed to determine the parameter  $\sigma$ . Each dot represents the local statistic (variance on vertical axis versus mean on horizontal axis) of a single patch computed from a real intraoperative image. Since a square patch may not contain only one tissue, as illustrated on the left, robust statistics are used to compute the mean and variance. As a matter of fact, when a patch is composed of two tissue types, the variance increases and this is visible in figure (b). On the contrary, the use of robust statistics (c) enables a more accurate regression and estimation of  $\sigma$  compared to the regression using standard statistics (b).

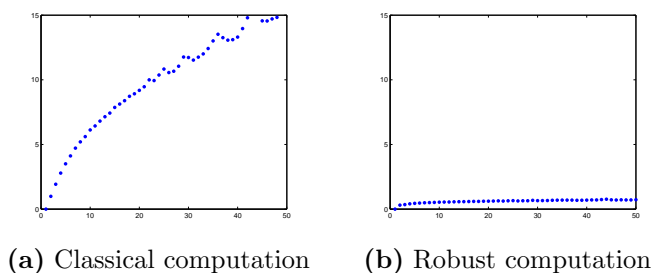


Figure 5.8: Influence of patch size on parameter  $\sigma^2$  computed with classical statistics (a,) and robust statistics (b). The use of robust statistics leads to a consistent and reliable estimation of the regression parameter. When the size patch increases, a patch contains several tissue classes and the observed variance is the sum of the noise variance and the inter-tissue intensity variance. Therefore, the regression parameter increases.

#### 5.3.2.4 Regularization

Since acoustic shadows are due to an anatomical structure that reflects the wave energy (which more precisely depends on the angle between the beam and the interface), the detection of acoustic shadows should vary smoothly between two consecutive lines. A simple regularization scheme is therefore adopted: for each line, the detection index is defined as the position of the detected shadow along the line. A 2D median filtering of the detection indexes was first performed on a local neighborhood of adjacent lines to regularize the solution.

When the acquisition is continuous, the variations of acoustic shadow profiles should also vary smoothly between consecutive slices, since the frame rate of the imaging system is usually above  $10Hz$  and the movement of the probe is relatively slow. Thus, a longitudinal regularization is performed by taking into account adjacent lines from the 2 neighboring B-scans, achieving an anisotropic  $2D + t$  median filtering.

### 5.3.3 Results

#### 5.3.3.1 Comparison with manually delineated ROI

Since the automatic method detects both the B-scan geometry and the shadows as shown in figure 2.2-c, the image ROI (i.e., the B-scan mask without the detected shadows) was compared to a manual delineation of this area. Three real intraoperative sequences were chosen for this experiment, with depth varying from superficial acquisition 5.9-(a) to deep acquisition 5.9-(c). The extent of the acoustic shadows and signal attenuation increases with the acquisition depth.

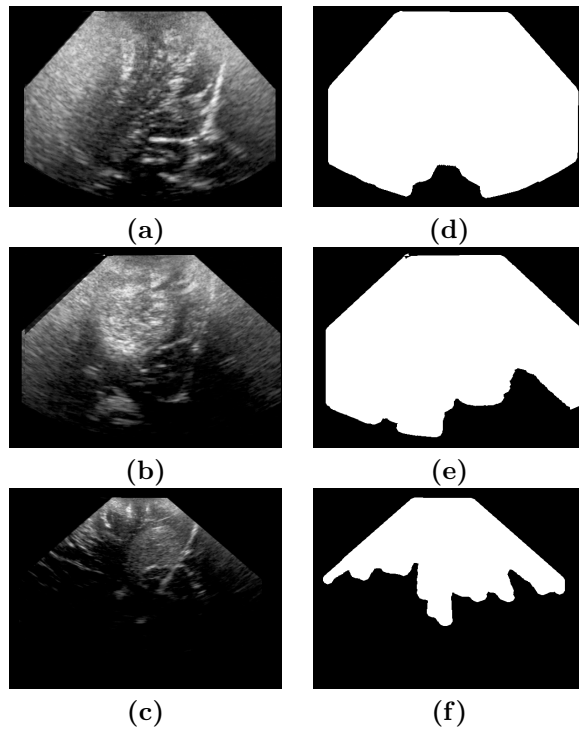


Figure 5.9: Left: Real intraoperative data used for the comparison with manual delineation. Data was chosen so as to represent three different depth acquisition: superficial, medium and deep. Right: the corresponding ROI detected with the automatic method.

Four experts manually delineated the areas using the ITKsnap software [180]. The corresponding segmentations are presented in Fig. 5.10. Visually, the experts segmentations exhibit very large differences. This fact supports

the use of an objective automatic process to deliniate these areas. As an evaluation criterion, the Dice coefficient, as well as the specificity and sensitivity were compared between the automatic method and the manual raters. Results are given in Tables 5.2, 5.3 and 5.4. Results show that the automatic method is very consistent with respect to the raters segmentations.

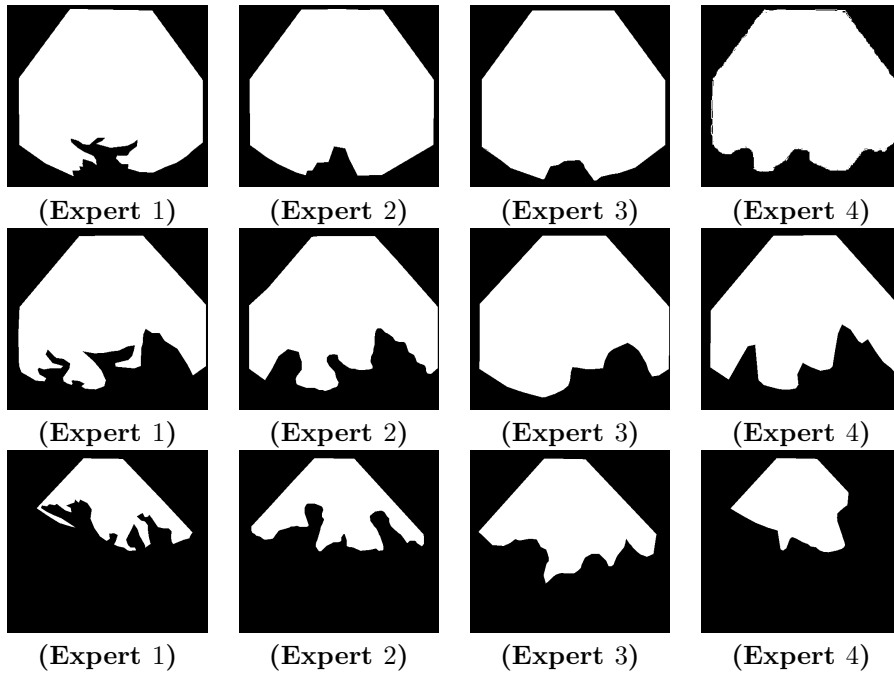


Figure 5.10: Expert segmentation of the image ROI for the dataset 5.9-(a) (top row), 5.9-(b) (middle row) and 5.9-(c) (bottom row). Despite reasonably high kappa values, the manual segmentations are visually significantly different, what advocates for an automatic process.

	Rater 2	Rater 3	Rater 4	Automatic method
Rater 1	0.980	0.969	0.967	0.977
Rater 2		0.981	0.974	0.986
Rater 3			0.964	0.978
Rater 4				0.975

Table 5.2: Comparison between the various segmentations (manual raters, and automatic method) for the superficial dataset (5.9-(a)). For each comparison, the criterion is the Dice coefficient. The automatic method leads to results as consistent as the manual raters with an excellent detection rate.

	Rater 2	Rater 3	Rater 4	Automatic method
Rater 1	0.964	0.936	0.958	0.933
Rater 2		0.943	0.977	0.939
Rater 3			0.945	0.976
Rater 4				0.942

Table 5.3: Comparison between the various segmentations for the medium depth dataset (5.9-(b)) as in Table 5.2. The automatic method leads to results as consistent as the manual raters with an excellent detection rate.

	Rater 2	Rater 3	Rater 4	Automatic method
Rater 1	0.855	0.781	0.819	0.817
Rater 2		0.822	0.848	0.897
Rater 3			0.752	0.879
Rater 4				0.840

Table 5.4: Comparison between the various segmentations for the large depth dataset (5.9-(c)) as in Table 5.2. The Dice coefficient decreases compared to superficial acquisitions, since the relative size of the ROI compared to the image size decreases.

#### 5.4 DISCUSSION

In this chapter, a dedicated ultrasound noise model was used to detect and/or correct image artifact like noise or acoustic shadows. The noise model is simple and can be manipulated easily. Yet it has revealed to be efficient since it has demonstrated good capability to capture the image artifacts. This artifacts detection/reduction clearly aims at improving image processing processing and not visual image interpretation.

The acoustic shadow detection method may be incorporated in a CT to ultrasound registration technique. As a matter of fact, bone surfaces produce a strong energy reflection, leading to an acoustic shadow. The detection of acoustic shadows in ultrasound images, and the shadow interface, is a feature that may be registered to a bone segmentation in CT images. This could be applied to an automatic image-to-patient registration for spine surgery [13].

Validation is still an issue, as well as the comparison of methods (detection of acoustic shadows and noise reduction). In both cases, generally no ground truth is available. We have tried to cope with this limitation and to propose evaluation metrics. The dissemination of such data and metrics would be valuable since different methods would then be evaluated on the same basis.

## 6.1 INTRODUCTION

In the context of Image-Guided NeuroSurgery (IGNS), the feasibility to quantify or compensate for the brainshift using ultrasound imaging has been shown in several studies [8, 25, 35, 59, 70, 91, 106, 110, 131]. Deformations are estimated using rigid and non-rigid registration techniques.

The rigid registration between the preoperative MR image and the intraoperative field is performed using the neuronavigation system before the beginning of the procedure. This rigid image to physical space registration is based on fiducials on the patient's head or on surface matching between the scalp surface extracted from the MR image and a cloud of points acquired on the patient's head with a position localizer. In phantom [35] or animal studies [110], the accuracy of this rigid registration between intraoperative B-scans and operative field has been quantified between  $1.5mm$  and  $3mm$ . In many studies performed with different image modalities [50, 54, 67, 69, 75, 106, 121, 125, 146, 153], the brainshift has been measured between  $5mm$  and  $25mm$ . The necessity to improve the accuracy of the rigid registration between the intraoperative B-scans and the operative field is thus required to estimate or compensate for brainshift. In case of ultrasound utilization, this improvement is generally based on an image-based rigid registration between intraoperative US and preoperative MR image.

The formation of ultrasound images is based on the difference of acoustic impedance of tissues while MR images are based on paramagnetic properties of the tissues. Thus, the information and artifacts present in US and MR images have very different nature. The registration of these two modalities is still a difficult task. Registration approaches based on classical similarity measures such as the Sum Square Difference (SSD), Mutual Information (MI) or Correlation Ratio (CR) are known to fail [147]. Previous works have studied three options to register US and MR images: (a) the matching of homologous features segmented from both images [35, 59, 91, 139, 145], (b) the preprocessing of the images to make US images and MR images more similar in order to use classical similarity measures [8, 105, 132] and (c) the intensity-based registration based on a specific similarity measure matching the US and MR image intensities [147].

Landmark-based registration represents the majority of the approaches in the context of US to MR registration [35, 59, 91, 139, 145]. The motivation is bound to the difficulty of finding a function matching US image intensities with MR image intensities. These methods are based on the matching of (a) points manually defined [59], (b) lines representing the vascular system [35, 139, 145], or (c) cortical surface [91]. The main disadvantage of landmark-based registration

is finding the landmarks and sensitivity to segmentation.

Intensity-based approaches using histogram-based similarity measures tend to overcome the problem by preprocessing the images in order to register similar images. In [8], the segmentation and the gradient magnitude of the MR image are used to simulate a pseudo-US, then the Correlation Coefficient (CC) is used as the similarity measure. In [105], the Normalized Mutual Information (NMI) is used to register the gradient magnitude images of both modalities. Intensity-based approaches use the MR image gradient in the registration procedure because US images are considered as similar to gradient images.

To the best of our knowledge, Roche *et al.* [147] was the only attempt to incorporate the transformation of MR image into pseudo-US in the similarity measure by introducing the the Bivariate Correlation Ratio (BCR). The registration procedure is split into two steps: (a) the estimation of a polynomial function matching the intensity and the gradient of the MRI with the US image and (b) the estimation of the transformation minimizing the BCR.

In this chapter, we propose a new objective function based on a probabilistic map of hyperechogenic structures composed of the mean curvature ( $Ml_{vv}$ ) of the preoperative MR image and the segmentation of the pathological tissues. The  $Ml_{vv}$  operator was introduced to detect the sulci and the cerebral falx [99] which are the hyperechogenic structures of the brain in ultrasound images. Being robust and specific to distinguish the positive and negative curvature of MR isophots, the  $Ml_{vv}$  operator is more relevant than the gradient magnitude operator to detect the sulci in MR brain image.

## 6.2 METHOD

### 6.2.1 Matching hyperechogenic structures

Contrary to histogram-based approaches that match all the information in both images, the proposed approach consists in matching only hyperechogenic structures [37]. To do so, the “hyperechogenic” structures present in MR image (i.e. the structures visible in MR image expected to be hyperechogenic in intraoperative US) are detected. In brain imaging, these structures are the liquid interfaces as the cerebral falx and the sulci, and the lesion when the corresponding tissue is hyperechogenic such as cavernoma or glioma.

The registration process is based on the estimation of the transformation  $\hat{T}$  maximizing the joint probability for a voxel  $X = (x, y, z)$  to be included in hyperechogenic structures in both modalities:

$$\hat{T} = \arg \max_T \int_{\Omega} p(X \in \Phi_{US}, T(X) \in \Phi_{MR}) dX \quad (6.1)$$

where  $p(X \in \Phi_{US})$  is the probability for  $X$  to be included in an hyperechogenic structure from the US image and  $p(X \in \Phi_{MR})$  is the probability for  $X$  to be included in an hyperechogenic structure (in the sense of the ultrasound image) from the MR image. Assuming that the probabilities are independent, we can write:

$$\hat{T} = \arg \max_T \int_{\Omega} p(X \in \Phi_{US}) \cdot p(T(X) \in \Phi_{MR}) dX \quad (6.2)$$

### 6.2.2 Construction of the probability maps

In order to construct the probability maps, we define a function  $f$  matching the intensity of both the US image and the MR image with the probability for

$X$  to be included in hyperechogenic structures:

$$p(X \in \Phi) = f(u(X)) \quad (6.3)$$

where  $u : \Omega \mapsto \mathbb{R}$  is an image defined on  $\Omega$ .

For the intraoperative US image  $U$ , the evaluation of  $f$  is done during surgery and is only a normalizing function:

$$p(X \in \Phi_{US}) = U(X)/2^n \quad (6.4)$$

where  $n$  is the number of bits of the unsigned encoded image.

For the preoperative MR image  $V$ , the evaluation of  $f$  is done prior to surgery and is based on both the detection of the liquid interfaces with the  $Mlvv$  operator and the segmentation of the pathological tissues:

$$p(X \in \Phi_{MR}) = \frac{Mlvv(V(X))}{2^n} \mathbb{I}_{M1}(X) + \Psi(X) \mathbb{I}_{M2}(X) \quad (6.5)$$

where  $\mathbb{I}_M$  is the indicator function for the set  $M$ :

- $M1 = \{X \in \Omega, \text{ such that } Mlvv(V(X)) \geq 0\}$
- $M2 = \{X \in \Omega, \text{ such that } X \text{ belongs to the lesional tissue}\}$

The  $Mlvv$  operator is defined in 3D as :

$$Mlvv(V(x, y, z)) = -\frac{1}{2\|\vec{w}\|^2} \left[ \begin{aligned} & \left[ \frac{\partial V(X)}{\partial x} \right]^2 \left( \frac{\partial^2 V(X)}{\partial y^2} + \frac{\partial^2 V(X)}{\partial z^2} \right) - 2 \frac{\partial V(X)}{\partial y} \frac{\partial V(X)}{\partial z} \frac{\partial^2 V(X)}{\partial y \partial z} + \\ & \frac{\partial V(X)}{\partial y} \left[ \frac{\partial^2 V(X)}{\partial x^2} + \frac{\partial^2 V(X)}{\partial z^2} \right] - 2 \frac{\partial V(X)}{\partial x} \frac{\partial V(X)}{\partial z} \frac{\partial^2 V(X)}{\partial x \partial z} + \\ & \frac{\partial V(X)}{\partial z} \left[ \frac{\partial^2 V(X)}{\partial x^2} + \frac{\partial^2 V(X)}{\partial y^2} \right] - 2 \frac{\partial V(X)}{\partial x} \frac{\partial V(X)}{\partial y} \frac{\partial^2 V(X)}{\partial x \partial y} \end{aligned} \right] \quad (6.6)$$

where  $\|\vec{w}\|^2 = \frac{\partial V(X)}{\partial x}^2 + \frac{\partial V(X)}{\partial y}^2 + \frac{\partial V(X)}{\partial z}^2$ .  $\Psi(X)$  is the probability given to  $X$  in the segmentation of pathological tissue  $M_2$ .  $\Psi()$  is used to incorporate *a priori* on pathology. For pathological tissue such as cavernoma or low-grade glioma,  $\Psi(X)$  is high since these tissues are hyperechogenic.

The following operations are performed before surgery: the  $Mlvv$  is computed from T1-w MR images on the segmented brain by masking the pathological tissue. Then, only the positive values (i.e. the sulci and the falx) are kept. Finally, the  $Mlvv$  map is fused with the segmentation  $M_2$ . In our experiments, the segmentation of pathology was manually performed by the neuroanatomist before the surgical procedure. Moreover, the simplest case for hyperechogenic pathologies was chosen:  $\Psi$  is constant (i.e.,  $\forall X \in M_2, \Psi(X) = 1$ ). This segmentation could be automated and the different parts of pathologies (lesion, coagulated blood, cyst, necrotic tissue, *etc*) could be defined with different values corresponding to their hyperechogenic level. A scheme of the overall workflow is given in figure 6.1.

### 6.2.3 Non-rigid parametrization

The proposed similarity can also be embedded with non rigid transformations. Since the registration procedure is based on hyperechogenic features matching, a global parametrization is chosen. Indeed, the probability maps can be considered as fuzzy segmentations of hyperechogenic structures. As a global

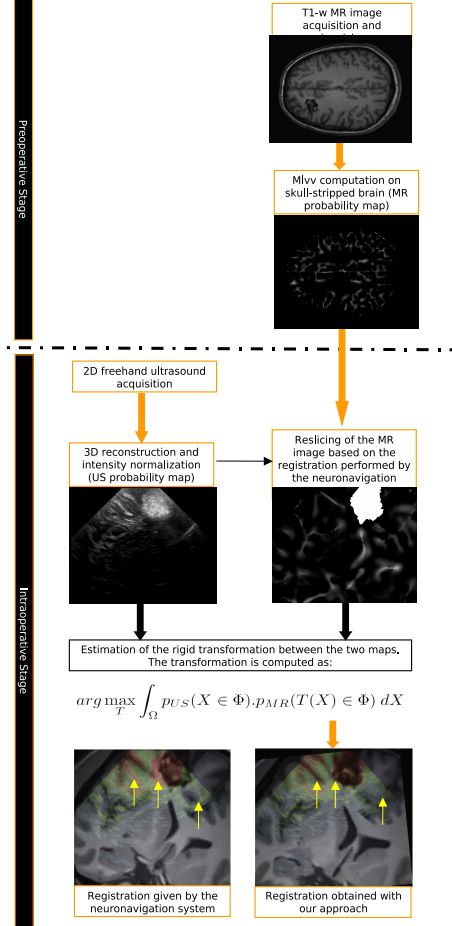


Figure 6.1: Illustration of the performed workflow to achieve the registration. The skull stripping, the denoising, the  $Mlvv$  computation and the segmentation of lesion are performed before the neurosurgical procedure. Then, the 3D reconstruction of intraoperative volume, the reslicing of the MR map and the estimation of the transformation is estimated during the neurosurgical procedure.

non-rigid parametrization, a set of cosines basis functions was chosen. This kind of parametrization has been already presented in the literature as in [10] for instance.

The set of cosine basis functions is defined by their pulsation  $\omega^f$  (i.e. frequency). Estimating the transformations therefore amounts to estimating the magnitude parameters ( $\{\alpha_i^f, \beta_i^f, \gamma_i^f; i \in [1, 2, 3]\}$ ) and phases parameters ( $\{\phi_i^f, \psi_i^f, \rho_i^f; i \in [1, 2, 3]\}$ ) for each cosine basis function. The set of pulsations

$\mathcal{W}$  of the basis functions is defined as  $\mathcal{W} : \{\omega^0, \dots, \omega^F\}$  and is fixed *a priori*. Finally, the parametrization can be written as:

$$U^F(X) = \sum_{f=0}^F \begin{pmatrix} \alpha_1^f \cos(\omega^f x + \phi_1^f) + \beta_1^f \cos(\omega^f y + \psi_1^f) + \gamma_1^f \cos(\omega^f z + \rho_1^f) \\ \alpha_2^f \cos(\omega^f x + \phi_2^f) + \beta_2^f \cos(\omega^f y + \psi_2^f) + \gamma_2^f \cos(\omega^f y + \rho_2^f) \\ \alpha_3^f \cos(\omega^f x + \phi_3^f) + \beta_3^f \cos(\omega^f y + \psi_3^f) + \gamma_3^f \cos(\omega^f z + \rho_3^f) \end{pmatrix} \quad (6.7)$$

where  $X = (x, y, z)$  are the coordinates of the voxel in the reference image (i.e. the probability map extract from MR image) and  $U^F(X)$  are the coordinates of the homologous points in the floating image (i.e. the normalized US image). By extension of the equation 6.2 to the non rigid transformations, the registration procedure can be written as:

$$\arg \max_{\mathbf{P}} \int_{\Omega} p(X \in \Phi_{MR}) \cdot p(U^F(X) \in \Phi_{US}) dX \quad (6.8)$$

where  $\mathbf{P} : \{\alpha_i^f, \beta_i^f, \gamma_i^f, \phi_i^f, \psi_i^f, \rho_i^f; i \in [1, 2, 3]; f \in [0, \dots, F]\}$  represents the set of basis function parameters.

#### 6.2.4 Optimization

These parameters are iteratively estimated from the lowest frequency to the highest frequency. First, the Simplex optimizer is used to estimate the 18 parameters for  $\omega^0$ . Then, these parameters are fixed and the 18 parameters for  $\omega^1$  are then estimated. This procedure is repeated until  $f = F$ . In the experiments, the same set  $\mathcal{W}$  was used for all the patients. This set is composed of 10 pulsations (i.e.  $F = 10$ ) regularly distributed between  $[\omega^0, \omega^{10}]$ .

### 6.3 FIRST RESULTS

In this section, results on patient data set is presented. The proposed approach was validated on hyperechogenic pathologies (2 patients with cavernoma and 1 patient with low-grade glioma). For all patients, as previously described, the same simple model  $\Psi(X) = 1$  was chosen before neurosurgery. The accuracy of the registration was visually checked by the neurosurgeon over the volumes. According to the neurosurgeon, the overlay of the modalities was improved after rigid and non rigid registration procedures in all cases.

Patient	Rigid registration Estimated error	Non rigid registration Estimated deformation
1	5.72 mm	2.71 ± 1.03 mm
2	4.94 mm	3.74 ± 1.19 mm
3	6.50 mm	1.81 ± 1.02 mm

Table 6.1: Result of the overall workflow for 3 patients. Left: Patient identification. Middle: estimation of the error provided by the neuronavigation system (i.e. rigid registration). Right: magnitude of the estimated non rigid deformation (i.e. non rigid registration).

Table 6.3 shows the quantitative results obtained for three patients after rigid and non rigid registrations. These estimations were computed as the mean

Euclidean distance over all the voxels before and after registration. The estimated errors produced by the neuronavigation system were significantly higher than the errors reported in the literature ( $< 3$  mm [35,110]). This difference may be due to the clinical context of our study where the constraints differ from phantom studies. The magnitude of the estimated non rigid deformations was close to the deformation reported by others studies [106,121,125].

Figures 6.2, 6.3 6.4 show the result of the registrations for three patients. In all cases, before opening the dura, the rigid registrations greatly improved the registration of the US and MR images performed by the neuronavigation system (see top of Fig. 6.2, 6.3 and 6.4). After opening the dura different cases appeared. For patient 1, the cavernoma did move to the craniotomy (see bottom of Fig. 6.2). Visually, the non rigid registration correctly compensated this movement. It is interesting to note that the real deformation observed for this patient is close (visually and in term of magnitude) to the synthetic deformation applied to this data set during the previous experiment. For patient 2, a large expansion of the glioma did occur creating out-bulging shift (see bottom of Fig. 6.3). The expansion may be due to the great size of the glioma for which the growing generated constraints on surrounding tissues. In this extreme case, the non rigid registration did not entirely recover the large local deformation on the top of glioma. Nevertheless, the non rigid procedure did compensate the movement on cerebral falx and bottom of glioma. For patient 3, the sulci did shift to the central part of the cortex (see bottom of Fig. 6.4). This deformation seems to be correctly compensated, especially on sulci, cavernoma and cerebral falx.

#### 6.4 DISCUSSION

In this chapter, a registration framework between intraoperative brain ultrasound and preoperative MR images was presented. This framework builds on the matching of hyperechogenic structures. This feature was chosen since it is straightforwardly computed intraoperatively, due to its local nature it is less sensitive to imaging artifact. This similarity measure can then be used for a rigid or non-rigid parametrization. First results show the efficacy of this similarity to register intraoperative ultrasound to preoperative MRI. This type of registration technique may be easily implemented using GPU in order to lead to real-time registration.

At the moment, the similarity balances between two hyperechogenic structures, the liquid interfaces (falx, sulci) and the lesion. A parameter function  $\Psi$  is involved. At the moment, the simplest choice was made for  $\Psi: \forall X, \Psi(X) = 1$ . Future work should concentrate on relaxing this choice, either using a more precise segmentation of the lesion (determining the tumoral tissue from the cystic part that might be hypoechogenic for instance), or by "learning" the optimized function for a set of clinical cases.

Further work should investigate the non-rigid parametrization that is very constrained at the moment. The parametrization was constraint so as to speed up the registration, however this is not satisfying. The parameters (set of frequencies) should be either estimated or learned over a database of real cases. Probably better, the parametrization model itself should be learned and this will be discussed in the conclusion.

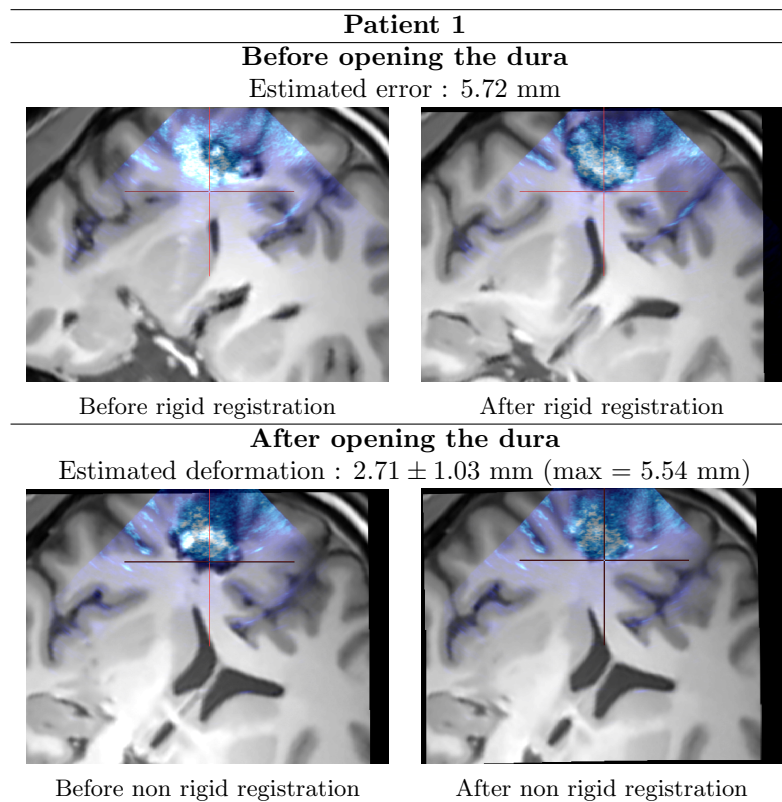


Figure 6.2: **Top.** Left: overlay of the US image acquired before opening the dura with the re-sliced MR image after rigid registration based on the matrix provided by the neuronavigation system. Right: overlay of these images before rigid registration. **Bottom.** Left: overlay of the US image acquired after opening the dura and the rigid registration of the MR image. A displacement of the cavernoma to the craniotomy has occurred. Right: overlay of these images after non rigid registration.

Although first results are promising, extensive experiments and evaluation of the method are needed. Validation is also problematic and should be addressed. As for many validation contexts, no ground truth is available and simulated deformation are too limited. This issue will also be discussed in the conclusion of the manuscript.

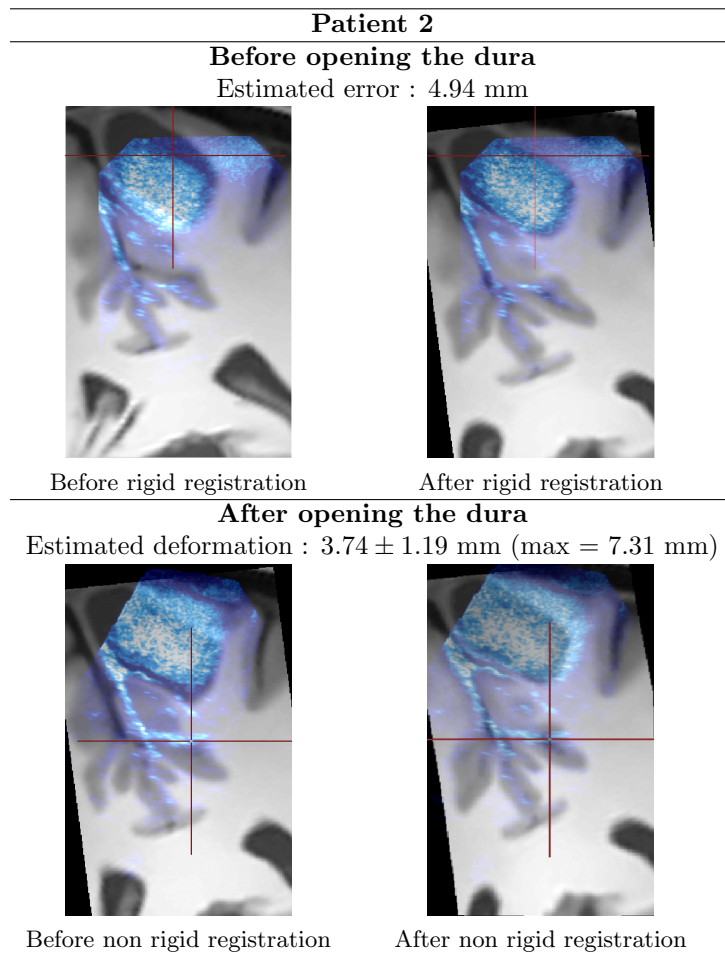


Figure 6.3: **Top.** Left: overlay of the US image acquired before opening the dura with the re-sliced MR image after rigid registration based on the matrix provided by the neuronavigation system. Right: overlay of these images before rigid registration. **Bottom.** Left: overlay of the US image acquired after opening the dura and the rigid registration of the MR image. A large expansion of the glioma has occurred. Right: overlay of these images after non rigid registration.

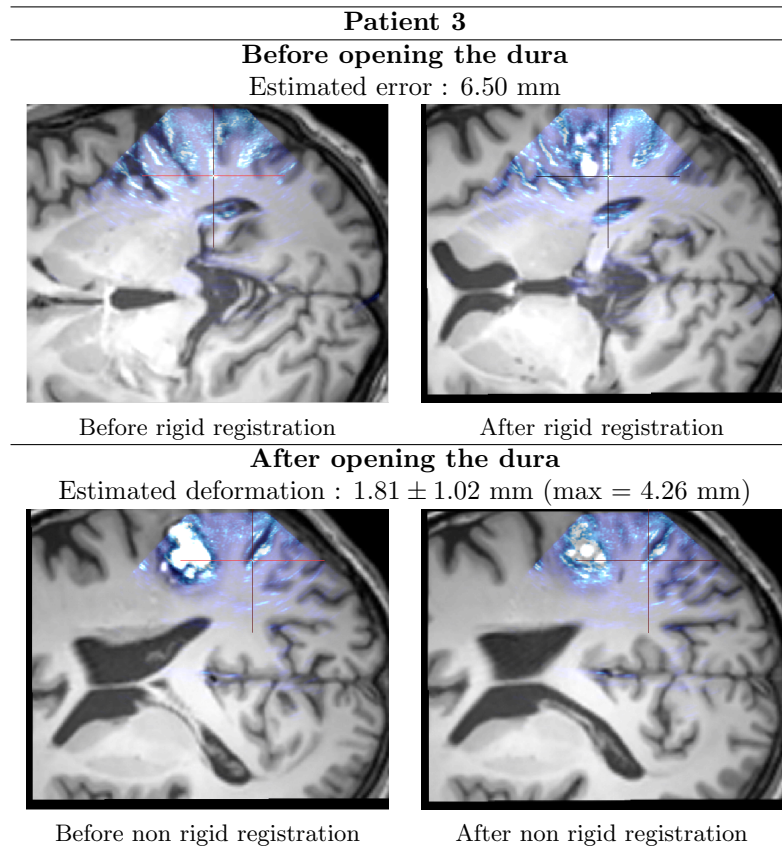


Figure 6.4: **Top.** Left: overlay of the US image acquired before opening the dura and the re-sliced MR image after rigid registration based on the matrix provided by the neuronavigation system. Right: overlay of these images before rigid registration. **Bottom.** Left: overlay of the US image acquired after opening the dura and the rigid registration of the MR image. A movement of the sulci near the cavernoma has occurred. Right: overlay of these images after non rigid registration.



Il semble que nous naissons à mi  
chemin du commencement et de  
la fin du monde. Nous  
grandissons en révolte ouverte  
presque aussi furieusement contre  
ce qui nous entraîne que contre  
ce qui nous retient.

---

René Char

In this document, a few contributions to image processing methods for intraoperative ultrasound in neurosurgery have been proposed. From the acquisition to the analysis of the data, these steps require successively calibration, reconstruction, artifact reduction and registration. Some conclusions have been drawn along this document, and further work awaits us:

### 7.1 CAPTURING INTRAOPERATIVE DEFORMATIONS

- To meet the requirement of surgery, a real-time workflow is needed. Real-time, in this context, means less than  $1min$  between data acquisition and displaying the reformatted preoperative MRI. At the moment, around  $4min$  are needed. Efforts to reach this goal are technological rather than methodological. In particular, GPU computation facilities may be successfully used to this aim.
- The reconstruction step may eventually be skipped by developing registration without reconstruction techniques. The advantage would be a decreased computation time. The rigid implementation is straightforward, but the non-rigid extension is less trivial since the regularization of the deformation field should then be adapted to the local spatial resolution of the data.
- Visual servoing and Bayesian techniques may be useful in such project, in order to capture a possible relationship between the ultrasound acquisition field of view and an expected registration error. If such relationship can be established, then it would be possible to guide the surgeon's acquisition and/or to reject sequences that will lead to an unacceptable registration error.
- In the registration chapter, the choice of a ultrasound to MRI registration has been made. It would be valuable to compare the obtained deformations to an ultrasound to ultrasound registration [144]. The advantage

would be a monomodal registration problem and thus easier, the drawback being that field of views between ultrasound images to be registered should overlap so as to capture relevant deformations.

- The temporal resolution of 3D ultrasound data is rather low because the surgeon needs to stop surgery for data acquisition. Therefore, only a few acquisition are possible (generally, one before opening the dura, one after opening the dura, one during surgery and one at the expected end of resection). This leads to a difficult problem of estimating deformations of possibly large magnitude. A solution would be to think the problem in terms of continuous deformation flow. Additional observations, like 2D images of the microscope, could be added as a constraint to this estimation problem.
- Finally, the matter dissipation effect caused by the resection process needs to be incorporated in the registration problem. It makes no sense to register tissue that has been removed, nor to regularize the deformation field at points where it should not be defined. A cooperative framework, including resection segmentation and registration, could be developed to this aim.

## 7.2 INTRAOPERATIVE TISSUE CHARACTERIZATION

In image-guided neurosurgery, the compensation of soft-tissue deformation is only a piece of the puzzle. The final objective is to answer the question if there is tumoral tissue left at the expected end of resection. This is particularly relevant for low-grade glioma where the expected lifespan is correlated to the quality of resection. Therefore, although brainshift compensation is the first step, intraoperative tissue classification is needed.

- The classification of tumoral tissue using B-mode ultrasound seems challenging since the quality of images at the end of surgery is rather low, due to imaging conditions (the cavity, although filled with liquid, contains bubbles). The hyperechogenic rim is visible at the end of resection cavity, probably due to inflammation, and assessing the thickness of the rim may help. As a matter of fact, one may hypothesize that an heterogeneous rim might indicate the presence of residual lesion, while an homogeneous rim would indicate total resection. However, additional developments are needed:
  - At the expected end of resection, relevant information is at the fondus of the intraoperative cavity, but the imaging thickness should be limited and the spatial resolution increased. To this aim, high-frequency ultrasound (above 20Mhz) would then be useful.
  - The use of contrast agent, for instance USPIO (ultra-small particles of iron oxide), would increase the contrast of ultrasound images. In particular, it has been shown recently [45, 128] that USPIO induces a frequency-shift. The advantage is that USPIO is capable of traversing the BBB (Brain Blood Barrier) and when recaptured by macrophages, will be fixed in the tumor. As a consequence, the use of USPIO would increase the capability of ultrasound to delineate tumor borders.

- In addition to contrast agent, elastography would probably provide stiffness information that would be helpful. It is known, for instance for low-grade glioma, that stiffness differs from normal brain tissue. That information could potentially be more specific to delineate brain tumors.
- To assess the nature of the tissue, optical imagery like fluorescence or confocal microscopy would definitely be of great interest. However, there are still some technical limitations that may disappear in the next future.
- To fully exploit all the information available, multimodal and multiscale classification techniques will be needed, since data are of extremely different spatial and temporal resolution.

#### 7.3 CLINICAL CONTEXT: LEARNING AND VALIDATION

Finally, further work should focus on the clinical context:

- It would be valuable to introduce clinical a priori in the proposed methods. For instance, external parameters like patient's position, craniotomy size, direction of gravity, tumor volume and position, etc. could be used fruitfully as constraints. In addition, learning aspects should be introduced, for instance in the registration process (learning a relevant parametrized deformation model).
- In the future, clinical usefulness and validation should be addressed. This topic is difficult, from an ethical point of view, and from a methodological point of view. It will be reasonable to start with simple questions like "is the resection quality better when using image-guided techniques?".



---

## Bibliography

---

- [1] K.Z. Abd-Elmoniem, A.B.M. Youssef, and Y.M. Kadah. Real-time speckle reduction and coherence enhancement in ultrasound imaging via nonlinear anisotropic diffusion. *IEEE Transactions on Biomedical Engineering*, 49(9):997–1014, 2002.
- [2] A. Achim, A. Bezerianos, and P. Tsakalides. Novel bayesian multiscale method for speckle removal in medical ultrasound images. *IEEE Transactions on Medical Imaging*, 20:772–783, August 2001.
- [3] O. Acosta, H. Frimmel, A. Fenster, and S. Ourselin. Filtering and restoration of structures in 3d ultrasound images. In *Biomedical Imaging: From Nano to Macro, 2007. ISBI 2007. 4th IEEE International Symposium on*, pages 888–891, 2007.
- [4] B. Aiazzi, L. Alparone, and S. Baronti. Multiresolution local-statistics speckle filtering based on a ratio laplacian pyramid. *IEEE Transactions on Geoscience and Remote Sensing*, 36(5):1466–1476, 1998.
- [5] A. Ali and R. Logeswaran. A visual probe localization and calibration system for cost-effective computer-aided 3d ultrasound. *Computers in Biology and Medicine*, 37(8):1141–1147, 2007.
- [6] D.V. Amin, T. Kanade, B. Jaramaz, A.M. DiGioia, C. Nikou, R.S. LaBarca, and JE Moody. Calibration method for determining the physical location of the ultrasound image plane. *Lecture Notes in Computer Science*, pages 940–947, 2001.
- [7] B.A.J. Angelsen and R.C. Waag. Ultrasound imaging: Waves, signals, and signal processing. *The Journal of the Acoustical Society of America*, 121:1820, 2007.
- [8] T. Arbel, X. Morandi, M. Comeau, and D. L. Collins. Automatic Non-linear MRI-Ultrasound Registration for the Correction of Intra-operative Brain Deformations. In *Medical Image Computing and Computer-Assisted Intervention*, volume 2208 of *LNCS*, pages 913–922. Springer, 2001.
- [9] F. Argenti and G. Torricelli. Speckle suppression in ultrasonic images based on undecimated wavelets. *EURASIP Journal on Advances in Signal Processing*, 2003(5):470–478, 2003.
- [10] J. Ashburner, J. Andersson, and K.J. Friston. Image registration using a symmetric prior in three dimensions. *Human Brain Mapping*, 9:212–225, 1998.
- [11] T. C. Aysal and K. E. Barner. Rayleigh-maximum-likelihood filtering for speckle reduction of ultrasound images. *IEEE Transactions on Medical Imaging*, 26(5):712–727, 2007.

- [12] E. Bardinet, L. Cohen, and N. Ayache. Superquadrics and free-form deformations: a global model to fit and track 3D medical data. In N. Ayache, editor, *Proc. of Computer Vision, Virtual Reality and Robotics in Medicine*, number 905 in Lect. Not. in Comp. Sci., pages 319–326, Nice, France, April 1995. Springer.
- [13] Dean C Barratt, Graeme P Penney, Carolyn S K Chan, Mike Slomczykowski, Timothy J Carter, Philip J Edwards, and David J Hawkes. Self-calibrating 3d-ultrasound-based bone registration for minimally invasive orthopedic surgery. *IEEE Trans Med Imaging*, 25(3):312–23, 2006.
- [14] C.D. Barry, C.P. Allott, N.W. John, P.M. Mellor, P.A. Arundel, D.S. Thomson, and Waterton. Three-dimensional freehand ultrasound: image reconstruction and volume analysis. *Ultrasound in Medicine & Biology*, 23(16):1209–1224, 1997.
- [15] Athanasios Bekos, Mary Arvaniti, Konstantinos Hatzimouratidis, Kyriakos Moysidis, Vasilios Tzortzis, and Dimitrios Hatzichristou. The natural history of peyronie’s disease: An ultrasonography-based study. *European Urology*, 53(3):644–651, 2008.
- [16] S. Berg, H. Torp, D. Martens, E. Steen, S. Samstad, I. Høivik, and B. Olstad. Dynamic three-dimensional freehand echocardiography using raw digital ultrasound data. *Ultrasound in medicine & biology*, 25(5):745–753, 1999.
- [17] M. I. H. Bhuiyan, Omair, and M. N. S. Swamy. New spatially adaptive wavelet-based method for the despeckling of medical ultrasound images. In *IEEE International Symposium on Circuits and Systems, 2007. ISCAS 2007.*, pages 2347–2350, 2007.
- [18] M. Black and A. Rangarajan. On the unification of line processes, outlier rejection, and robust statistics with application in early vision. *Int. J. Computer Vision*, 19(1):57–91, 1996.
- [19] J. M. Blackall, D. Rueckert, C. R. Maurer, G. P. Penney, D. L. G. Hill, and D. J. Hawkes. An image registration approach to automated calibration for freehand 3d ultrasound. *Medical Image Computing and Computer-Assisted Intervention*, 2000.
- [20] E.M. Boctor, A. Jain, M.A. Choti, R.H. Taylor, and G. Fichtinger. A rapid calibration method for registration and 3d tracking of ultrasound images using spatial localizer. *SPIE Medical imaging2003, San Diego*, pages 15–20, 2003.
- [21] L.G. Bouchet, S.L. Meeks, G. Goodchild, F.J. Bova, J.M. Buatti, and W.A. Friedman. Calibration of three-dimensional ultrasound images for image-guided radiation therapy. *Physics in Medicine and Biology*, 46(2):559–577, 2001.
- [22] B. Brendel, S. Winter, and H. Ermert. A simple and accurate calibration method for 3d freehand ultrasound. *Biomedizinische Technik*, 49(Suppl 2):872–873, 2004.
- [23] T. Brox and D. Cremers. Iterated nonlocal means for texture restoration. In *Proc. International Conference on Scale Space and Variational Methods in Computer Vision*, LNCS, Ischia, Italy, May 2007. Springer.
- [24] A. Buades, B. Coll, and J. M. Morel. A review of image denoising algorithms, with a new one. *Multiscale Modeling & Simulation*, 4(2):490–530, 2005.
- [25] R. D. Bucholz, D. D. Yeh, J. Trobaugh, L. L. McDurmont, C. D. Strum, C. Bauermann, J. M. Henderson, A. Levy, and P. Kessman. The correction of stereotactic inaccuracy caused by brain shift using an intraoperative ultrasound device.

- 
- In *Proceedings of the 1st Joint conference on CVRMed and MRCAS*, pages 459–466, 1997.
- [26] JP. Burt. *Multiresolution image processing and analysis*, chapter 2 : The pyramid as a structure for efficient computation, pages 6–38. Number 12 in Springer series in information science. Springer-verlag, 1984.
- [27] Elaine M. Caoili, Barbara S. Hertzberg, Mark A. Kliewer, David DeLong, and James D. Bowie. Refractory shadowing from pelvic masses on sonography: A useful diagnostic sign for uterine leiomyomas. *Am. J. Roentgenol*, 174(1):97–101, 2000.
- [28] J. Carr. *Surface reconstruction in 3D medical imaging*. PhD thesis, University of Canterbury, Christchurch, New Zealand, 1996.
- [29] M.M. Chakravarty, A.F. Sadikot, J. Germann, P. Hellier, G. Bertrand, and D. L. Collins. Comparison of piece-wise linear, linear, and nonlinear atlas-to-patient warping techniques: analysis of the labeling of subcortical nuclei for functional neurosurgical applications. *Human Brain Mapping*, 30(11):3574–3595, 2009.
- [30] B. Chalmond. *Modeling and inverse problems in imaging analysis*. Springer Verlag, 2003.
- [31] T.K. Chen, P. Abolmaesumi, A.D. Thurston, and R.E. Ellis. Automated 3d freehand ultrasound calibration with real-time accuracy control. In *Medical Image Computing and Computer Assisted Intervention*, volume 4190, page 899. Springer, 2006.
- [32] L. Chevalier, F. Jaillet, and A. Baskurt. Segmentation and superquadric modeling of 3d objects. *Journal of WSCG*, 11(1):1213–6972, 2003.
- [33] L. Clifford, P. Fitzgerald, and D. James. Non-rayleigh first-order statistics of ultrasonic backscatter from normal myocardium. *Ultrasound in medicine & biology*, 19(6):487–495, 1993.
- [34] R. Coifman and D. Donoho. Translation invariant de-noising. In *Lecture Notes in Statistics: Wavelets and Statistics*, pages 125–150, New York, February 1995.
- [35] R.M. Comeau, A.F. Sadikot, A. Fenster, and T.M. Peters. Intraoperative ultrasound for guidance and tissue shift correction in image-guided neurosurgery. *Medical Physics*, 27:787, 2000.
- [36] P. Coupé, P. Hellier, C. Kervrann, and C. Barillot. Nonlocal means-based speckle filtering for ultrasound images. *IEEE Transactions on Image Processing*, 18(10):2221–2229, 2009.
- [37] P. Coupé, P. Hellier, X. Morandi, and C. Barillot. A probabilistic objective function for 3D rigid registration of intraoperative US and preoperative MR brain images. In *IEEE ISBI*, pages 1320–1323, April 2007.
- [38] P. Coupé, P. Hellier, X. Morandi, and C. Barillot. A probabilistic objective function for 3d rigid registration of intraoperative us and preoperative mr brain images. In *IEEE ISBI*, 2007.
- [39] P. Coupé, P Hellier, X Morandi, and C Barillot. Probe trajectory interpolation for 3d reconstruction of freehand ultrasound. *Medical Image Analysis*, 11(6):604–615, 2007.

- [40] P. Coupé, P. Hellier, X. Morandi, and C. Barillot. Intraoperative ultrasonography for the correction of brainshift based on the matching of hyperechogenic structures. In *IEEE International Symposium on Biomedical Imaging (ISBI)*, 2010.
- [41] P. Coupé, P. Yger, S. Prima, P. Hellier, C. Kervrann, and C. Barillot. An Optimized Blockwise Non Local Means Denoising Filter for 3D Magnetic Resonance Images. *IEEE Transactions on Medical Imaging*, 27(4):425–441, 2008.
- [42] N. Courty and P. Hellier. Accelerating 3d non-rigid registration using graphics hardware. *International Journal of Image and Graphics*, 8(1):1–18, 2008.
- [43] M.B. Cuadra, C. Pollo, A. Bardera, O. Cuisenaire, J.G. Villemure, and J.P. Thiran. Atlas-based segmentation of pathological mr brain images using a model of lesion growth. *IEEE Transactions on Medical Imaging*, 23(10):1301–1314, 2004.
- [44] A. Cuzol, P. Hellier, and E. Mémin. A low dimensional fluid motion estimator. *International journal of computer vision*, 75(3):329–350, 2006.
- [45] M. Decyk, Y. Kono, and R. Mattrey. 11 MRI and Ultrasound Imaging of Lymph Nodes. In *From Local Invasion to Metastatic Cancer: Involvement of Distant Sites Through the Lymphovascular System*, page 115. Springer, 2009.
- [46] PR Detmer, G Bashein, T Hodges, KW Beach, EP Filer, DH Burns, and DE Strandness. 3d ultrasonic image feature localization based on magnetic scanhead tracking: in vitro calibration and validation. *Ultrasound in Medicine and Biology*, 20(9):923–36, 1994.
- [47] K. Djemal. Speckle reduction in ultrasound images by minimization of total variation. In *ICIP: international conference on image processing*, volume 3, pages 357–360, 2005.
- [48] D.L. Donoho. De-noising by soft-thresholding. *IEEE Transactions on Information Theory*, 41(3):613–627, 1995.
- [49] D.L. Donoho and I.M. Johnstone. Ideal spatial adaptation by wavelet shrinkage. *Biometrika*, 81(3):425–455, 1994.
- [50] N. L. Dorward, O. Alberti, B. Velani, F. A. Gerritsen, W. F. J. Harkness, N. D. Kitchen, and D. G. T. Thomas. Postimaging brain distortion: magnitude, correlates, and impact on neuronavigation. *J. of Neurosurgery*, 88:656–662, 1998.
- [51] N.L. Dorward. Neuronavigation - the surgeon’s sextant. *Journal of neurosurgery*, 11(2):101–103, 1997.
- [52] Karen Drukker, Maryellen L. Giger, and Ellen B. Mendelson. Computerized analysis of shadowing on breast ultrasound for improved lesion detection. *Medical Physics*, 30(7):1833–1842, July 2003.
- [53] V. Dutt. *Statistical analysis of ultrasound echo envelope*. PhD thesis, Mayo Clinic, 1995.
- [54] O. Ecabert, T. Butz, A. Nabavi, and J.P. Thiran. Brain shift correction based on a boundary element biomechanical model with different material properties. In *Medical Image Computing and Computer Assisted Intervention*, pages 41–49. Springer, 2003.
- [55] M. Elad. On the origin of the bilateral filter and ways to improve it. *IEEE Transactions on Image Processing*, 11(10):1141–1151, 2002.

- 
- [56] S. Foucher, G. B. Benie, and J. M. Boucher. Multiscale map filtering of sar images. *IEEE Transactions on Image Processing*, 10(1):49–60, 2001.
- [57] V.S. Frost, J.A Stiles, K.S Shanmugan, and J.C. Holtzman. A model for radar images and its application to adaptive digital filtering of multiplicative noise. *IEEE Transactions on Pattern Analysis and Machine Intelligence*, 2:157–65, 1982.
- [58] L. Gagnon and Drissi F. Smali. Speckle noise reduction of airborne sar images with symmetric daubechies wavelets. In O. E. Drummond, editor, *Proc. SPIE Signal and Data Processing of Small Targets*, volume 2759, pages 14–24, 1996.
- [59] D. G. Gobbi, R. M. Comeau, and T. M. Peters. Ultrasound/MRI Overlay with Image Warping for Neurosurgery. In *Medical Image Computing and Computer-Assisted Intervention*, volume 1935 of *LNCS*, pages 106–114. Springer, 2000.
- [60] D.G. Gobbi, B.K.H. Lee, and T.M. Peters. Correlation of pre-operative mri and intra-operative 3d ultrasound to measure brain tissue shift. In *Proceedings of SPIE the international society for optical engineering*, volume 4319, pages 264–271, 2001.
- [61] D.G. Gobbi and T.M. Peters. Interactive intra-operative 3d ultrasound reconstruction and visualization. In *Medical Image Computing and Computer Assisted Intervention*, pages 156–163. Springer, 2002.
- [62] M.J. Gooding, S.H. Kennedy, and J.A. Noble. Temporal calibration of freehand three-dimensional ultrasound using image alignment. *Ultrasound in medicine & biology*, 31(7):919–927, 2005.
- [63] J.W. Goodman. Some fundamental properties of speckle. *Journal of the Optical Society of America*, 66(11):1145–1150, 1976.
- [64] GJ Grevera and JK Udupa. An objective comparison of 3-d image interpolation methods. *IEEE transactions on medical imaging*, 17(4):642–652, 1998.
- [65] S. Gupta, R. C. Chauhan, and S. C. Saxena. Locally adaptive wavelet domain bayesian processor for denoising medical ultrasound images using speckle modelling based on rayleigh distribution. *Vision, Image and Signal Processing, IEEE Proceedings -*, 152(1):129–135, 2005.
- [66] Xiaohui Hao, Shangkai Gao, and Xiaorong Gao. A novel multiscale nonlinear thresholding method for ultrasonic speckle suppressing. *IEEE Transactions on Medical Imaging*, 18(9):787–794, 1999.
- [67] T. Hartkens, D. L. G. Hill, A. D. Castellano-Smith, D. J. Hawkes, Jr. Maurer, C. R., A. J. Martin, W. A. Hall, H. Liu, and C. L. Truwit. Measurement and analysis of brain deformation during neurosurgery. *IEEE Transactions on Medical Imaging*, 22(1):82–92, 2003.
- [68] A. Hartov, S.D. Eisner, W. Roberts, K.D. Paulsen, L.A. Platenik, and M.I. Miga. Error analysis for a free-hand three-dimensional ultrasound system for neuronavigation. *Neurosurgical Focus*, 6(3):7, 1999.
- [69] N. Hata, A. Nabavi, W. M. Wells, S. K. Warfield, R. Kikinis, P. M. Black, and F. A. Jolesz. Three-dimensional optical flow method for measurement of volumetric brain deformation from intraoperative MR images. *J Comput Assist Tomogr.*, 24(4):531–538, 2000.
- [70] N. Hata, M. Suzuki, T. Dohi, H. Iseki, K. Takakura, and D. Hashimoto. Registration of ultrasound echography for intraoperative use: a newly developed multiproperty method. In *SPIE*, volume 2359, pages 251–259, 1994.

- [71] P Hellier, C Barillot, I Corouge, B Gibaud, G Le Goualher, D L Collins, A Evans, G Malandain, N Ayache, G E Christensen, and H J Johnson. Retrospective evaluation of intersubject brain registration. *IEEE Transactions on Medical Imaging*, 22(9):1120–1130, 2003.
- [72] P. Hellier, C. Barillot, E. Mémin, and P. Pérez. Hierarchical estimation of a dense deformation field for 3D robust registration. *IEEE Transactions on Medical Imaging*, 20(5):388–402, May 2001.
- [73] P. Hellier, P. Coupé, X. Morandi, and D. L. Collins. An automatic geometrical and statistical method to detect acoustic shadows in intraoperative ultrasound brain images. *Medical Image Analysis*, 14(2):195–204, 2010.
- [74] Pierre Hellier and Christian Barillot. Coupling dense and landmark-based approaches for nonrigid registration. *IEEE Transactions on Medical Imaging*, 22(2):217–227, 2003.
- [75] D. Hill, C. Maurer, R. Maciunas, J. Barwise, J. Fitzpatrick, and M. Wang. Measurement of intraoperative brain surface deformation under a craniotomy. *Neurosurgery*, 43(3):514–526, September 1998.
- [76] K. Hirakawa and T. W. Parks. Image denoising using total least squares. *IEEE Transactions on Image Processing*, 15(9):2730–2742, 2006.
- [77] Y. Hochberg and A. C. Tamhane. *Multiple comparison procedures*. John Wiley & Sons, Inc., New York, NY, USA, 1987.
- [78] F. Hottier and A.C. Billon. 3d echography: status and perspective. *3D Imaging in Medicine: Algorithms, Systems, Applications*, pages 21–41, 1990.
- [79] PVC Hough. Machine analysis of bubble chamber pictures. In *International Conference on High Energy Accelerators and Instrumentation*, volume 73, 1959.
- [80] Po-Wei Hsu, Richard W. Prager, Andrew H. Gee, and Graham M. Treece. Freehand 3d ultrasound calibration: A review. *Advanced Imaging in Biology and Medicine*, pages 47–84, 2009.
- [81] QH Huang, YP Zheng, MH Lu, and ZR Chi. Development of a portable 3d ultrasound imaging system for musculoskeletal tissues. *Ultrasonics*, 43(3):153–163, 2005.
- [82] M. C. Jacobs, M. A. Livingston, and A. State. Managing latency in complex augmented reality systems. In *Symposium on Interactive 3D Graphics*, pages 49–54, 1997.
- [83] E. Jakeman and PN Pusey. Significance of k distributions in scattering experiments. *Physical Review Letters*, 40(9):546–550, 1978.
- [84] S. José-Estépar et al. A theoretical framework to three-dimensional ultrasound reconstruction from irregularly sampled data. *Ultrasound in medicine & biology*, 29(2):255–269, 2003.
- [85] M. Karaman, M. A. Kutay, and G. Bozdagi. An adaptive speckle suppression filter for medical ultrasonic imaging. *IEEE Transactions on Medical Imaging*, 14(2):283–292, 1995.
- [86] C. Kervrann and J. Boulanger. Optimal spatial adaptation for patch-based image denoising. *IEEE Transactions on Image Processing*, 15(10), 2006.
- [87] C. Kervrann and J. Boulanger. Local adaptivity to variable smoothness for exemplar-based image regularization and representation. *International Journal of Computer Vision*, 2008. Accepted for future publication.

- 
- [88] C. Kervrann, J. Boulanger, and P. Coupé. Bayesian non-local means filter, image redundancy and adaptive dictionaries for noise removal. In *Proc. Conf. Scale-Space and Variational Meth. (SSVM' 07)*, pages 520–532, Ischia, Italy, June 2007.
- [89] A. Khamene and F. Sauer. A novel phantom-less spatial and temporal ultrasound calibration method. In *Medical Image Computing and Computer Assisted Intervention*, volume 3750, page 65. Springer, 2005.
- [90] S. Kindermann, S. Osher, and P. W. Jones. Deblurring and denoising of images by nonlocal functionals. *Multiscale Modeling & Simulation*, 4(4):1091–1115, 2005.
- [91] A. P. King, J. M. Blackall, G. P. Penney, P. J. Edwards, D. L. G. Hill, and D. J. Hawkes. Bayesian estimation of intra-operative deformation for image-guided surgery using 3-D ultrasound. In *Medical Image Computing and Computer-Assisted Intervention*, volume 1935 of *LNCS*, pages 588–597. Springer, 2000.
- [92] A. Klein, J. Andersson, B.A. Ardekani, J. Ashburner, B. Avants, M. Chiang, G.E. Christensen, D. L. Collins, J. Gee, P. Hellier, J. Song, M. Jenkinson, C. Lepage, D. Rueckert, P. Thompson, T. Vercauteren, R.P. Woods, J. J. Mann, and R.V. Parsey. Evaluation of 14 nonlinear deformation algorithms applied to human brain mri registration. *NeuroImage*, 46(3):786–802, 2009.
- [93] H. Knutsson and C.F. Westin. Normalized and differential convolution: Methods for interpolation and filtering of incomplete and uncertain data. In *IEEE Computer Society Conference on Computer Vision and Pattern Recognition*, pages 515–515. INSTITUTE OF ELECTRICAL ENGINEERS INC (IEEE), 1993.
- [94] E. Kofidis, S. Theodoridis, C. Kotropoulos, and I. Pitas. Nonlinear adaptive filters for speckle suppression in ultrasonic images. *Signal Processing*, 52(3):357–72, 1996.
- [95] K. Krissian, K. Vosburgh, R. Kikinis, and C.-F. Westin. Speckle-constrained anisotropic diffusion for ultrasound images. In *Proceedings of IEEE Computer Society Conference on Computer Vision and Pattern Recognition*, pages 547–552, San Diego CA US, 2005.
- [96] K. Krissian, C. F. Westin, R. Kikinis, and K. G. Vosburgh. Oriented speckle reducing anisotropic diffusion. *IEEE Transactions on Image Processing*, 16(5):1412–1424, 2007.
- [97] A. Krupa. Automatic calibration of a robotized 3d ultrasound imaging system by visual servoing. In *IEEE Int. Conf. on Robotics and Automation, ICRA*, pages 4136–4141, 2006.
- [98] D.T Kuan, A.A. Sawchuck, T.C Strand, and P.Chavel. Adaptive noise smoothing filter for images with signal-dependent noise. *IEEE Transactions on Pattern Analysis and Machine Intelligence*, 7(2):165–177, 1985.
- [99] G. Le Goualher, C. Barillot, and Y. Bizais. Three-dimensional segmentation and representation of cortical sulci using active ribbons. *Int. J. of Pattern Recognition and Artificial Intelligence*, 11(8):1295–1315, 1997.
- [100] J. S. Lee. Digital image enhancement and noise filtering by use of local statistics. *IEEE Transactions on Pattern Analysis and Machine Intelligence*, 2:165–168, 1980.

- [101] T. Lehmann, C. Gonner, and K. Spitzer. Survey: interpolation methods in medical image processing. *IEEE Trans. Medical Imaging*, 18(11):1049–1075, 1999.
- [102] D.F. Leotta, P.R. Detmer, and R.W. Martin. Performance of a miniature magnetic position sensor for three-dimensional ultrasound imaging. *Ultrasound in Medicine and Biology*, 23(4):597–609, 1997.
- [103] A. Leroy, P. Mozer, Y. Payan, and J. Troccaz. Rigid registration of freehand 3d ultrasound and ct-scan kidney images. In C. Barillot, D. Haynor, and P. Hellier, editors, *Medical Image Computing and Computer Assisted Intervention*, number 3216 in LNCS, pages 837–844, St-Malo, September 2004. Springer-Verlag Berlin Heidelberg.
- [104] A. Leroy, P. Mozer, Y. Payan, and J. Troccaz. Intensity-based registration of freehand 3D ultrasound and CT-scan images of the kidney. *International Journal of Computer Assisted Radiology and Surgery*, 2(1):31–41, 2007.
- [105] M. M. J. Letteboer, M. A. Viergever, and W. J. Niessen. Rigid registration of 3D ultrasound data of brain tumours. In *CARS*, pages 433–439, 2003.
- [106] M.M.J. Letteboer, P.W.A. Willems, M.A. Viergever, and W.J. Niessen. Brain shift estimation in image-guided neurosurgery using 3-d ultrasound. *IEEE Transactions on Biomedical Engineering*, 52(2):268–276, Feb. 2005.
- [107] F. Lindseth, G.A. Tangen, T. Langø, and J. Bang. Probe calibration for freehand 3-d ultrasound. *Ultrasound in medicine & biology*, 29(11):1607–1623, 2003.
- [108] A. Lopes, R. Touzi, and E. Nezry. Adaptive speckle filters and scene heterogeneity. *IEEE Transactions on Geoscience and Remote Sensing*, 28:992–1000, 1990.
- [109] T. Loupas, W. N. McDicken, and P. L. Allan. An adaptive weighted median filter for speckle suppression in medical ultrasonic images. *IEEE transactions on Circuits and Systems*, 36(1):129–135, 1989.
- [110] Karen E. Lunn, Keith D. Paulsen, David W. Roberts, Francis E. Kennedy, Alex Hartov, and Leah A. Platenik. Nonrigid brain registration: synthesizing full volume deformation fields from model basis solutions constrained by partial volume intraoperative data. *Computer Vision and Image Understanding*, 89(2-3):299–317, 2003.
- [111] H. Q. Luong, A. Ledda, and W. Philips. Non-local image interpolation. In *IEEE International Conference on Image Processing*, pages 693–696, 2006.
- [112] A. Madabhushi, P. Yang, M. Rosen, and S. Weinstein. Distinguishing Lesions from Posterior Acoustic Shadowing in Breast Ultrasound via Non-Linear Dimensionality Reduction. *Engineering in Medicine and Biology Society, 2006. EMBS'06. 28th Annual International Conference of the IEEE*, pages 3070–3073, 2006.
- [113] R.L. Maurice and M. Bertrand. Lagrangian speckle model and tissue-motion estimation—theory. *IEEE transactions on medical imaging*, 18(7):593–603, 1999.
- [114] S. Meairs, J. Beyer, and M. Hennerici. Reconstruction and visualization of irregularly sampled three- and four-dimensional ultrasound data for cerebrovascular applications. *Ultrasound in Medicine and Biology*, 26(10):263–272, 2000.

- 
- [115] E.H.W. Meijering, W.J. Niessen, and M.A. Viergever. Quantitative evaluation of convolution-based methods for medical image interpolation. *Medical Image Analysis*, 5(2):111–126, 2001.
- [116] Laurence Mercier, Thomas Langø, Frank Lindseth, and Louis D. Collins. A review of calibration techniques for freehand 3-d ultrasound systems. *Ultrasound in Medicine and Biology*, 31(2):143 – 165, 2005.
- [117] M. I. Miga, K. D. Paulsen, J. M. Lemery, S. D. Eisner, A. Hartov, F. E. Kennedy, and D. W. Roberts. Model-updated image guidance: initial clinical experiences with gravity-induced brain deformation. *IEEE Transactions on Medical Imaging*, 18(10):866–874, 1999.
- [118] RC Molthen, PM Shankar, JM Reid, F. Forsberg, EJ Halpern, CW Piccoli, and BB Goldberg. Comparisons of the rayleigh and k-distribution models using in vivo breast and liver tissue. *Ultrasound in medicine & biology*, 24(1):93–100, 1998.
- [119] J.J. Moré. The levenberg-marquardt algorithm: implementation and theory. In *Numerical Analysis*, volume 630, pages 105–116. Springer, 1978.
- [120] Diane M. Muratore and Robert L. Galloway. Beam calibration without a phantom for creating a 3-d freehand ultrasound system. *Ultrasound in Medicine and Biology*, 27(11):1557 – 1566, 2001.
- [121] Arya Nabavi, Peter McL. Black, David T. Gering, Carl-Fredrik Westin, Vivek Mehta, Richard S. Jr. Pergolizzi, Mathieu Ferrant, Simon K. Warfield, Nobuhiko Hata, Richard Schwartz, William M. Wells, Ron Kikinis, and Ferenc A. M. Jolesz. Serial intraoperative magnetic resonance imaging of brain shift. *Neurosurgery*, 48(4):787–798, 2001.
- [122] K. Nakada, M. Nakamoto, Y. Sato, K. Konishi, M. Hashizume, and S. Tamura. A rapid method for magnetic tracker calibration using a magneto-optic hybrid tracker. In *Medical Image Computing and Computer Assisted Intervention*, pages 285–293. Springer, 2003.
- [123] M. Nakamoto, Y. Sato, K. Nakada, Y. Nakajima, K. Konishi, M. Hashizume, and S. Tamura. A temporal calibration method for freehand 3d ultrasound system : a preliminary result. In *CARS*, 2003.
- [124] T.R. Nelson and D.H. Pretorius. Interactive acquisition, analysis, and visualization of sonographic volume data. *International Journal of Imaging Systems and Technology*, 8(1):26–37, 1997.
- [125] Christopher Nimsky, Oliver. Ganslandt, S. Cerny, Peter Hastreiter, Gunther Greiner, and Rudolf Fahlbusch. Quantification of, visualization of, and compensation for brain shift using intraoperative magnetic resonance imaging. *Neurosurgery*, 47(5):1070–1080, November 2000.
- [126] J. E. Odegard, H. Guo, M. Lang, C. S. Burrus, R. O. Wells, L. M. Novak, and M. Hiatt. Wavelet based SAR speckle reduction and image compression. In *SPIE Proc. on Algorithms for Synthetic Aperture*, volume 2487, pages 259–271, 1995.
- [127] A. Ogier, P. Hellier, and C. Barillot. Restoration of 3D medical images with total variation scheme on wavelet domains (TVW). In *SPIE Medical Imaging*, volume 6144, February 2006.
- [128] J. Oh, M.D. Feldman, J. Kim, C. Condit, S. Emelianov, and T.E. Milner. Detection of magnetic nanoparticles in tissue using magneto-motive ultrasound. *Nanotechnology*, 17:4183–4190, 2006.

- [129] R. Ohbuchi, D. Chen, and H. Fuchs. Incremental volume reconstruction and rendering for 3-d ultrasound imaging. In *PROCEEDINGS-SPIE THE INTERNATIONAL SOCIETY FOR OPTICAL ENGINEERING*, pages 312–312. Citeseer, 1992.
- [130] J. M. Park, W. J. Song, and W. A. Pearlman. Speckle filtering of sar images based on adaptive windowing. *Vision, Image and Signal Processing*, 146(4):191–197, 1999.
- [131] X. Pennec, P. Cachier, and N. Ayache. Tracking brain deformations in time-sequences of 3D US images. *Pattern Recognition Letters - Special Issue on Ultrasonic Image Processing and Analysis*, 24(4-5):801–813, February 2003.
- [132] G.P. Penney, J.M. Blackall, M.S. Hamady, T. Sabharwal, A. Adam, and D.J. Hawkes. Registration of freehand 3d ultrasound and magnetic resonance liver images. *Medical Image Analysis*, 8:81–91, 2004.
- [133] G.P. Penney, J.A. Schnabel, D. Rueckert, D.J. Hawkes, and W.J. Niessen. Registration-based interpolation using a high-resolution image for guidance. In *Medical Image Computing and Computer Assisted Intervention*, pages 558–565. Springer, 2004.
- [134] GP Penney, JA Schnabel, D. Rueckert, MA Viergever, and WJ Niessen. Registration-based interpolation. *IEEE Transactions on Medical Imaging*, 23(7):922–926, 2004.
- [135] P. Perona and J. Malik. Scale-space and edge detection using anisotropic diffusion. *IEEE Transactions on Pattern Analysis and Machine Intelligence*, 12(7):629–639, 1990.
- [136] O. Pfrria, L. Chevalier, A. Franois-Joubert, J.P. Caravel, S. Dalsoglio, S. Lavalle, and P. Cinquin. Using a 3D position sensor for registration of SPECT and US images of the kidney. In *CVRMed*. Springer, 1995.
- [137] A. Pizurica, , A. M. Wink, E. Vansteenkiste, W. Philips, and J. Roerdink. A review of wavelet denoising in mri and ultrasound brain imaging. *Current Medical Imaging Reviews*, 2(2):247–260, 2006.
- [138] T. C. Poon and R. N. Rohling. Comparison of calibration methods for spatial tracking of a 3-d ultrasound probe. *Ultrasound Med Biol*, 31(8):1095–108, 2005. 0301-5629 (Print) Journal Article calibration pas lu pas dans review cite me.
- [139] B. C. Porter, D. J. Rubens, J. G. Strang, J. Smith, S. Totterman, and K. J. Parker. Three-dimensional registration and fusion of ultrasound and MRI using major vessels as fiducial markers. *IEEE Transaction on Medical Imaging*, 20(4):354–359, April 2001.
- [140] R. W. Prager, R. N. Rohling, A. H. Gee, and L. Berman. Rapid calibration for 3-d freehand ultrasound. *Ultrasound Med Biol*, 24(6):855–69, 1998.
- [141] Richard W. Prager, Andrew Gee, and Laurence Berman. Stradx: real-time acquisition and visualization of freehand three-dimensional ultrasound. *Medical Image Analysis*, 3(2):129 – 140, 1999.
- [142] R.W. Prager, A.H. Gee, G.M. Treece, and L.H. Berman. Analysis of speckle in ultrasound images using fractional order statistics and the homodyned k-distribution. *Ultrasonics*, 40(1-8):133–137, 2002.
- [143] RW Prager, AH Gee, GM Treece, and LH Berman. Decompression and speckle detection for ultrasound images using the homodyned k-distribution. *Pattern Recognition Letters*, 24(4-5):705–713, 2003.

- 
- [144] I. Pratikakis, C. Barillot, P. Hellier, and E. Mémin. Robust multiscale deformable registration of 3D ultrasound images. *International Journal of Image and Graphics*, 3(4):547–566, 2003.
- [145] I. Reinertsen, M. Descoteaux, S. Drouin, K. Siddiqi, and D. L. Collins. Vessel driven correction of brain shift. In *Medical Image Computing and Computer-Assisted Intervention*, volume 3217 of *LNCS*, pages 208–216. Springer, 2004.
- [146] D. W. Roberts, A. Hartov, F. E. Kennedy, M. I Miga, and K. D. Paulsen. Intraoperative brain shift and deformation: a quantitative analysis of cortical displacement in 28 cases. *Neurosurgery*, 43:749–758, 1998.
- [147] A. Roche, X. Pennec, G. Malandain, and N. Ayache. Rigid registration of 3D ultrasound with MR images: a new approach combining intensity and gradient information. *IEEE Transaction on Medical Imaging*, 20(10):1038–1049, October 2001.
- [148] R. Rohling, A. Gee, and L. Berman. A comparison of freehand three-dimensional ultrasound reconstruction techniques. *Medical Image Analysis*, 3(4):339–359, 1999.
- [149] F. Rousseau, P. Hellier, M. Letteboer, W. Niessen, and C. Barillot. Quantitative evaluation of three calibration methods for 3d freehand ultrasound. *IEEE Transactions on Medical Imaging*, 25(11):1492–1501, Novembre 2006.
- [150] Francois Rousseau, Pierre Hellier, and Christian Barillot. Confusius: a robust and fully automatic calibration method for 3d freehand ultrasound. *Med Image Anal*, 9(1):25–38, 2005.
- [151] Francois Rousseau, Pierre Hellier, and Christian Barillot. A novel temporal calibration method for 3-d ultrasound. *IEEE Trans Med Imaging*, 25(8):1108–1112, 2006.
- [152] P.J. Rousseeuw and A.M. Leroy. *Robust regression and outlier detection*. Wiley-IEEE, 2003.
- [153] G. J. Rubino, C. Lycette, K. Farahani, D. McGill, B. van de Wiele, and Villablanca. Interventional magnetic resonance imaging guided neurosurgery - the UCLA experience with the first 100 cases. *Electromedica*, 68:37–46, 2000.
- [154] L.I. Rudin, S. Osher, and E. Fatemi. Nonlinear total variation based noise removal algorithms. *Physica D*, 60:259–268, 1992.
- [155] J.M. Sanches and J.S. Marques. A rayleigh reconstruction/interpolation algorithm for 3d ultrasound. *Pattern recognition letters*, 21(10):917–926, 2000.
- [156] Y. Sato, M. Nakamoto, Y. Tamaki, T. Sasama, I. Sakita, Y. Nakajima, M. Monden, and S. Tamura. Image guidance of breast cancer surgery using 3-d ultrasound images and augmented reality visualization. *IEEE Trans Med Imaging*, 17(5):681–693, 1998.
- [157] C. Sheng, Y. Xin, Y. Liping, and S. Kun. Total variation-based speckle reduction using multi-grid algorithm for ultrasound images. In *ICIAP: international conference on image analysis and processing*, volume 3617, pages 245–252, 2005.
- [158] S. Sherebrin, A. Fenster, R.N. Rankin, and D. Spence. Freehand three-dimensional ultrasound: implementation and applications. In *Proceedings of SPIE*, volume 2708, page 296, 1996.
- [159] K. Shoemake. Animating rotation with quaternion curves. *ACM SIGGRAPH computer graphics*, 19(3):245–254, 1985.

- [160] O.V. Solberg, F. Lindseth, H. Torp, R.E. Blake, and T.A. Nagelhus Hernes. Freehand 3d ultrasound reconstruction algorithms—a review. *Ultrasound in Medicine and Biology*, 33(7):991–1009, 2007.
- [161] Robin Steel, Tamie L. Poepping, Rosemary S. Thompson, and Charles Macaskill. Origins of the edge shadowing artefact in medical ultrasound imaging. *Ultrasound in Medicine & Biology*, 30(9):1153–1162, 2004.
- [162] Z. Tao, H. D. Tagare, and J. D. Beaty. Evaluation of four probability distribution models for speckle in clinical cardiac ultrasound images. *IEEE Transactions on Medical Imaging*, 25(11):1483–1491, 2006.
- [163] P. C. Tay, S. T. Acton, and J. A. Hossack. A stochastic approach to ultrasound despeckling. In *Biomedical Imaging: Nano to Macro, 2006. 3rd IEEE International Symposium on*, pages 221–224, 2006.
- [164] P. C. Tay, S. T. Acton, and J. A. Hossack. Ultrasound despeckling using an adaptive window stochastic approach. In *IEEE International Conference on Image Processing*, pages 2549–2552, 2006.
- [165] P. Thevenaz, T. Blu, and M. Unser. Interpolation revisited. *IEEE Transactions on Medical Imaging*, 19(7):739–758, 2000.
- [166] N. Thune, O.H. Gilja, T. Hausken, and K. Matre. A practical method for estimating enclosed volumes using 3d ultrasound. *European Journal of Ultrasound*, 3(1):83–92, 1996.
- [167] D. Timmerman, A. C. Testa, T. Bourne, L. Ameye, D. Jurkovic, C. Van Holsbeke, D. Paladini, B. Van Calster, I. Vergote, S. Van Huffel, and L. Valentin. Simple ultrasound-based rules for the diagnosis of ovarian cancer. *Ultrasound in Obstetrics and Gynecology*, 31(6):681–690, 2008.
- [168] G. M. Treece, A. H. Gee, R. W. Prager, C. J. C. Cash, and L. H. Berman. High resolution freehand 3d ultrasound. *Ultrasound in Medicine and Biology*, 9(4):529–546, 2003.
- [169] J W Trobaugh, W D Richard, K R Smith, and R D Bucholz. Frameless stereotactic ultrasonography: method and applications. *Computerized medical imaging and graphics*, 18(4):235–46, 1994.
- [170] J. Varandas, P. Baptista, J. Santos, R. Martins, and J. Dias. Volus—a visualization system for 3d ultrasound data. *Ultrasonics*, 42:689–694, 2004.
- [171] A. Viswanathan, E.M. Boctor, R.H. Taylor, G. Hager, and G. Fichtinger. Immediate ultrasound calibration with three poses and minimal image processing. *Lecture Notes in Computer Science*, pages 446–454, 2004.
- [172] C. Wachinger, W. Wein, and N. Navab. Three-dimensional ultrasound mosaicing. In *Medical Image Computing and Computer-Assisted Intervention - MICCAI 2007*, 2007.
- [173] M. P. Wachowiak, A. S. Elmaghraby, R. Smolíková, and J. M. Zurada. Classification and estimation of ultrasound speckle noise with neural networks. In *IEEE International Symposium on Bio-Informatics and Biomedical Engineering (BIBE'00)*, pages 245–252, 2000.
- [174] M.P. Wachowiak, R. Smolíková, J.M. Zurada, and A.S. Elmaghraby. Estimation of k distribution parameters using neural networks. *IEEE Transactions on Biomedical Engineering*, 49(6):617–620, 2002.

- 
- [175] JN Welch, JA Johnson, MR Bax, R. Badr, and R. Shahidi. A real-time freehand 3d ultrasound system for image-guided surgery. In *2000 IEEE Ultrasonics Symposium*, volume 2, 2000.
- [176] L. Weng, J.M. Reid, P.M. Shankar, and K. Soetanto. Ultrasound speckle analysis based on the k distribution. *The Journal of the Acoustical Society of America*, 89:2992, 1991.
- [177] Z. Yang and M. D. Fox. Speckle reduction and structure enhancement by multichannel median boosted anisotropic diffusion. *EURASIP J. Appl. Signal Process.*, 2004(1):2492–2502, January 2004.
- [178] Y. Yu and S. T. Acton. Speckle reducing anisotropic diffusion. *IEEE Transactions on Image Processing*, 11(11):1260–1270, 2002.
- [179] Y. Yu, J. A. Molloy, and S. T. Acton. Three-dimensional speckle reducing anisotropic diffusion. In *Signals, Systems and Computers, 2003. Conference Record of the Thirty-Seventh Asilomar Conference on*, volume 2, pages 1987–1991 Vol.2, 2003.
- [180] P.A. Yushkevich, J. Piven, H.C. Hazlett, R.G. Smith, S. Ho, J.C. Gee, and G. Gerig. User-guided 3d active contour segmentation of anatomical structures: significantly improved efficiency and reliability. *Neuroimage*, 31(3):1116–1128, 2006.
- [181] F. Zhang, Y. M. Yoo, L. M. Koh, and Y. Kim. Nonlinear diffusion in laplacian pyramid domain for ultrasonic speckle reduction. *IEEE Transactions on Medical Imaging*, 26(2):200–211, 2007.
- [182] X. Zong, A. F. Laine, and E. A. Geiser. Speckle reduction and contrast enhancement of echocardiograms via multiscale nonlinear processing. *IEEE Transactions on Medical Imaging*, 17(4):532–540, 1998.



## JOURNAL PAPERS

1. C. Nauczyciel, P. Hellier, X. Morandi, S. Blestel, D. Drapier, J.C. Ferre, C. Barillot, B. Millet. Assessment of standard coil positioning in transcranial magnetic stimulation in depression. *Psychiatry research*, 2010.
2. F. Palhano, G. Andrade Barroso, P. Coupé, P. Hellier. Real time ultrasound image denoising. *Journal of Real-Time Image Processing*, 2010.
3. P. Hellier, P. Coupé, X. Morandi, D. L. Collins. An automatic geometrical and statistical method to detect acoustic shadows in intraoperative ultrasound brain images. *Medical Image Analysis*, 14(2): 195-204, 2010.
4. M.M. Chakravarty, A.F. Sadikot, J. Germann, P. Hellier, G. Bertrand, D. L. Collins. Comparison of piece-wise linear, linear, and nonlinear atlas-to-patient warping techniques: analysis of the labeling of subcortical nuclei for functional neurosurgical applications. *Human Brain Mapping*, 30(11):3574-3595, 2009.
5. A. Klein, J. Andersson, B.A. Ardekani, J. Ashburner, B. Avants, M. Chiang, G.E. Christensen, D. L. Collins, J. Gee, P. Hellier, J. Song, M. Jenkinson, C. Lepage, D. Rueckert, P. Thompson, T. Vercauteren, R.P. Woods, J. J. Mann, R.V. Parsey. Evaluation of 14 nonlinear deformation algorithms applied to human brain MRI registration. *NeuroImage*, 46(3):786-802, 2009.
6. P. Coupé, P. Hellier, C. Kervrann, C. Barillot. NonLocal Means-based Speckle Filtering for Ultrasound Images. *IEEE Transactions on Image Processing*, 18(10):2221-2229, 2009.
7. N. Courty, P. Hellier. Accelerating 3D Non-Rigid Registration using Graphics Hardware. *International Journal of Image and Graphics*, 8(1):1-18, 2008.
8. P. Coupé, P. Hellier, S. Prima, C. Kervrann, C. Barillot. 3D Wavelet Sub-Bands Mixing for Image Denoising. *International Journal of Biomedical Imaging*, 2008.
9. C. Nauczyciel, L. Guibert, P. Hellier, D. Drapier, N. Le Garzic, X. Morandi, B. Millet. TMS and neuronavigation in treatment of depression: a view into the future. *Encephale*, 34(6):625-8, 2008.
10. P. Coupé, P. Yger, S. Prima, P. Hellier, C. Kervrann, C. Barillot. An Optimized Blockwise Non Local Means Denoising Filter for 3D Magnetic Resonance Images. *IEEE Transactions on Medical Imaging*, 27(4):425-441, 2008.
11. A. Cuzol, P. Hellier, E. Mémin. A low dimensional fluid motion estimator. *International journal of computer vision*, 75(3):329-350, 2007.
12. P. Coupé, P. Hellier, X. Morandi, C. Barillot. Probe Trajectory Interpolation for 3D Reconstruction of Freehand Ultrasound. *Medical Image Analysis*, 11(6):604-615, 2007.
13. F. Rousseau, P. Hellier, M. Letteboer, W. Niessen, C. Barillot. Quantitative Evaluation of Three Calibration Methods for 3D Freehand Ultrasound. *IEEE Transactions on Medical Imaging*, 25(11):1492-1501, 2006.

## 8. PUBLICATIONS

---

14. F. Rousseau, P. Hellier, C. Barillot. A Novel Temporal Calibration Method for 3-D Ultrasound. *IEEE Transactions on Medical Imaging*, 25(8):1108-1112, Aout 2006.
15. F. Rousseau, P. Hellier, C. Barillot. Confusius: a robust and fully automatic calibration method for 3D freehand ultrasound. *Medical Image Analysis*, 9:25-38, 2005.
16. P. Hellier, C. Barillot. A hierarchical parametric algorithm for deformable multimodal image registration. *Computer Methods and Programs in Biomedicine*, 75(2):107-115, Aout 2004.
17. P. Hellier, C. Barillot. Coupling dense and landmark-based approaches for non rigid registration. *IEEE Transactions on Medical Imaging*, 22(2):217-227, 2003.
18. I. Pratikakis, C. Barillot, P. Hellier, E. Mémin. Robust multiscale deformable registration of 3D ultrasound images. *International Journal of Image and Graphics*, 3(4):547-566, 2003.
19. I. Corouge, P. Hellier, B. Gibaud, C. Barillot. Interindividual functional mapping: a nonlinear local approach. *NeuroImage*, 19(4):1337-1348, 2003.
20. P. Hellier, C. Barillot, I. Corouge, B. Gibaud, G. Le Goualher, D.L. Collins, A. Evans, G. Malandain, N. Ayache, G.E. Christensen, H.J. Johnson. Retrospective evaluation of inter-subject brain registration. *IEEE Transactions on Medical Imaging*, 22(9):1120-1130, 2003.
21. C. Baillard, P. Hellier, C. Barillot. Segmentation of brain 3D MR images using level sets and dense registration. *Medical Image Analysis*, 5(3):185-194, 2001.
22. P. Hellier, C. Barillot, E. Mémin, P. Pérez. Hierarchical estimation of a dense deformation field for 3D robust registration. *IEEE Transactions on Medical Imaging*, 20(5):388-402, 2001.
23. P. Hellier, C. Barillot, E. Mémin, P. Pérez. Estimation robuste 3D d'un champ de déformation pour le recalage non-linéaire inter-sujet d'images cérébrales. *Traitement du Signal*, 17(2):99-112, 2000.

### BOOKS AND BOOK CHAPTERS

1. Christian Barillot, David R. Haynor, Pierre Hellier. *Medical Image Computing and Computer-Assisted Intervention - MICCAI 2004 - Part I. Lecture Notes in Computer Science*, Springer-Verlag, 2004.
2. I. Corouge, P. Hellier, C. Barillot. From Global to Local Approaches for Non-Rigid Registration. In *Medical Imaging Systems Technology: Methods in General Anatomy*, C. T. Leondes (ed.), Vol. 265, World Scientific Publishing, Singapour, 2005.
3. P. Hellier. Inter-subject non-rigid registration: survey and methods. J. Suri, D. Wilson, S. Laxminarayan (eds.), Vol. 3, *Handbook of medical image analysis: segmentation and registration methods*, Kluwer, 2004.

### EDITORIALS

1. D. R. Haynor, C. Barillot, P. Hellier. A selection of papers from MICCAI 2004: the marriage of data and prior information. *Academic Radiology*, 12(10):1229-31, 2005. [download](#)
2. C. Barillot, D.R. Haynor, P. Hellier. *Medical Image Computing and Computer-Assisted Intervention*. *Medical Image Analysis*, 9(5):411-412, Octobre 2005.
3. P. Hellier, D.R. Haynor, C. Barillot. *Medical Image Computing and Computer-Assisted Intervention*. *Journal of Computer Assisted Surgery*, 10(4):197-197, Juillet 2005.

---

REVIEWED CONFERENCE PAPERS

1. S.J. Chen, P. Hellier, J.-Y. Gauvrit, M. Marchal, X. Morandi, and D.L. Collins. An Anthropomorphic Polyvinyl Alcohol Triple-Modality Brain Phantom based on Colin27. In 13th International Conference on Medical Image Computing and Computer Assisted Intervention, Miccai 2010, Beijing, China, September 2010.
2. P. Coupé, P. Hellier, X. Morandi, C. Barillot. . Intraoperative ultrasonography for the correction of brainshift based on the matching of hyperechogenic structures. In IEEE International Symposium on Biomedical Imaging: From Nano to Macro, 2010.
3. P. Coupé, P. Hellier, C. Kervrann, C. Barillot. Bayesian non local means-based speckle filtering. In 5th IEEE International Symposium on Biomedical Imaging: From Nano to Macro, ISBI'2008, Paris, France, Mai 2008.
4. P. Hellier, P. Coupé, P. Meyer, X. Morandi, D.L. Collins. Acoustic shadows detection, application to accurate reconstruction of 3D intraoperative ultrasound. In 5th IEEE International Symposium on Biomedical Imaging: From Nano to Macro, ISBI'2008, Paris, France, Mai 2008.
5. C. Barillot, P. Coupé, O. El Ganaoui, B. Gibaud, P. Hellier, P. Jannin, P. Paul, S. Prima, N. Wiest-Daesslé, X. Morandi. Image guidance in neurosurgical procedures, the Visages point of view. In 4th IEEE International Symposium on Biomedical Imaging: From Nano to Macro, ISBI'2007, Pages 1056-1059, Washington, états-Unis, Avril 2007.
6. P. Coupé, P. Hellier, X. Morandi, C. Barillot. A probabilistic objective function for 3D rigid registration of intraoperative US and preoperative MR brain images. In IEEE International Symposium on Biomedical Imaging: From Nano to Macro, Pages 1320-1323, Avril 2007.
7. A. Ogier, P. Hellier, C. Barillot. Restoration of 3D medical images with total variation scheme on wavelet domains (TVW). San Diego, états-Unis, Février 2006.
8. L.S. Ait-ali, S. Prima, P. Hellier, B. Carsin, G. Edan, C. Barillot. STREM: a robust multidimensional parametric method to segment MS lesions in MRI. In 8th International Conference on Medical Image Computing and Computer-Assisted Intervention, MICCAI'2005, J. Duncan, G. Gerig (eds.), Lecture Notes in Computer Science, Volume 3749, Pages 409-416, Palm Springs, états-Unis, Octobre 2005.
9. P. Coupé, P. Hellier, N. Azzabou, C. Barillot. 3D Freehand Ultrasound Reconstruction based on Probe Trajectory. In 8th International Conference on Medical Image Computing and Computer-Assisted Intervention, MICCAI'2005, J. Duncan, G. Gerig (eds.), Lecture Notes in Computer Science, Volume 3749, Pages 597-604, Palm Springs, états-Unis, Octobre 2005.
10. A. Cuzol, P. Hellier, E. Mémin. A novel parametric method for non-rigid image registration. In 19th International Conference on Information Processing in Medical Imaging, IPMI'2005, G. Christensen, M. Sonka (eds.), Lecture Notes in Computer Science, Pages 456-467, Glenwood Springs, états-Unis, Juillet 2005.
11. A. Ogier, P. Hellier. A modified Total Variation denoising method in the context of 3D ultrasound images. In 7th International Conference on Medical Image Computing and Computer-Assisted Intervention, MICCAI'2004, C. Barillot, D.R. Haynor, P. Hellier (eds.), Lecture Notes in Computer Science, Volume 3216, Pages 70-77, Saint-Malo, France, Septembre 2004.

12. F. Rousseau, P. Hellier, C. Barillot. Méthode de calibration automatique pour système échographique 3D main-libre. In 14ème Congrès Francophone AFRIF/AFIA de Reconnaissance des Formes et Intelligence Artificielle, RFIA'2004, Toulouse, France, Janvier 2004.
13. C. Ciofalo, C. Barillot, P. Hellier. Combining fuzzy logic and level set methods for 3D MRI brain segmentation. In 2nd IEEE International Symposium on Biomedical Imaging: From Nano to Macro, ISBI'2004, Pages 161-164, Arlington, états-Unis, Avril 2004.
14. A. Ogier, P. Hellier, C. Barillot. Speckle reduction on ultrasound image by variational methods and adaptive Lagrangian multipliers. In 2nd IEEE International Symposium on Biomedical Imaging: From Nano to Macro, ISBI'2004, Pages 547-550, Arlington, états-Unis, Avril 2004.
15. M. Letteboer, P. Hellier, D. Rueckert, P. Willems, J.W. Berkelbach, W. Niessen. Non-rigid registration of intraoperatively acquired 3D ultrasound data of brain tumors. In Proc. of Medical Robotics, Navigation and visualization, T. Buzug, T. Lueth (eds.), Pages 11-19, Remagen, Allemagne, Mars 2004.
16. F. Rousseau, P. Hellier, C. Barillot. Robust and automatic calibration method for 3D freehand ultrasound. In 6th International Conference on Medical Image Computing and Computer-Assisted Intervention, MICCAI'2003, R.E. Ellis, T.M. Peters (eds.), Lecture Notes in Computer Science, Volume 2879, Pages 440-448, Montréal, Canada, Novembre 2003.
17. P. Hellier. Consistent intensity correction of MR images. In IEEE International Conference on Image Processing, ICIP'2003, Barcelone, Espagne, Septembre 2003.
18. P. Hellier, J. Ashburner, I. Corouge, C. Barillot, K.J. Friston. Inter subject registration of functional and anatomical data using SPM. In 5th International Conference on Medical Image Computing and Computer-Assisted Intervention, MICCAI'2002, Lecture Notes in Computer Science, Volume 2489, Pages 590-597, Tokyo, Japon, Septembre 2002.
19. F. Rousseau, P. Hellier, C. Barillot. A fully automatic calibration procedure for freehand 3D ultrasound. In 1st IEEE International Symposium on Biomedical Imaging: Macro to Nano, ISBI'2002, Pages 985-988, Washington, états-Unis, Juillet 2002.
20. C. Barillot, P. Hellier, I. Corouge. Non rigid registration in neuroimaging: from a retrospective evaluation of global approaches to new advances in local and hybrid methods. In 1st IEEE International Symposium on Biomedical Imaging: Macro to Nano, ISBI'2002, Pages 469-472, Washington, états-Unis, Juin 2002.
21. M. Letteboer, P. Willems, P. Hellier, W. Niessen. Acquisition of 3D ultrasound images during neuronavigation. In Computer Assisted Radiology and Surgery - 16th International Congress and Exhibition, CARS'2002, H.U. Lemke, M.W. Vannier, K. Doi, K. Inamura, A.G. Farman, J.H.C. Reiber (eds.), Pages 121-126, Paris, France, Juin 2002.
22. I. Corouge, C. Barillot, P. Hellier, P. Toulouse, B. Bibaud. Non-linear local registration of functional data. In 4th International Conference on Medical Image Computing and Computer-Assisted Intervention, MICCAI'2001, W.J. Niessen, M.A. Viergever (eds.), Lecture Notes in Computer Science, Volume 2208, Pages 948-956, Utrecht, Pays-Bas, Octobre 2001.
23. P. Hellier, C. Barillot, I. Corouge, B. Gibaud, G. Le Goualher, D.L. Collins, A. Evans, G. Malandain, N. Ayache. Retrospective evaluation of inter-subject brain registration. In 4th International Conference on Medical Image Computing and Computer-Assisted Intervention, MICCAI'2001, W.J. Niessen, M.A.

- 
- Viergever (eds.), *Lecture Notes in Computer Science*, Volume 2208, Pages 258-265, Utrecht, Pays-Bas, Octobre 2001.
24. I. Pratikakis, C. Barillot, P. Hellier. Robust multi-scale non-rigid registration of 3D ultrasound images. In 3rd International Conference on Scale-Space and Morphology in Computer Vision, Scale-Space'2001, M. Kerckhove (ed.), *Lecture Notes in Computer Science*, Volume 2106, Pages 389-397, Vancouver, Canada, Juillet 2001.
  25. I. Corouge, P. Hellier, P. Toulouse, B. Bibaud, C. Barillot. A new inter-individual functional mapping scheme based on a local non linear registration method. In 7th International Conference on Functional Mapping of the Human Brain, HBM'2001, Brighton, Royaume-Uni, Juin 2001.
  26. P. Hellier, C. Barillot. Cooperation between local and global approaches to register brain images. In 17th International Conference on Information Processing in Medical Imaging, IPMI'2001, M.F. Insana, R.M. Leahy (eds.), *Lecture Notes in Computer Science*, Volume 2082, Pages 315-328, Davis, états-Unis, Juin 2001.
  27. P. Hellier, C. Barillot. Multimodal non-rigid warping for correction of distortions in functional MRI. In 3rd International Conference on Medical Image Computing and Computer-Assisted Intervention, MICCAI'2000, S.L. Delp, A.M. DiGioia, B. Jaramaz (eds.), *Lecture Notes in Computer Science*, Volume 1935, Pages 512-521, Pittsburgh, états-Unis, Octobre 2000.
  28. C. Baillard, P. Hellier, C. Barillot. Cooperation between level set techniques and dense 3D registration for the segmentation of brain structures. In 15th International Conference on Pattern Recognition, ICPR'2000, Volume 1, Pages 991-994, Barcelone, Espagne, Septembre 2000.
  29. C. Baillard, P. Hellier, C. Barillot. Segmentation of 3D brain structures using level sets and dense registration. In IEEE Workshop on Mathematical Methods in Biomedical Image Analysis, MMBIA'2000, B. Kimia, A. Amini, D. Metaxas (eds.), Pages 94-103, Hilton Head Island, états-Unis, Juin 2000.
  30. P. Hellier, C. Barillot, E. Mémin, P. Pérez. An energy-based framework for dense 3D registration of volumetric brain image. In IEEE Conference on Computer Vision and Pattern Recognition, CVPR'2000, B. Kimia, A. Amini, D. Metaxas (eds.), Volume 2, Pages 270-275, Hilton Head Island, états-Unis, Juin 2000.
  31. P. Hellier, C. Barillot, E. Mémin, P. Pérez. Medical image registration with robust multigrid techniques. In 2nd International Conference on Medical Image Computing and Computer-Assisted Intervention, MICCAI'99, C. Taylor, A.C.F. Colchester (eds.), *Lecture Notes in Computer Science*, Volume 1679, Pages 680-687, Cambridge, Royaume-Uni, Septembre 1999.
  32. P. Hellier, C. Barillot, E. Mémin, P. Pérez. Recalage d'images cérébrales par estimation robuste contextuelle du flot optique. In 17ème Colloque GRETSI sur le traitement du signal et des images, Volume 4, Pages 1077-1080, Vannes, France, Septembre 1999.
  33. C. Barillot, G. Le Goualher, P. Hellier, B. Gibaud. Statistical analysis of brain sulci based on active ribbon modeling. In SPIE Medical Imaging 1999: Image Processing, K.M. Hanson (ed.), Volume 3661, Pages 312-321, San Diego, états-Unis, Février 1999.

#### PATENTS

1. Dispositif et Procédé d'aide à la Localisation Cérébrale, 09/00254, 21.01.2009.

## 8. PUBLICATIONS

---

2. Dispositif de traitement d'images pour la mise en correspondance d'images d'une même portion d'un corps obtenues par résonance magnétique et par ultrasons, n<sup>o</sup> 07/02386, Avril 2007
3. Dispositif de traitement d'images amélioré, registered 21-04-2008, n<sup>o</sup> 08/02206

### SOFTWARES

1. F. Palhano, G. Andrade, P. Hellier. FUID (Fast Ultrasound Image Denoising). Dépôt à l'Agence pour la Protection des Programmes - IDDN.FR.001.310018.000.S.P.2009.000.21000, 2009.
2. P. Coupé, P. Hellier, C. Barillot. INRIABrainshift. Dépôt à l'agence pour la protection des programmes - IDDN.FR.001.110024.000.S.P.2008.000.21000, 2008.
3. N. Courty, P. Hellier. GpuReg. Dépôt à l'agence pour la protection des programmes - IDDN.FR.001.170009.000.S.P.2008.000.21000, 2008.
4. S. Blestel, V. Gratsac, P. Hellier. TMS Inria. Depot a l'agence pour la protection des programmes - IDDN.FR.001.470037.000.S.P.2007.000.31230, 2007.
5. P. Hellier. Correction of Local Acoustic Shadows - CLASH. Depot a l'agence pour la protection des programmes - IDDN.FR.001.270019.000.S.P.2007.000.21000, Juillet 2007.
6. P. Coupé, P. Yger, S. Prima, P. Hellier, C Kervrann, C. Barillot. MONADE: Multimodal and Optimized Non local meAns DEnoising. Dépôt à l'Agence pour la Protection des Programmes, numéro IDDN.FR.001.070033.000.S.P.2007.000.21000, Février 2007.
7. P. Coupé, P. Hellier, C. Barillot. TULIPE : Three-dimensional ULtrasound reconstruction Incorporating ProbE trajectory. Dépôt à l'Agence pour la Protection des Programmes, numéro IDDN.FR.001.120034.000.A.2006.000.21000, Janvier 2006.
8. P. Hellier, C. Barillot. JULIEt: Joint Use of Landmarks and Intensities for Elastic registration. Dépôt à l'Agence pour la Protection des Programmes, 2003.
9. P. Hellier, C. Barillot, E. Mémin, P. Pérez. ROMEO: RObust Multigrid Elastic registration based on Optical flow. Dépôt à l'Agence pour la Protection des Programmes, numéro IDDN.FR.001.450015.00.S.P.2001.000.21000, Juillet 2001.
10. C. Barillot, F. Boisse, P. Hellier. VisTAL: Volumetric Images Treatments and Analysis Library. Dépôt à l'Agence pour la Protection des Programmes, 2000.